FORMATION CHARACTERIZATION FOR ACID STIMULATION

A Dissertation

by

YUHAI ZHOU

Submitted to the Office of Graduate and Professional Studies of
Texas A&M University
in partial fulfillment of the requirements for the degree of

DOCTOR OF PHILOSOPHY

Chair of Committee,	Ding Zhu
Committee Members,	A. Daniel Hill
	David Schechter
	Michael Pope
Head of Department,	Jeff Spath

December 2019

Major Subject: Petroleum Engineering

ABSTRACT

Matrix acidizing is an effective stimulation technique for carbonate reservoirs and it has been practiced for years in the industry. By injecting acid below the formation fracturing pressure, highly permeable paths called “wormholes” are created to bypass the near wellbore damage and penetrate the formation as deep as possible to improve flow conditions. For various types of carbonate formation, it is important to design the volume of acid needed and the optimal acid injection rate to achieve minimum acid consumption. Besides, acid type, acid concentration, core size, mineralogy and petrophysical properties of the carbonate rocks affect the optimal conditions for matrix acidizing. This research focuses on the characterization of carbonate formation at multiple scales to investigate how the petrophysical parameters affect matrix acidizing. The study covers three different scales: micro scale, core scale, and log scale.

For micro-scale study, three types of rock samples (Indiana Limestone, Desert Pink, and Travertine) was selected and micro-Computer Tomography (micro-CT) technique was adopted to capture the microscopic heterogeneity in the pore structure. Image processing was performed and important petrophysical parameters quantified, including pore size distribution, pore connectivity, and the surface-area-to-volume ratio of the rock. The quantified parameters were used to correlate to the optimal conditions obtained by physical experiments and rock permeability. A concept named equivalent pore radius was defined. This study determined that this parameter, equivalent pore radius, is tightly related to the permeability of rock and can be used to improve the optimal conditions prediction model for matrix acidizing.

For the core-scale study, the optimal conditions for one type of the Travertine, a highly heterogeneous carbonate rock, is measured with core flooding test in the laboratory. The optimal

conditions for various rock types under different experimental conditions are collected and sets of curves for optimal conditions are generated. The results of this study indicate that the optimal conditions for most carbonate rocks lie in a narrow range, which is useful for guiding matrix acidizing design.

Finally, the characterization for carbonate formation at log scale mainly focuses on the most important petrophysical properties (porosity and permeability). The methods for porosity estimation, lithology estimation, and permeability estimation are discussed. The depth-by-depth porosity profile, permeability profile, and lithology are integrated with a horizontal well acid stimulation software (HWAS), which helps customize matrix acidizing design. Field application based on true formation properties are demonstrated.

DEDICATION

Dedicated to my parents and brother, for their love and support.

ACKNOWLEDGEMENTS

I would like to thank Dr. Zhu and Dr. Hill sincerely for their valuable guidance, encouragement, and support for my research. I appreciate every advice that keeps me motivated and enlightened.

I would also thank Dr. David Schechter and Dr. Michael Pope for their valuable suggestions and comments. I benefit a lot from the course about carbonate rocks instructed by Dr. Pope and I enjoyed the field trip in west Texas.

Thanks also go to my friends, colleagues and the department faculty and staff. Thanks Haoran Cheng, Mateus Schwalbet, and Robert Shirley for all the valuable technical discussion and help with laboratory measurements. Special thanks to my friends, Jihui Ding, Yun Shang, Lu Chi, Lizhong Wang, Peiyuan Wei, Lijun Peng, Yu Meng, Xin Chen and everyone in Jianbing Group for all the happiness and life we shared.

Finally, thanks to my parents and my older brother for their encouragement and love.

CONTRIBUTORS AND FUNDING SOURCES

This work was supervised by a dissertation committee consisting of Professor Ding Zhu (advisor), Professor A. Daniel Hill, Professor David Schechter of the Department of Petroleum Engineering and Professor Michael Pope of Department of Geology & Geophysics.

All work for the dissertation was completed independently by the student.

This work was made possible by financial support of the Acid Stimulation Research Program in Department of Petroleum Engineering, Texas A&M University.

NOMENCLATURE

a	Width of simplified capillary tube model
A	The cross-section area fluid flowing through (e.g. cm^2)
A_i	The area of each pore on one 2D image slice
B	Formation volume factor, rb/stb
b	Length of simplified capillary tube model
c	Height of simplified capillary tube model
c_t	Total compressibility of the reservoir, psi^{-1}
C_1	The number of "holes" or "tunnels" in the isolated pore clusters
C_3	Parameter for general porosity-permeability correlation
D_3	Parameter for general porosity-permeability correlation
d_{core}	Diameter of core plug, inch
$d_{e,wh}$	Diameter of the generated wormhole cluster, ft
f_f	Friction factor
h	Reservoir thickness, ft
J	Productivity Index, STB/day/psi
J_D	Dimensionless Productivity Index
k	Permeability, mD
k_c	Parameter for Coates equation
k_s	Permeability of damaged region, mD
k_w	Parameter for Wyllie-Rose equation
k_{wh}	Wormhole permeability, mD
k_x	Permeability in horizontal direction x, mD

k_y	Permeability in horizontal direction y, mD
k_z	Permeability in vertical direction, mD
L	Length of tubing, ft
L_c	The actual pore length in capillary tube model
L_{core}	The length of core plug, inch
L_w	Horizontal well length, ft
m	Slope of wellbore flow equation
m_1	Adjustable parameter for tortuosity equation
m_{wh}	Dominant wormhole number in 2D plane across the wellbore
n_1	Adjustable parameter for tortuosity equation
n	Total number of pores on one image slice
N	The number of the capillary tubes in simplified capillary tube model
N_1	Total number of isolated pore clusters
N_{ac}	Acid capacity number
N_{re}	Reynold's number
$PV_{bt,opt}$	Optimal pore volume to breakthrough, dimensionless
p_e	Pressure at reservoir boundary, psi
$p_{wf,ideal}$	Ideal bottomhole pressure without formation damage, psi
$p_{wf,ideal}$	Real bottomhole pressure , psi
p_{wh}	Pressure at well head, psi
Q	The flow rate through the porous media (e.g. cm3/s);
q	Flow rate in single capillary tube (e.g. cm3/s);
R	Radius of each capillary tube

R_a	Average arithmetic pore radius in a binary rock image slice, μm
R_e	Equivalent pore radius, μm
r	The coordinate in radial direction
r_e	Radius of the reservoir, ft
r_s	Radius of damaged zone
r_w	wellbore radius, inch
r_{wh}	Wormhole front penetration, ft
s	Skin factor
S_c	Total surface area of the capillary tubes
S_w	Water saturation, %
$S_{w,irr}$	Irreducible water saturation, %
S/V	Specific surface area
u	Fluid velocity along the capillary tube
v_{wh}	Wormhole front velocity, cm/s
$v_{i,tip}$	Acid velocity at the wormhole front, cm/s
$v_{i,tip,opt}$	Optimal acid velocity at the wormhole front, cm/s
$V_{i,opt}$	Optimal interstitial velocity, cm/min
V_c	Bulk volume of capillary tube model
V_{core}	Volume of core plug, cm^3

Greek

α_z	Coefficient for wormhole spacing in axial direction
μ_1	Mean value of the radius of pores, um
μ	Viscosity of fluid, cP

σ	Variance of the pore radius, um^2
ϕ	Porosity, v/v
ϕ_t	Total porosity, v/v
ϕ_e	Effective porosity, v/v
τ	Tortuosity, dimensionless
ρ	Density of fluid, g/cc
γ	Parameter for fluid-loss-limited wormhole model
ε	Relative pipe roughness

TABLE OF CONTENTS

Page

ABSTRACT ii

DEDICATION iv

ACKNOWLEDGEMENTS v

CONTRIBUTORS AND FUNDING SOURCES vi

NOMENCLATURE vii

TABLE OF CONTENTS xi

LIST OF FIGURES xiii

LIST OF TABLES xix

1. INTRODUCTION: 1

    1.1 Background 1
    1.2 Literature Review 2
        1.2.1 Optimal Conditions 2
        1.2.2 Factors Affecting Optimal Conditions 4
        1.2.3 Wormhole Models 10
        1.2.4 Applications to Horizontal Wells 15
    1.3 Objective and Approach 15
    1.4 Dissertation Outline 16

2. FORMATION CHARACTERIZARTION AT MICRO SCALE 18

    2.1 Introduction 18
    2.2 Data Acquisition and Image Processing 18
        2.2.1 Data Acquisition 18
        2.2.2 Image Processing 20
    2.3 Characterization of Pore Size Distribution 27
    2.4 Characterization of Pore Connectivity 36
    2.5 Characterization of Surface-Area-to-Volume Ratio 45
    2.6 Characterization of Permeability 53
    2.7 Section Summary 60

3. FORMATION CHARACTERIZARTION AT CORE SCALE 62

3.1 Introduction 62
3.2 Travertine 62
3.2.1 Petrophysical Characteristics of Travertine 62
3.2.2 CT-Scan for Travertine 64
3.3 Experiments for Matrix Acidizing 66
3.3.1 Experiment Apparatus 66
3.3.2 Experiment Procedure 68
3.3.3 Experiment Results 71
3.4 Statistical Results for Optimal Conditions 72
3.4.1 General Wormhole-Efficiency Curve 72
3.4.2 The Effect of Porosity and Permeability on Optimal Conditions 76
3.5 Section Summary 79

4. FORMATION CHARACTERIZARTION AT LOG SCALE 81

4.1 Introduction 81
4.2 Wormhole Models Review 82
4.3 Well Performance with Wormhole 84
4.4 Horizontal Well Acid Stimulator 87
4.5 Petrophysical Properties Estimation 91
4.5.1 Estimation of Porosity and Lithology 91
4.5.2 Estimation of Permeability 94
4.6 Integration of Petrophysical Modules into HWAS 99
4.7 Section Summary 101

5. FIELD EXAMPLE OF FORMATION CHARACTERIZATION FOR ACID STIMULATION 102
5.1 Field Application with HWAS 102
5.2 Estimation of Optimal Conditions 105
5.2.1 Estimation of Optimal Conditions for Indiana Limestone 105
5.2.2 Estimation of Optimal Conditions for Kansas Chalk 107
5.3 Skin Factor Calculation with Optimal Conditions 108
5.3.1 Case A 109
5.3.2 Case B 112
5.4 Section Summary 114

6. CONCLUSIONS 115

REFERENCES 117

LIST OF FIGURES

Page

Figure 1.1 Field post-stimulation buildup-test data for carbonate matrix acidizing (Reprinted from Furui et al., 2010) 3

Figure 1.2 Dissolution patterns for different injection rates (Reprinted from McDuff et al., 2010) 4

Figure 1.3 Thin section for limestone (on the left) and dolomite rock (on the right) (Reprinted from Dong 2015) 7

Figure 1.4 The wormhole efficiency curve generalized by reservoir rock type (Reprinted from Ziauddin and Bize 2007) 8

Figure 1.5 The master wormhole curve with Damkohler number (Reprinted from Zakaria et al. 2015) 8

Figure 1.6 Relationship between permeability and optimal conditions for 2 rock types (Reprinted from Etten 2015) 9

Figure 1.7 Capillary model of a porous medium (Reprinted from Schechter 1969) 11

Figure 1.8 2D network model built for limestone (Reprinted from Hoefner and Fogler 1988) 12

Figure 1.9 Core acidizing results matched with the semi-empirical model (Reprinted from Buijse and Glasbergen, 2005) 13

Figure 1.10 Simulated dissolution pattern with various injection rate (Reprinted from Schwalbert et al. 2017) 14

Figure 1.11 Dissertation outline 16

Figure 2.1 Phoenix nanotom Micro-CT scanner 19

Figure 2.2 Image slice of Indiana limestone sample exported from micro-CT scanner(a), selected region of interest(b) 20

Figure 2.3 Example of identified pore space with thresholding for Indiana limestone sample (histogram on the upper right corner, pores are colored red) 21

Figure 2.4 Binarized image slice for Indiana limestone where black is pore space and

white is rock matrix 22
Figure 2.5a The processed binary images of scanned 6 md Indiana limestone (pores are colored black)..... 24
Figure 2.5b The processed binary images of scanned 8 md Indiana limestone (pores are colored black)..... 24
Figure 2.5c The processed binary images of scanned 10 md Indiana limestone (pores are colored black)..... 25
Figure 2.5d The processed binary images of scanned 239 md Indiana limestone (pores are colored black)..... 25
Figure 2.5e The processed binary images of scanned 99 md Travertine (pores are colored black)..... 26
Figure 2.5f The processed binary images of scanned 600 md Travertine (pores are colored black)..... 26
Figure 2.5g The processed binary images of scanned 33 md Desert Pink (pores are colored black)..... 27
Figure 2.6 The pore radius distribution of all pores accounted for all the rock samples.... 28
Figure 2.7 The arithmetic average value of pore radius against rock permeability..... 29
Figure 2.8 Concept of equivalent pore radius R_e 30
Figure 2.9 Probability function of the calculated equivalent pore radius for Indiana limestone sample 4..... 31
Figure 2.10 The probability function of the calculated equivalent pore radius for all rock samples..... 32
Figure 2.11 Relationship between the calculated mean values of equivalent pore radius against the measured permeability..... 34
Figure 2.12 The relationship between the mean value of top 5% percent large pores against the measured permeability in the laboratory 35
Figure 2.13 Equivalent pore radius against the optimal pore volume to breakthrough..... 35
Figure 2.14 Illustration of a processed 2D micro-CT scanned images (pores are colored black)..... 37
Figure 2.15 Binarized image stacks along the Z direction (pores care colored black)..... 38

Figure 2.16 The plot of the connectivity numbers in unit volume against the laboratory-measured permeability 39

Figure 2.17 The plot of the connectivity numbers in unit volume against optimal pore volume to breakthrough 39

Figure 2.18 The plot of the connectivity numbers in unit volume against optimal interstitial velocity 40

Figure 2.19 Voxel connection types 40

Figure 2.20 Illustration of pore cluster labeling by Hoshen-Kopelman's algorithm 41

Figure 2.21 The identified connected pixels from binary image: Original image on the top and identified connected objects colored on the bottom 42

Figure 2.22 Plot of permeability and connected pore clusters in unit volume 42

Figure 2. 23 Extracted pore structure for 600 mD Travertine (pore space in yellow white) 43

Figure 2. 24 Extracted pore structure for 239 mD Indiana limestone (pore space in yellow white) 43

Figure 2. 25 Extracted pore structure for 33 mD Desert Pink rock (pore space in yellow white) 44

Figure 2. 26 Extracted pore structure for 10 mD Indiana limestone (pore space in yellow white) 44

Figure 2.27 The extracted pore system of Indiana limestone with pores colored white on the left; thin section of Indiana limestone sample with 239 md permeability on the right 45

Figure 2.28 The plot of the surface-area-to-volume ratio against measured permeability. 46

Figure 2.29 The plot of the specific surface-area-to-volume ratio against equivalent pore radius 47

Figure 2. 30 An illustration of capillary tube model 47

Figure 2.31 The reciprocal of equivalent pore radius against the surface-area-to-volume ratio calculated by image process and simplified capillary tube model (red dots) 49

Figure 2.32 The capillary tube model with tortuosity 49

Figure 2.33 The surface-area-to-volume ratio against the optimal pore volume to breakthrough 51

Figure 2.34 The plot of the surface-area-to-volume ratio against the optimal interstitial velocity 51

Figure 2.35 Relationship between ϕ/(S/V) against optimal pore volume to breakthrough 52

Figure 2.36 The illustration of fluid flow in one capillary tube 54

Figure 2.37 Fluid velocity profile in a capillary tube 55

Figure 2.38 Estimated permeability by using Kozeny-Carman equation 58

Figure 2.39 Estimated permeability against laboratory-measured permeability 59

Figure 3.1 The Travertine block for this study (H indicates horizontal direction, V indicates vertical direction) 63

Figure 3.2 Travertine core plugs cut from vertical direction 63

Figure 3.3 CT scanner used for Travertine scan 64

Figure 3.4 CT scan working principle illustration 65

Figure 3.5 The CT scanned image for Travertine samples 66

Figure 3.6 The experiment setup for matrix acidizing (Reprinted from Cheng 2017) 67

Figure 3.7 Core holder 68

Figure 3.8 Travertine block where the cores are cut from 68

Figure 3.9 Measurement of the weight of dry Travertine core plug 69

Figure 3.10 Wormhole efficiency curve for Travertine 72

Figure 3.11 Statistics for wormhole-efficiency curves 73

Figure 3.12 The plot of permeability against optimal pore volume to breakthrough 76

Figure 3.13 Relationship between core permeability and optimal interstitial velocity 77

Figure 3.14 The plot of porosity against optimal pore volume to breakthrough 78

Figure 3.15 The plot of porosity against optimal interstitial velocity 78

Figure 4.1 CT scanned image of wormholes generated with 15 wt% HCl injection at optimal injection rate (Reprinted from McDuff et al 2010)..... 81

Figure 4.2 Illustration of wormhole generation in horizontal wells 82

Figure 4.3 The cross-section view of various region near wellbore under acidizing 85

Figure 4.4 The models of horizontal well acid simulator (Reprinted from Ueda 2015) 87

Figure 4.5 Workflow chart for matrix acidizing design with HWAS..... 88

Figure 4.6 The updated workflow HWAS..... 89

Figure 4.7 The well logs used for multi-mineral joint inversion, the estimated lithology and estimated porosity. Tracks from 1 to 9 are: measured depth (meter);caliper log and gamma ray; bulk density; neutron porosity; compressional wave slowness; photo electric factor log; shallow resistivity and deep resistivity; estimated volumetric concentration of each mineral; estimated total porosity and total porosity by core measurements (red dots) (Reprinted from Zhou et al. 2019) 94

Figure 4.8 Porosity-permeability correlation from core measurement for a tight carbonate formation (Reprinted from Zhou et al. 2017)..... 96

Figure 4.9 Example of estimated permeability by different method. Tracks from 1 to 9 are: measured depth in meter; caliper log and gamma ray log; compressional wave slowness log; shallow resistivity and deep resistivity log; estimated volumetric concentration of minerals; estimated porosity with core measurements (in red dots); estimated water saturation; estimated permeability with porosity-permeability correlation; estimated permeability with Timur's equation, Morris-Biggs equation, Coates equation, the core permeability (in red dots) (Reprinted from Zhou et al. 2017)..... 97

Figure 4.10 The estimated permeability with non-parametric regression against the measured core permeability 99

Figure 4.11 The integrated petrophysical module in HWAS 100

Figure 4.12 The petrophysical data resolution converter..... 100

Figure 5.1 Well completion scheme 102

Figure 5.2 Total skin variation with time..... 104

Figure 5.3 Depth-by-depth porosity, permeability, acid consumption, wormhole length,

and skin factor along the horizontal well after simulated acidizing treatment .. 105

Figure 5.4 Measured optimal conditions for Indiana limestone 106

Figure 5.5 Measured optimal conditions for Kansas Chalk..... 107

Figure 5.6 Workflow to calculate skin with estimated optimal conditions 109

Figure 5.7 Acid consumption against wormhole radius (Case A)..... 112

Figure 5.8 Acid consumption against wormhole radius (Case B) 113

LIST OF TABLES

Page

Table 1.1 The influencing factors for optimal conditions..... 10

Table 2.1 Measured porosity and permeability for studied rocks..... 19

Table 2.2 Image size, resolution and calculated porosity. 20

Table 2.3 Identified pore area of Indiana limestone sample 4 image slices. 31

Table 2.4 Explanation of equivalent pore radius concept..... 33

Table 2.5 Properties calculated based on binary image and laboratory measurements..... 53

Table 2.6 Parameters for permeability estimation with Kozenny-Carman's equation..... 58

Table 3.1 Acidizing experiment conditions for Travertine..... 70

Table 3.2 Matrix acidizing results for Travertine 71

Table 3.3 Statistics for matrix acidizing experiments..... 74

Table 5.1 Well and Stimulation Data..... 103

Table 5.2 Optimal Points (Tran, 2013) 103

Table 5.3 Pumping Schedule 103

Table 5.4 Optimal conditions, wormhole radius and skin factor for case A 108

Table 5.5 Optimal conditions, wormhole radius and skin factor for case B..... 111

1. INTRODUCTION

1.1 Background

Carbonate reservoirs contain over 60% of the world's oil reserves and 40% of its gas reserves (Schlumberger 2019). Prolific oil-bearing carbonate formations occur over the Middle East, Europe, North America, Libya (e.g. Sirte basin), and Asia (Zhang et al. 2014). Exploration and production from carbonate reservoirs is challenging for geologists, petrophysicists, reservoir, completion and production engineers due to the strong heterogeneity in these rocks at multiple scales. Stimulation techniques, such as matrix acidizing and fracturing, either with or without proppant, has long been applied in carbonate fields and proven to be effective. Matrix acidizing is achieved by injecting acid into the formation below the formation fracturing pressure to remove the damaged near-wellbore region as well as creating highly permeable paths, referred as "wormholes", into the formation. Deep wormhole penetration (e.g. 20 ft) is preferred to improve flow conditions in the formation. Matrix acidizing in carbonate formations is the focus of this study.

For matrix acidizing, optimal injection rate and the amount of acid used are crucial factors affecting the success of acid treatments. Low acid injection rate results in face-dissolution with shallow acid penetration and excessive waste of acid. High acid injection rate can lead to branching shape of wormholes and also shallow acid penetration. Optimal conditions for matrix acidizing yield deepest acid penetration with least acid volume consumed. Optimal conditions normally are obtained by performing laboratory experiments and fitting with semi-empirical wormhole models (Buijse and Glasbergen, 2005; Furui, etc. 2010). Many factors affect the optimal conditions, including acid type, acid concentration, temperature, mineralogy, and petrophysical properties (e.g. porosity and permeability). Understanding the influence of petrophysical

properties for carbonate rock at multiple scales on acidizing helps to improve acid stimulation efficiency.

1.2 Literature Review

This section focuses on the definition of optimal conditions and the influencing factors for optimal conditions from multiple scales. The models for wormholing also are reviewed.

1.2.1 Optimal Conditions

For production engineers, productivity index J is used to quantify the deliverability of a well. For a vertical oil well, the productivity index for steady-state flow is given in Equation 1.1. The dimensionless productivity index J_D is as Equation 1.2.

$$J = \frac{q}{p_e - p_{wf}} = \frac{kh}{141.2B\mu} J_D \tag{1.1}$$

$$J_D = \frac{1}{\ln(\frac{r_e}{r_w}) + s} \tag{1.2}$$

where q is the oil flow rate in STB/d, p_e is the reservoir pressure at outer boundary in psi, p_{wf} is the bottomhole flowing pressure in psi, k is the formation permeability in mD, h is the formation thickness in ft, B is the formation volume factor in *res* bbl/STB, μ is the fluid viscosity in cp, r_e is the reservoir radius in ft, r_w is the wellbore radius in ft, s is the skin factor (dimensionless).

Equation 1.2 indicates that positive skin reduces the productivity index and negative skin improves productivity index. Formation damage and well completion usually result in a positive skin factor, and previous studies showed that this skin factor can be as high as hundreds (Paccaloni

et al. 1988). On the other hand, well stimulation can create a negative skin factor close to the value of $ln(r_e/r_w)$, which ranges from 6-8 for most oil and gas wells (Equation 1.1). The average skin factor is -4 for matrix acidizing for approximately 400 acid-stimulated wells (Figure 1.1), indicating matrix acidizing is effective to reduce skin and boost production (Furui et al. 2010).

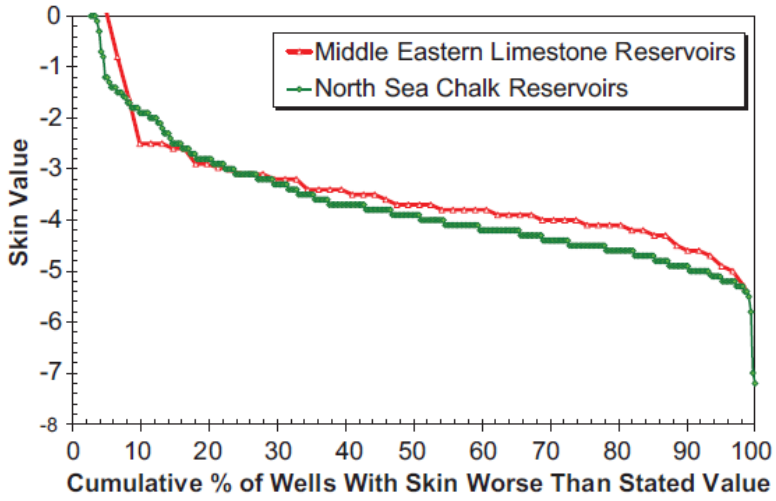

Figure 1.1 Field post-stimulation buildup-test data for carbonate matrix acidizing (Reprinted from Furui et al. 2010)

For various types of carbonate formations, it is important to know the volume of acid needed and the optimal acid injection rate to achieve deep penetration with minimum acid consumption. Based on numerous previous studies, the acid injection rate is the most influential parameter on wormhole structure and the amount of acid required. Matrix acidizing experiments were conducted with core plugs using low, optimal and high acid injection rates (Mcduff et al. 2010). The generated wormhole structures are visualized with high-resolution CT images in Figure 1.2. If the acid injection rate is relatively low, large, conical-shaped wormholes are created (the wormhole image on the top of Figure 1.2). Even lower injection rate can create face-dissolution. As the injection rate increases, the wormholes become much narrower and branch less (wormhole

image in the middle of Figure 1.2). Highly branched wormholes and ramified dissolution patterns are observed when the injection rate is relatively high (wormhole image in the lower section in Figure 1.2). There exists an optimal acid injection rate $V_{i,opt}$ that represents the conditions at which the minimum volume of acid is required for the wormhole to break through (Wang et al. 1993, Fredd and Fogler 1998). At this optimal acid injection rate, the optimal pore volume to breakthrough, $PV_{bt,opt}$, is defined as the ratio of the volume of acid injected into the core plug to achieve breakthrough to the pore volume in the core plug (Fredd and Fogler 1998). Determination of the optimal acid injection rate and the amount of acid to be used is an essential step for matrix acidizing design.

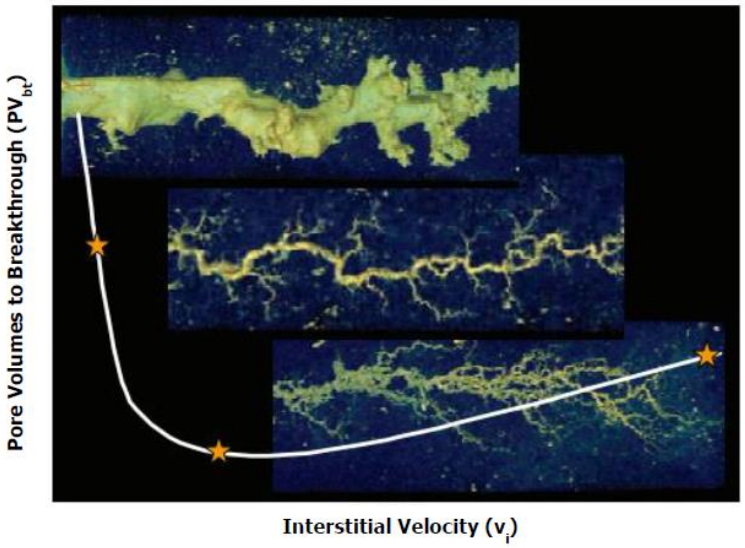

Figure 1.2 Dissolution patterns for different injection rates (Reprinted from McDuff et al., 2010)

1.2.2 Factors Affecting Optimal Conditions

Besides acid injection rate, researchers have studied several important factors affecting the optimal conditions for matrix acidizing: acid type (Huang et al. 1997, Fredd and Fogler, 1999, Bazin, 2001, Buijse et al. 2003), acid concentration (Wang et al. 1993, Fredd and Fogler, 1999, Bazin, 2001,

Furui et al. 2010), temperature (Wang et al. 1993, Fredd and Fogler, 1999, Bazin, 2001, Dong 2015), core size (Bazin, 2001, Furui et al. 2010, Dong et al. 2012), mineralogy (Wang et al. 1993, Ziauddin and Bize 2007, Dong 2015) and petrophysical properties of rock (Frick et al. 1994, Bazin, 2001, Ziauddin and Bize 2007, Etten 2015). The influence of some factors was studied extensively and the variation of each factor can lead to significantly different optimal conditions in the laboratory and also in the field. In this study, a comprehensive study on the influence of pore structure and petrophysical properties of carbonate rocks is carried out to determine the optimal conditions of matrix acidizing.

1.2.2.1 Effect of Acid Concentration

Acid concentration defines the reaction power of the acid system used. Because the reaction rate is very fast in carbonate, acid concentration is not critical but still influential. Based on laboratory experiments, increasing the acid concentration decreases the optimal pore volume to breakthrough $PV_{bt,opt}$ and increases optimal injection rate $V_{i,opt}$ (Wang et al. 1993, Bazin 2001). Increasing acid concentration decreases $PV_{bt,opt}$ but no definite trend for $V_{i,opt}$ was observed (Furui 2010). Increasing acid concentration speeds up the dominant wormhole growth more than the branched wormhole growth based on experiments, which is a reasonable explanation for the decrease of $PV_{bt,opt}$ (Furui 2010). Increasing the acid concentration up to 17.5 wt% results in an increase of $V_{i,opt}$ but higher acid concentration decreases $V_{i,opt}$ (Dong 2015).

1.2.2.2 Effect of Temperature

Several researchers observed that increasing temperature leads to higher $V_{i,opt}$ (Wang et al., 1993, Fredd and Fogler, 1999, Bazin, 2001, and Furui et al., 2010). This is important since experimental

temperature should be similar or close to the true formation temperature when measuring the optimal conditions in the laboratory for matrix acidizing treatment design.

Besides, higher temperature requires smaller $PV_{bt,opt}$ (Wang et al. 1993) but it was observed that temperature does not have a significant influence on $PV_{bt,opt}$ (Bazin 2001, Furui et al. 2010). Higher temperature causes lower fluid viscosity, higher diffusion rate and higher reaction rate, which enhances the growth of branching wormholes and leads to more acid consumption (Furui et al. 2010).

1.2.2.3 Effect of Core Size

Optimal conditions usually are identified in the laboratory by performing acidizing experiments with core plugs. PV_{bt} is no longer dependent on core length when the flow rate exceeds the optimal flow rate for cores of 20 cm in length (Bazin 2001). Optimal acid flux value becomes stable when cores are 6 inches or longer (Dong et al. 2012). Both $PV_{bt,opt}$ and $V_{i,opt}$ for 4-inch diameter core is much lower than that of 1-inch diameter core (Furui et al. 2010).

1.2.2.4 Effect of Mineralogy

The experimental results indicate that optimal conditions cannot be reached for dolomite at room temperature with a reasonable amount of acid (Hoefner and Fogler, 1989, Wang et al., 1993 and Dong, 2015). Matrix acidizing in dolomite requires a larger amount of acid and a higher injection rate than in limestone formations due to the low reaction rate of acid (Wang et al., 1993). Besides the chemical composition difference between calcite ($CaCO_3$) and dolomite ($CaMg(CO_3)_2$) that affect optimal conditions, the different pore structure between them can be another reason (Figure 1.3). Thin sections of limestone and dolomite indicate planar fabrics and the intercrystalline pore spaces are more abundant in the dolomite thin sections.

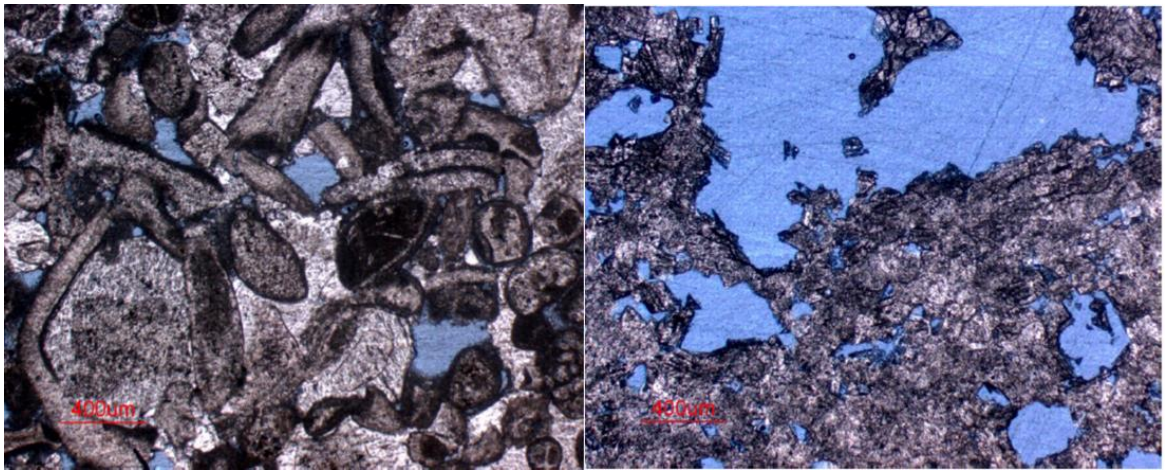

Figure 1.3 Thin section for limestone (on the left) and dolomite rock (on the right) (Reprinted from Dong 2015)

1.2.2.5 Effect of Rock Petrophysical Properties

Two sets of Lavoux limestone were studied to determine the effect of permeability on optimal conditions and that higher permeability rocks require higher $PV_{bt,opt}$ and higher $V_{i,opt}$ (Bazin 2001). Increasing permeability leads to higher $V_{i,opt}$ with radial flow core flooding experiments (Frick et al. 1994). The effects of pore-scale heterogeneities on carbonate matrix acidizing indicate that the optimal conditions for eight different types of carbonate can be classified into 4 groups (Figure 1.4) based on reservoir rock type, which is defined by porosity spatial distribution (Ziauddin and Bize 2007). Type 1 has mostly well-connected interparticle pores such as Indiana limestone; Type 2 has both interparticle pores and intraparticle pores (e.g. Austin Chalk); Type 3 is poorly sorted grainstone with moldic pores; Type 4 has large moldic pores and the matrix is tight. Several type curves describing the matrix acidizing behavior for all carbonate rocks tested were generated (Figure 1.4).

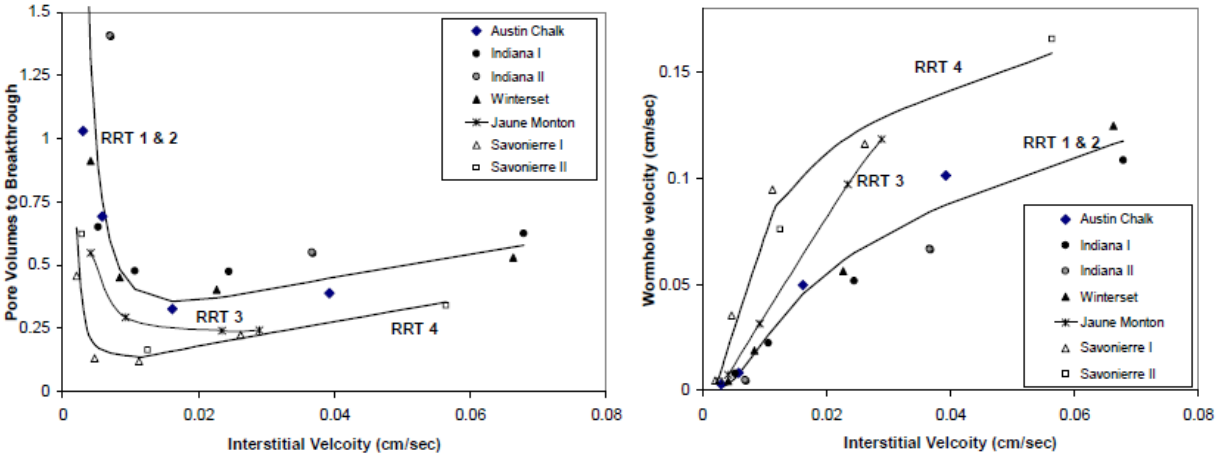

Figure 1.4 The wormhole efficiency curve generalized by reservoir rock type (Reprinted from Ziauddin and Bize 2007)

Instead of sub-dividing all affecting factors and studying each individually, Zakaria et al. (2015) used a concept called flowing fraction, which represents the relative amount of pores contributing to flow most, to quantify the heterogeneity at pore-scale for different carbonate rocks. Based on the flowing fraction concept, a master wormhole efficiency curve that applies to different injection temperatures was generated (Figure 1.5). The master wormhole curve represents the relationship between Damkohler number and pore volume to breakthrough (Figure 1.5).

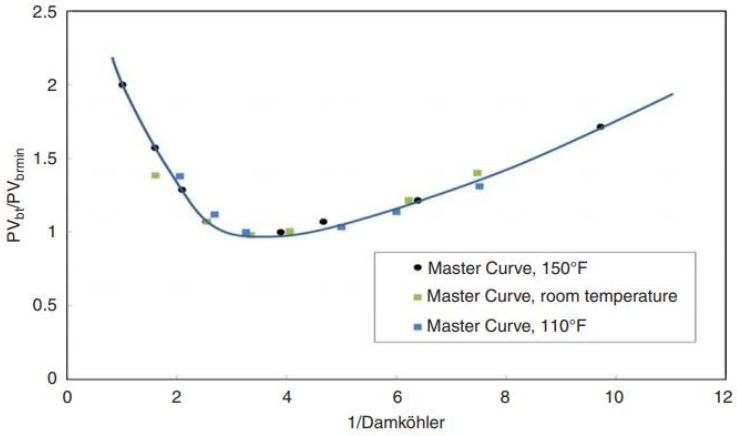

Figure 1.5 The master wormhole curve with Damkohler number (Reprinted from Zakaria et al. 2015)

In vuggy carbonate rocks, the vug network creates a preferential pathway for injected acid, and PV_{bt} decreases as vuggy fraction of porosity increases (Izgec 2009). The local pressure drop created by vugs affects the acid flow pathway dominantly. The effect of permeability and porosity on optimal conditions with core flooding experiments indicate that $PV_{bt,opt}$ is positively correlated to the permeability of samples but $V_{i,opt}$ is not following the same trend (Etten 2015). The trend between permeability and optimal conditions based on three Indiana limestone samples and one Desert Pink sample as shown in Figure 1.6. The effect of pore size distribution on wormhole propagation with micro-CT scanned rock samples was studied (Dubetz et al. 2016).

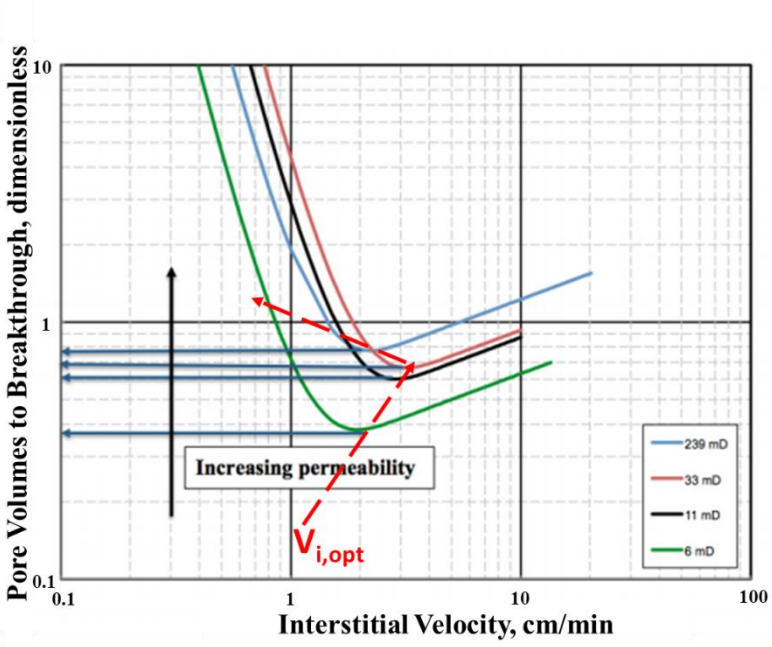

Figure 1.6 Relationship between permeability and optimal conditions for 2 rock types (Reprinted from Etten 2015)

The effects of all the factors reviewed above are generalized in Table 1.1. The up arrow symbol "↑" indicates the optimal condition is positively related to the influencing factor and the down arrow "↓" indicates the optimal condition is negatively correlated to the influencing factor.

Table 1.1 The influencing factors for optimal conditions

	$PV_{bt,opt}$	$V_{i,opt}$
Acid Concentration	↓	Not definite
Temperature	Not definite	↑
Core Size	↓	↓

1.2.3 Wormhole Models

Several categories of carbonate acidizing models were developed by previous researchers to study the propagation of wormholes. The existing matrix acidizing models can be classified into several groups. The assumptions, limitations, and applications for each type of model were discussed in Fredd and Miller (2000) and Akanni et al. (2015).

1.2.3.1 Capillary Tube Model

In the capillary tube model, wormholes are modeled as cylindrical tubes pre-existing in the matrix (Figure 1.7). The surface reaction influence on the evolution of pore structures and pore size distribution was studied (Schechter and Gidley 1969). Schechter and Gidley discovered that the larger pores respond to acid reaction more and the smaller pores receive little acid sensitively by the change in pore size distribution. A model based on capillary tube approach to predict wormhole population density was developed by modeling the near wormhole pressure distribution (Huang et al. 1999). Another model calculated optimal acid injection rate with mode-size pore diameter as input, which can be obtained from micro-CT scanning with formation rock (Dong 2015). The limitation of these models is that they require the microscopic pore size distribution as prerequisite and these models can be sensitive to some assumed parameters (e.g. differential pressure against the wall in the wormhole).

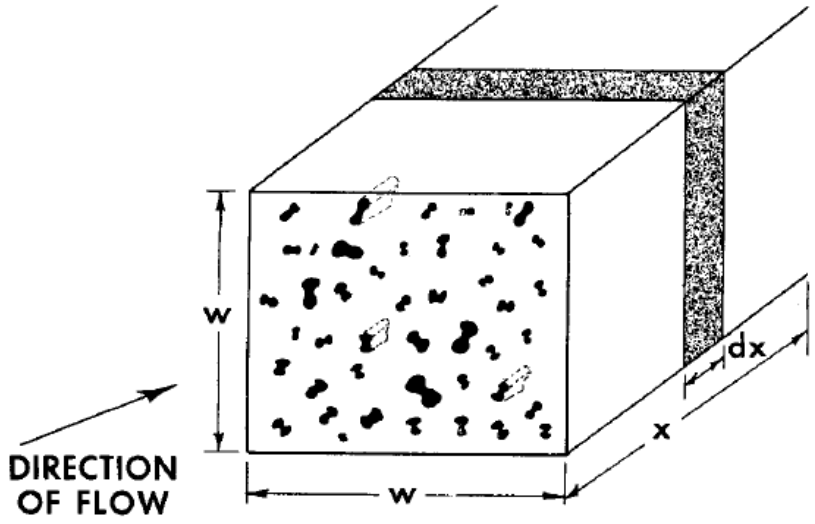

Figure 1.7 Capillary model of a porous medium (Reprinted from Schechter 1969)

1.2.3.2 Transition Pore Theory

The transition pore theory was developed to calculate $V_{i,opt}$ by incorporating maximum pore diameter as a parameter for wormhole initiation (Wang et al. 1993). They stated it requires some pores larger than the transition pore size to form a dominant wormhole. This method is limited by the difficulty of obtaining microscopic pore size description as input.

1.2.3.3 Damkohler Number Model

The effects of reaction and transportation on the wormholing process was studied with a wide range of reactive fluids (Fredd and Fogler 1999). The Damkohler number is defined as the ratio of acid reaction rate to acid transportation rate by convection. Their investigations indicate that the Damkholer number of 0.29 exists for all known fluid-mineral systems. But the application of this model is limited since the wormhole density and dimensions are required to run the model.

1.2.3.4 Peclet Number Model

Fractal theory and Peclet number was used to study wormhole propagation (Daccord et al. 1989, 1993). Peclet number is defined the as the ratio between convection transport and diffusion transport. They concluded that the dimensionless wormhole growth rate is proportional to Peclet number to the power of -1/3. For linear or cylindrical geometries, they determined wormhole growth rate is proportional to the injection rate to the power of 2/3. This approach is not practical since is only valid when the acid flux is larger than the optimal acid flux.

1.2.3.5 Network Model

The network approach was used to study the wormholing process, where the interconnectivity of the pore system (Figure 1.8) is included (Hoefner and Fogler 1988). They stated that the pore evolution is controlled by the Damkohler number. The influence of Damkohler number was studied using a 3D representative network model (Fredd and Fogler 1998).

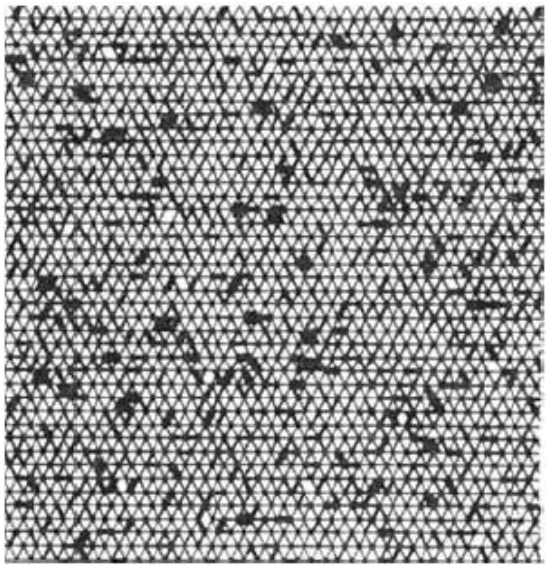

Figure 1.8 2D network model built for limestone (Reprinted from Hoefner and Fogler 1988)

1.2.3.6 Semi-empirical Model

A semi-empirical model was adopted to calculate the wormhole penetration depth (Buijse and Glasbergen 2005). Unlike linear core flooding, the wormhole growth rate decreases as wormhole length increases in radial geometry. This model requires two key parameters, $PV_{bt,opt}$ and $V_{i,opt}$, as inputs. The model predicts the skin evolution during matrix acidizing of the well. Optimal interstitial velocity and optimal pore volume to breakthrough can be obtained in the laboratory. The match of historical laboratory measurements of matrix acidizing with this model was illustrated by Buijse and Glasbergen (2005) (Figure 1.9). This model was extended by accounting for core-size dependencies and tip velocity of wormhole growth (Furui 2010). With corrected breakthrough pore volume, Furui's model explains the extremely negative skin factors that observed in the field.

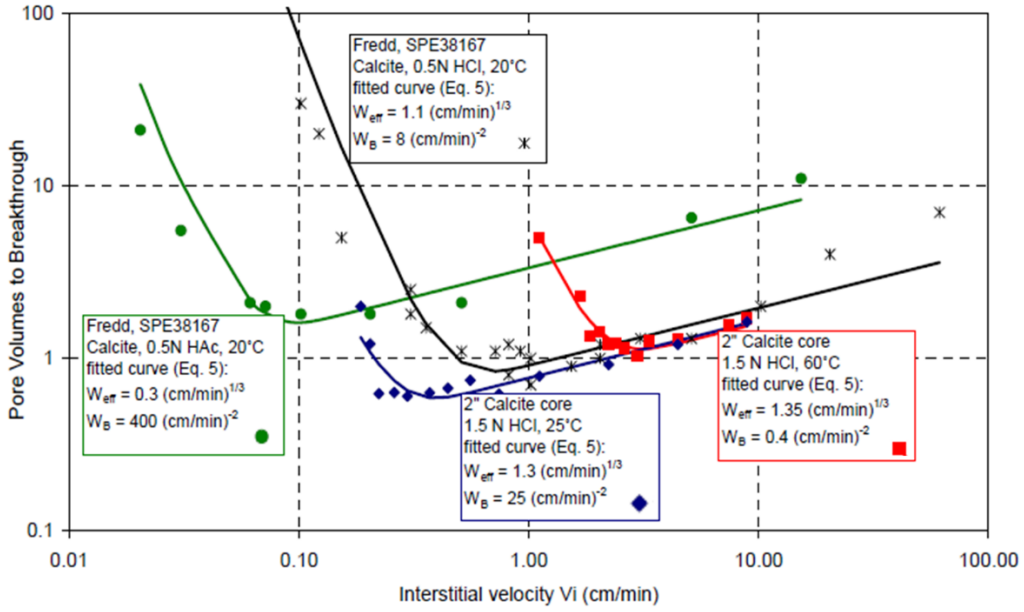

Figure 1.9 Core acidizing results matched with the semi-empirical model (Reprinted from Buijse and Glasbergen, 2005)

1.2.3.7 Averaged Continuum Model

The Averaged Continuum Model consists of the continuum equations for conservation for mass, momentum and chemical species. It couples with the evolution of petrophysical properties (e.g. permeability, pore radius, and specific surface area). This model was developed by several researchers (Golfier et al., 2001, Panga at al., 2005, Maheshwari et al., 2012, Schwalbert, 2017) and is flexible, including different kinds of rock/fluid systems, simulation geometry and also the distribution of petrophysical properties. It predicts the dissolution pattern of carbonate rocks well and can also provide a reasonable estimation of laboratory measurement optimal conditions, but this model is time-consuming and computationally expensive. The simulated dissolution pattern for matrix acidizing (Figure 1.10) with various injection rates was calculated by Schwalbert et al. (2017). As the injection rate increases, the dissolution pattern evolves from face dissolution where a thick wormhole is created to a conical wormhole whose wormhole diameter is reduced. When the injection rate reaches the optimal injection rate, the dominant wormhole is generated. High injection rates creates a ramified wormhole whose wormhole efficiency is impaired.

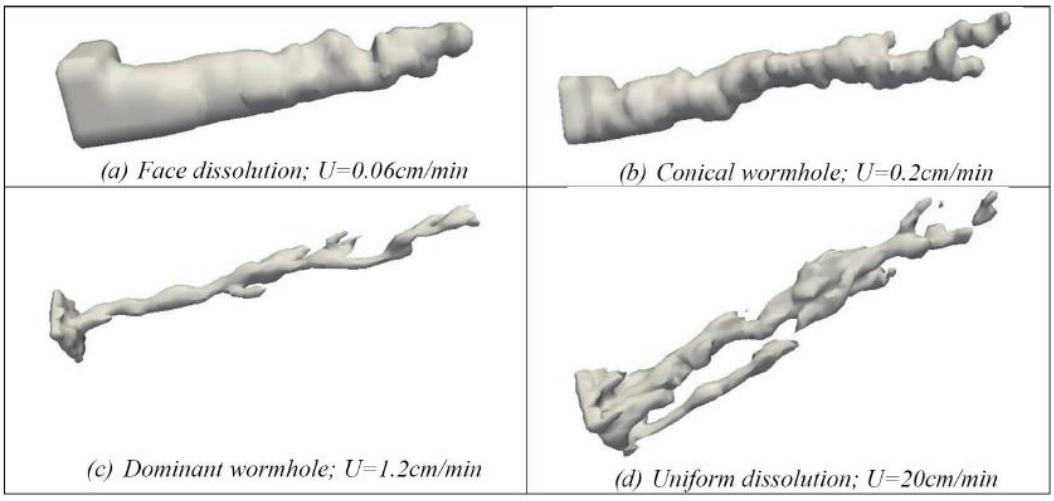

Figure 1.10 Simulated dissolution pattern with various injection rate (Reprinted from Schwalbert et al. 2017)

1.2.4 Application to Horizontal Wells

Horizontal wells can increase reservoir exposure to the wellbore, enhance production rate and reduce potential water-coning risk. Formation damage caused by drilling and completion impairs the productivity of horizontal wells. Matrix acidizing can be applied to horizontal wells to remove formation damage and enhance productivity, but it is challenging due to many reasons, including the heterogeneity of formation properties (e.g. porosity, permeability, and lithology) along the wellbore.

A integrated stimulation strategy was introduced for thick carbonate reservoirs penetrated by deviated wells based on the rock type characterization by geological description, well log analysis, core measurements, and thin section description (Abou-Sayed et al. 2007). Their work suggests that integrating the rock petrophysical properties is an essential step to improve the success of matrix acidizing. Integrating the formation evaluation technique into the simulation of matrix acidizing in horizontal wells was recommended to improve the acidizing design with better-characterized formation petrophysical properties (Ueda 2015).

1.3 Objective and Approach

The objective of this research is to investigate the influence of pore structure and petrophysical properties (porosity, permeability, etc.) on the optimal conditions of matrix acidizing at multiple scales. In this study, more rock types and rock samples were investigated, extending Etten's research (Etten 2015).

The approaches were tested with both experimental analysis and numerical processing from different scales. Multiple properties of the pore system in different type of carbonate rocks are examined. At the micro-scale, micro-CT techniques were adopted to capture the characteristics

of pore structures, then pore size distribution and other related properties of carbonate rocks were calculated based on digital image processing. At the core-scale, the optimal conditions for Travertine, a highly heterogeneous and anisotropic carbonate rock is obtained with laboratory experiments and compared with optimal conditions from previous matrix acidizing experiments. Finally, the relationship between the optimal conditions and pore structure properties are established, and the petrophysical properties are integrated into horizontal well acid stimulator (HWAS) to improve the matrix acidizing design at the log scale for field application.

1.4 Dissertation Outline

The background for the this study, related literature review, the objective and approaches are outlined in Figure 1.11.

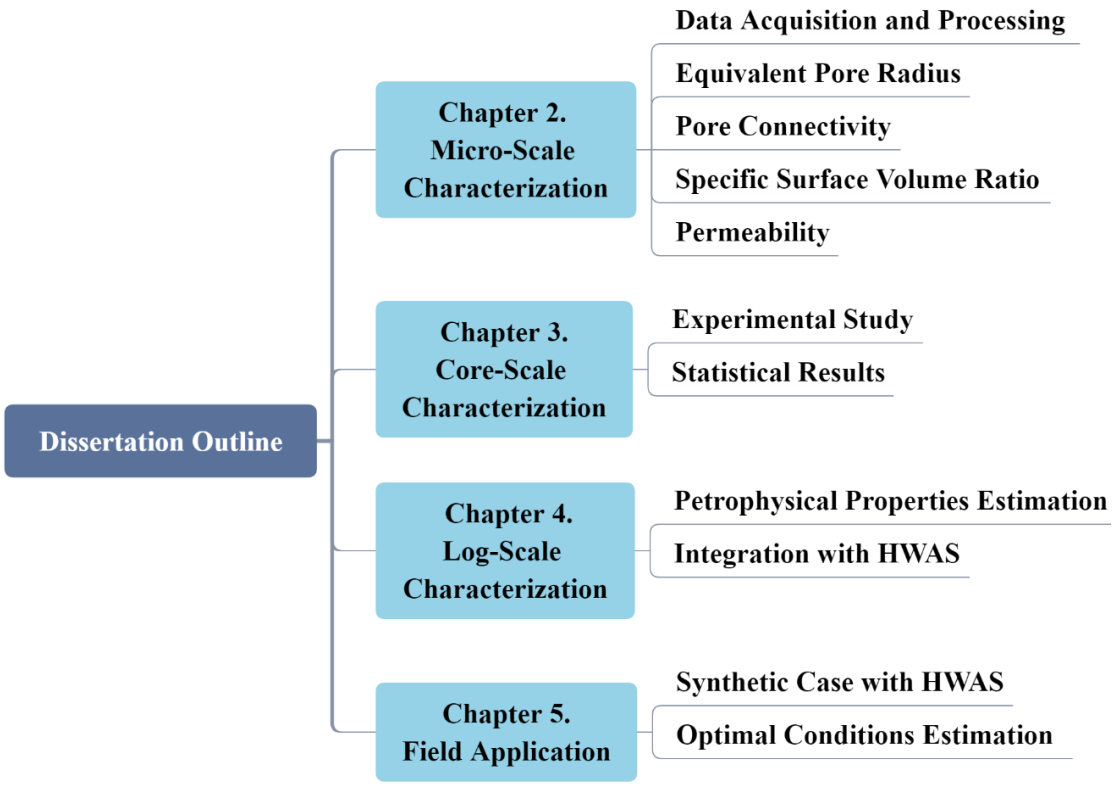

Figure 1.11 Dissertation outline

In Chapter 2, formation characterization for matrix acidizing at the micro-scale is performed. The contents of Chapter 2 include sample collection, data acquisition with micro-CT technique, image processing with software and Matlab code. The relationship between the calculated pore size distributions, pore connectivity, specific surface ratio and the optimal conditions for each rock is investigated.

In Chapter 3, formation characterization for matrix acidizing at the core-scale is determined. The experimental setup for optimal conditions is introduced. Statistical results for available experiments are generalized to demonstrate the common characteristics of optimal conditions for different types of carbonate rocks.

In Chapter 4, the formation characterization for matrix acidizing at the log-scale is determined. The procedures for petrophysical analysis are introduced, including the estimation of formation porosity, mineralogy and permeability. The estimated petrophysical properties are integrated into the horizontal well acid stimulator (HWAS) as relevant module. Field application of the improved HWAS is discussed.

In Chapter 5, a synthetic case based on field data is demonstrated. The simulation results indicate that the heterogeneity of petrophysical properties along the wellbore plays an important role for a success matrix acidizing treatment. Methodology of estimating optimal conditions with permeability and equivalent pore radius are introduced and examples are given.

Chapter 6 provides the conclusions of all the studies from different scales (Chapter 2-5) for matrix acidizing.

2. FORMATION CHARACTERIZATION AT MICRO-SCALE

2.1 Introduction

Determination of optimal conditions for specific acid/rock systems is crucial for successful acid matrix acidizing design. An insufficient acid injection rate can cause acid wasted to be wasted reacting with carbonate rock near the wellbore but not creating deep penetration into the formation. To better understand how the pore structures, affect the optimal conditions, a detailed description for different carbonate rock types is needed. To achieve that, micro-Computed Tomography (micro-CT) is used to image the rock samples tested for optimal conditions since it is a widely used non-destructive technique. The internal properties of the pore structures can then be visualized and quantified to investigate their relationship with optimal conditions.

2.2 Data Acquisition and Image Processing

2.2.1 Data Acquisition

Seven different carbonate rock samples were collected from outcrops, including Indiana Limestone, Desert Pink (from a Lower Cretaceous unit in Texas), and Travertine (from Italy). Indiana Limestone and Desert Pink were prepared as 1.5-inch diameter by 8-inch length core plugs to measure the porosity gravimetrically and measure permeability using flooding experiments (Etten 2015). The experimental setup and procedure are introduced in detail in Chapter 3. The Travertine was prepared as 1.5-inch diameter by 6-inch length core plugs, the porosity and permeability are measured with same method in this study (some core flooding experiments were performed by Haoran Cheng). The experimental results for measured porosity and permeability of these seven samples are shown in Table 2.1.

Table 2.1: Measured porosity and permeability for studied rocks

Rock Type	Sample Name	Porosity, v/v	Permeability, md
Indiana Limestone	Indiana Limestone_1	0.15	6
	Indiana Limestone_2	0.15	8
	Indiana Limestone_3	0.13	10
	Indiana Limestone_4	0.16	239
Travertine	Travertine_1	0.07	99
	Travertine_2	0.09	600
Desert Pink	Desert Pink	0.30	33

After core flooding test, we cut the rock samples into 1 cm^3 cubes for micro-CT scanning. The micro-CT scanner is a Phoenix nanotom (Figure 2.1).

Figure 2.1 Phoenix nanotom Micro-CT scanner

The resolution of scanning for each sample are slightly adjusted to ensure the best imaging quality, the resolution range is 5.0 um/pixel to 8 um/pixel. After scanning we exported the generated greyscale image slices into an open-source software Fiji (Schindelin et al. 2012) to perform image-processing.

2.2.2 Image Processing

The image-processing consists of several steps. The first step is to select a region of interest from the raw images to reduce the noise and artifacts produced during scanning. A exported raw image from micro-CT scanner is shown as Figure 2.2a. The pore space is shown in grayscale and it is hard to distinguish it from matrix visually. We selected a square shape of area inside the grayscale rock slices (Figure 2.2a) as a region of interest (Figure 2.2b) to preserve as much useful information as possible. The resolution for the region of interest is between 1695×1662 pixels to 1425×909 pixels for different rock types (Table 2.2).

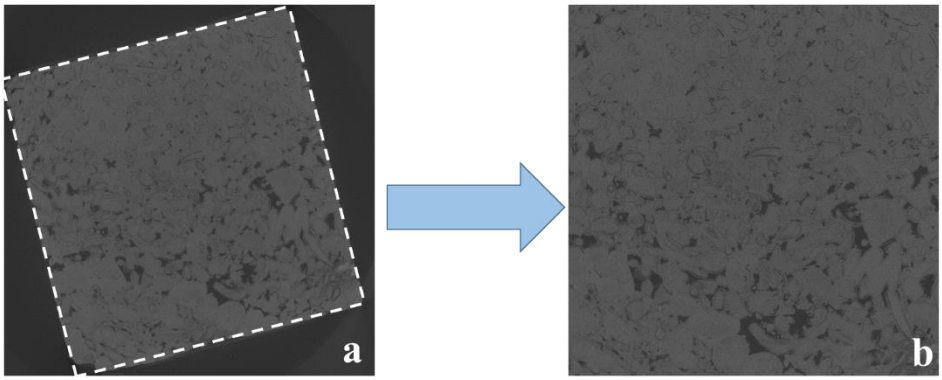

Figure 2.2 Image slice of Indiana limestone sample exported from micro-CT scanner(a), selected region of interest(b)

Table 2.2. Image size, resolution and calculated porosity

Sample Name	IMG_Size_X, pixel	IMG_Size_Y, pixel	IMG_Size_Z, pixel	Resolution, um/pixel	Por_Image, v/v	Por_Lab, v/v
Indiana Limestone_1	1695	1662	118	6.50	0.15	0.15
Indiana Limestone_2	1425	909	90	5.00	0.16	0.15
Indiana Limestone_3	1659	1713	90	6.50	0.13	0.13
Indiana Limestone_4	1362	1350	98	8.00	0.16	0.16
Travertine_1	1494	1434	99	7.60	0.08	0.07
Travertine_2	1635	1578	130	7.50	0.10	0.09
Desert Pink	1440	1426	90	8.00	0.28	0.30

For each 1 cm^3 rock sample, over 1000 image slices were scanned and exported. 100 image slices were selected for each sample to conduct further processing since the size of 1000 image slices is over 10 GB, which exceeds the capacity of image processing software. The next step was to perform thresholding for the selected images to distinguish the pores from the limestone matrix, this is the most important step in image processing.

Thresholding is a certain value of cutoff selected from the scanned images, which can automatically sort the pixels with a higher value than this cutoff into one group and the rest as another group. This process is also called image binarization since after this, pixels are either black or white, which are represented by numerical value 1 or 0, respectively. A histogram is always used for choosing the cutoff. The histogram of one image slice and its thresholding cutoff is shown on the upper right corner of Figure 2.3. The thresholding cutoff value is determined by using Huang's model (Huang and Wang, 1995). The area colored red are the identified pore spaces.

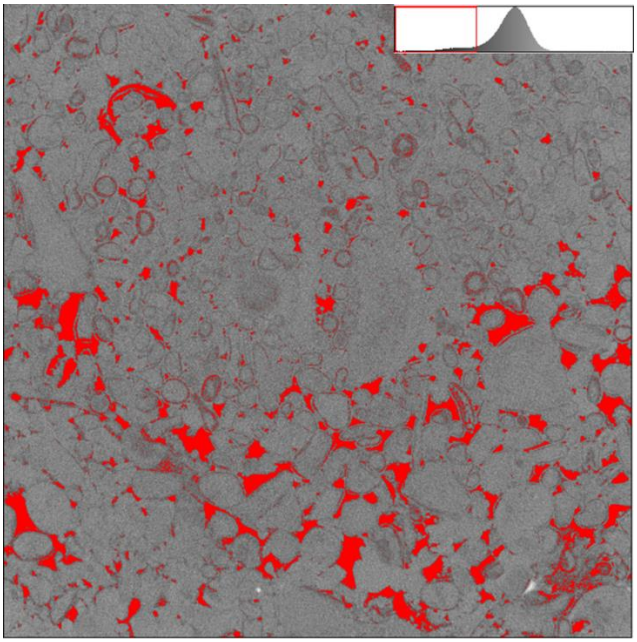

Figure 2.3 Example of identified pore space with thresholding for Indiana limestone sample (histogram on the upper right corner, pores are colored red)

Several thresholding algorithms were reviewed for processing X-ray CT image segmentation for porous media (Iassonov 2009). Iassonov concluded that fuzzy thresholding techniques, including Huang's model, are more robust for porous medium with complex structure and potential noise on the CT image. The basic principle for Huang's model is, a membership function is assigned to each pixel in an image to represent the relationship between its belonging binarized region and itself. The index of fuzziness can be measured by using Shannon's entropy or Yager's measure, which uses the assigned membership functions as inputs. The optimal thresholding value minimizes the index of fuzziness by measuring the distance between the gray scale image and the binarized image (Huang and Wang, 1995). The binarized images are colored black and white by using Huang's model (Figure 2.4). Pore space is colored black and rock matrix are colored white.

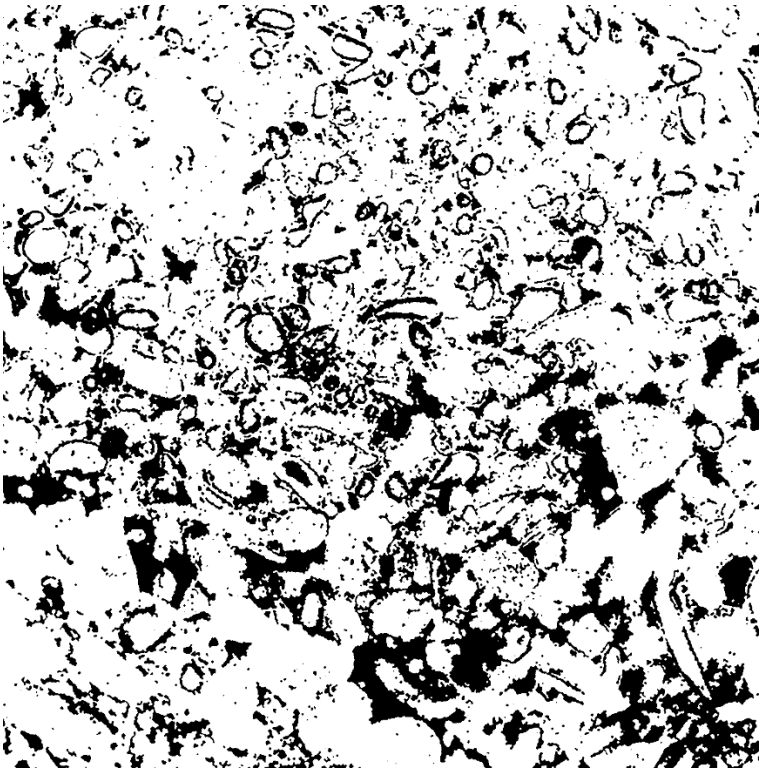

Figure 2.4 Binarized image slice for Indiana limestone where black is pore space and white is rock matrix

After image thresholding, noise was further reduced since sometimes it was difficult to completely distinguish pore space from matrix. The *Despeckle* function in Fiji software was used to remove the noise data. This process was repeated several times until the porosity calculated from binarized images matched the laboratory-measured porosity, which was selected as a benchmark to cross-validate if the image processing reflects the real rock properties. The porosity for the digital rock is calculated by adding the pixel number of pore spaces colored black for a set of image stacks then divided these pixels by the pixel volume of the image stack. The calculated "digital porosity" and total porosity previously measured gravimetrically in the laboratory are close to each other (Table 2.2), indicating the image processing is qualified for property quantification in the next step. In summary, the image processing steps include raw data import, selection of region of interest, thresholding, despeckle, and quality control with porosity.

The image processing procedures are implemented for all seven rock samples, including Indiana limestone with permeability of 6 md, 8 md, 10 md, 239 md; Travertine with permeability of 99 md, 600 md; Desert Pink rock with permeability of 33 md (Figure 2.5a to Figure 2.5g). It is clear on the binarized images that the tested rocks have quite different pore structures. Indiana limestone samples are calcitic oolitic grainstone with clear intergranular pores, whereas Travertine has large, sparse and irregular shape pores. The quantification in the following sections can further describe the characteristic of the pore structures.

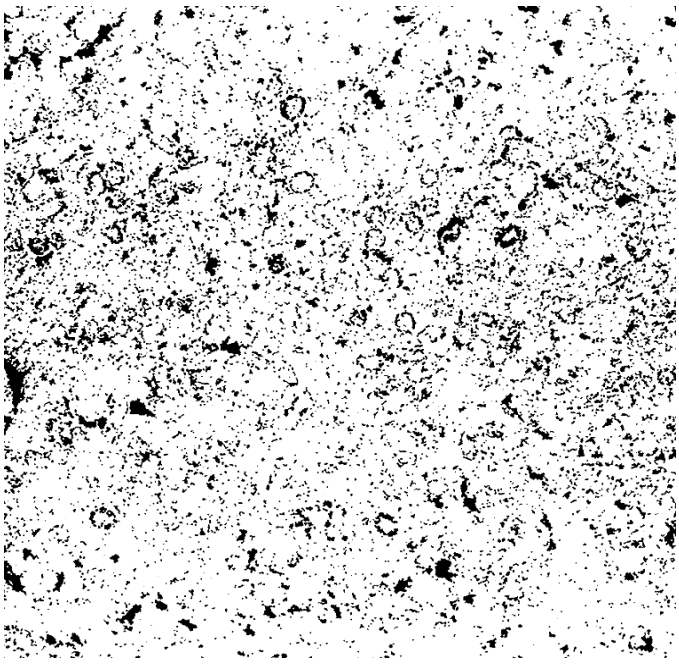

Figure 2.5a The processed binary images of scanned 6 md Indiana limestone (pores are colored black)

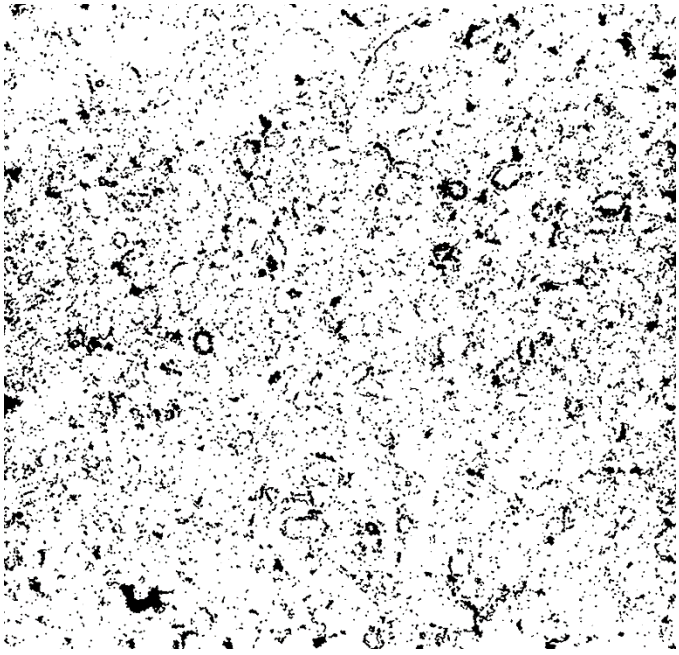

Figure 2.5b The processed binary images of scanned 8 md Indiana limestone (pores are colored black)

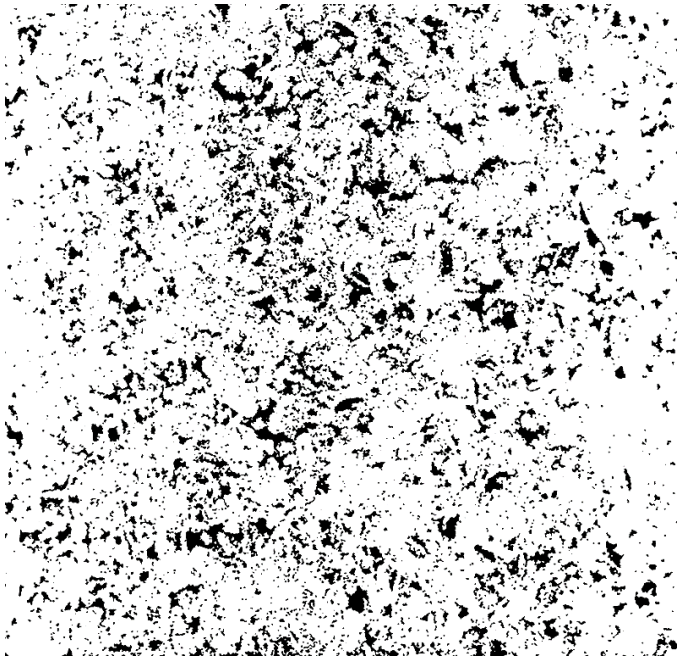

Figure 2.5c The processed binary images of scanned 10 md Indiana limestone (pores are colored black)

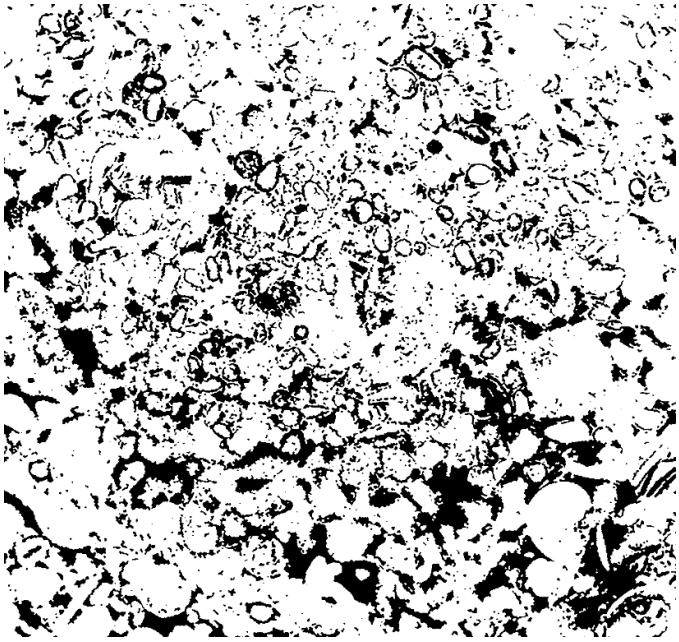

Figure 2.5d The processed binary images of scanned 239 md Indiana limestone (pores are colored black)

Figure 2.5e The processed binary images of scanned 99 md Travertine (pores are colored black)

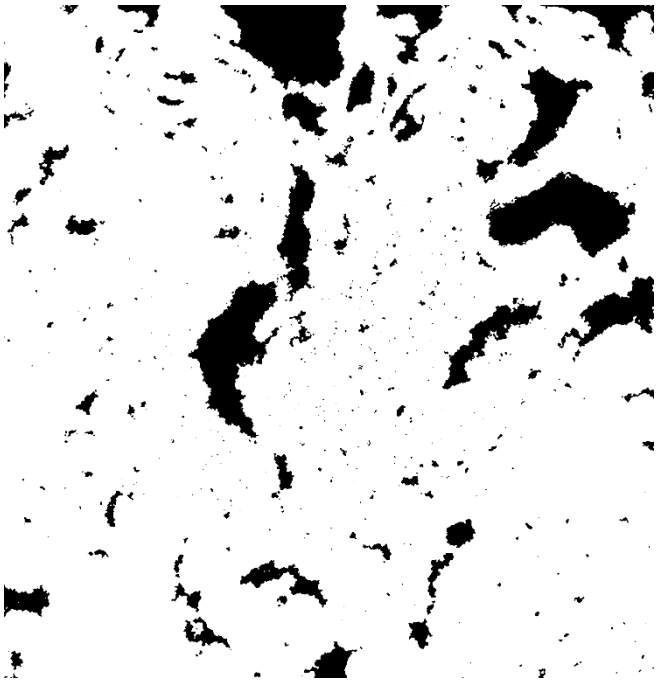

Figure 2.5f The processed binary images of scanned 600 md Travertine (pores are colored black)

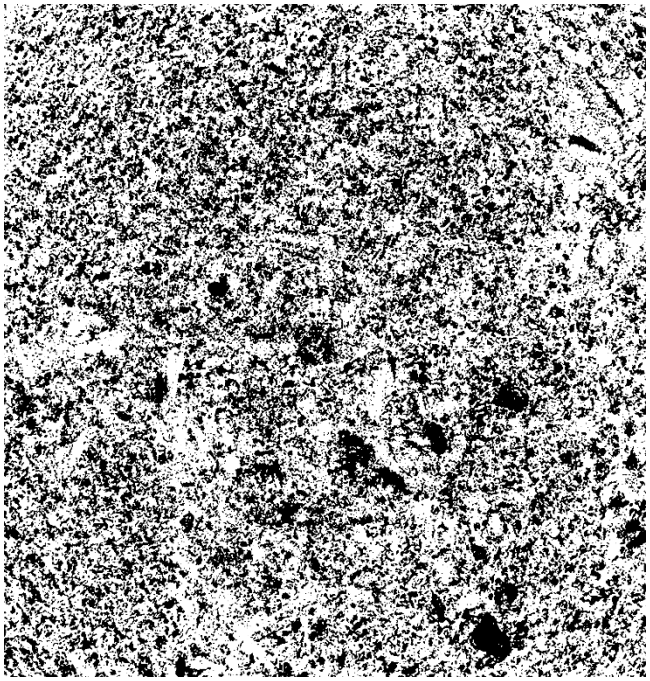

Figure 2.5g The processed binary images of scanned 33 md Desert Pink (pores are colored black)

2.3 Characterization of Pore Size Distribution

Researchers use pore size distribution to characterize the pore space of carbonate rocks, the related techniques include high pressure mercury injection (HPMI), micro-CT scanning and nuclear-magnetic-resonance (NMR) measurements since they are closely correlated with the flowing characteristics in the porous media. Based on the processed binary image data, we chose about 100 continuous image slices out of the 1000 image stack as representatives for each rock sample to calculate the pore size distribution. Based on the processed binary images, we can easily calculate the arithmetic pore radius for every single pore, and obtain the average arithmetic pore radius R_a for each rock as:

$$R_a = \frac{\sqrt{\frac{A_1}{\pi}} + \sqrt{\frac{A_2}{\pi}} + \sqrt{\frac{A_3}{\pi}} + \cdots + \sqrt{\frac{A_n}{\pi}}}{n} \tag{2.1}$$

where A_1, A_2, A_3 are the area of each pore on one 2D image slice, n is the total number of pores on one image slice.

With average pore radius, we used lognormal distribution to describe the pore size distribution for each rock sample. The probability function is given by:

$$P(x) = \frac{1}{x\sigma\sqrt{2\pi}} \exp\left(-\frac{(\ln x - \mu_1)^2}{\sqrt{2}\sigma}\right) \tag{2.2}$$

where x is the pore radius, σ is the variance of the pore radius and μ_1 is the mean value of the radius of pores. The arithmetic pore radius for all the pores in each 2D image stack (Figure 2.6), the pore size distributions for different samples overlapped and hard to distinguish one from each other.

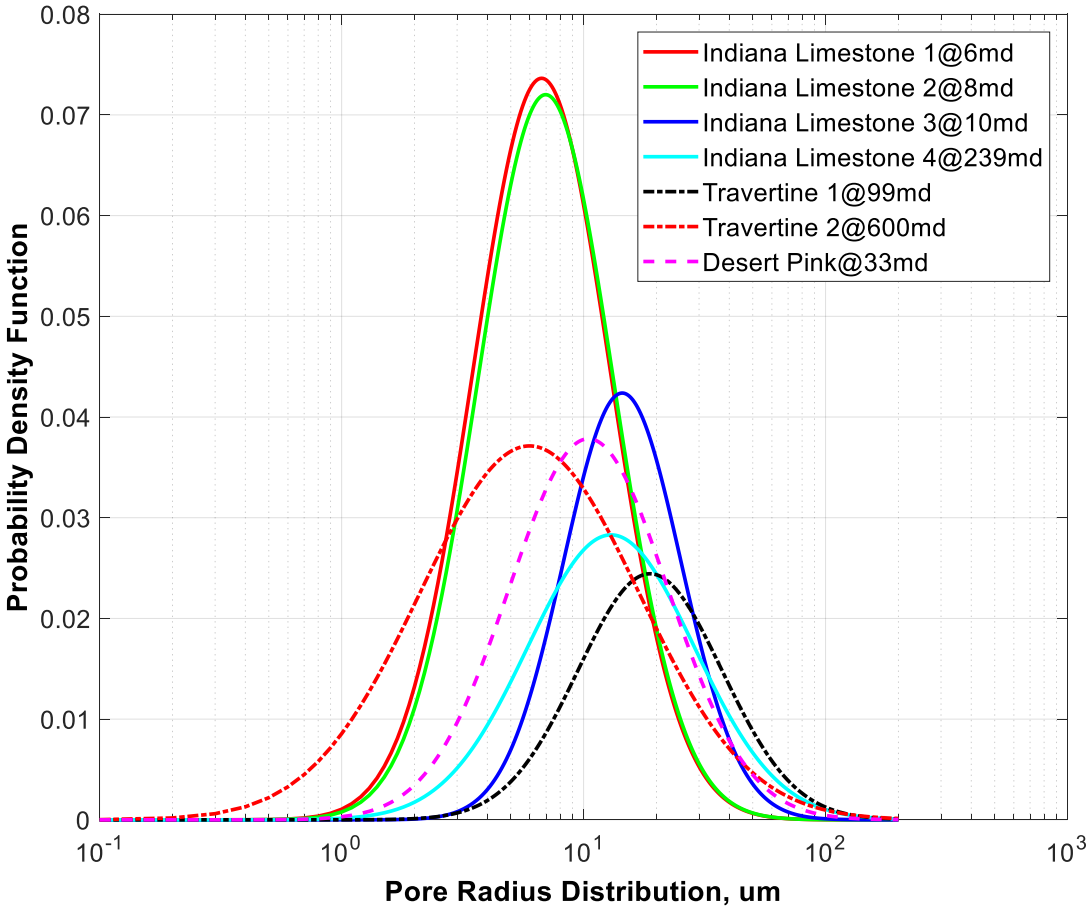

Figure 2.6 The pore radius distribution of all pores accounted for all the rock samples

By plotting the arithmetic average pore radius against the laboratory-measured permeability in Figure 2.7, we observe that as average arithmetic pore radius increases, permeability increases. But the correlation between them is scattered, indicating the average arithmetic pore radius is weakly correlated to permeability.

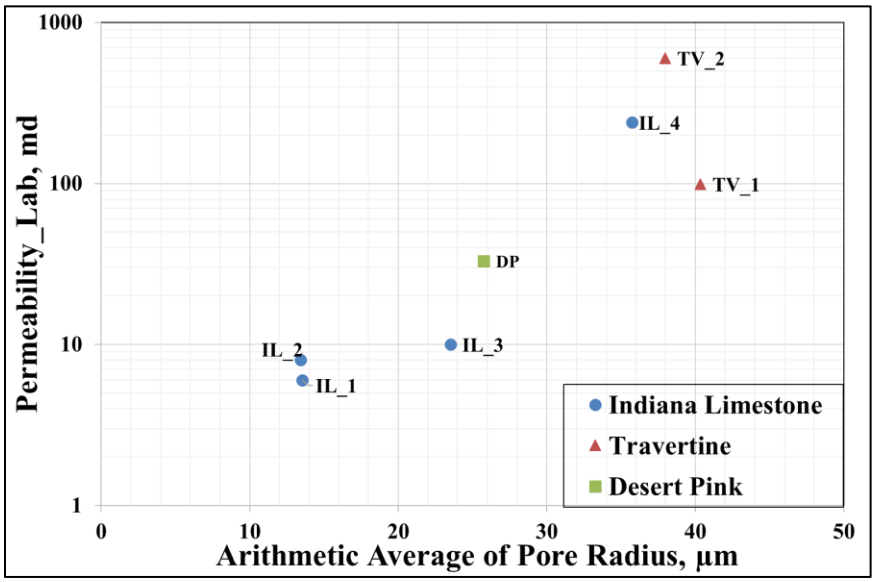

Figure 2.7 The arithmetic average value of pore radius against rock permeability

Based on the processed micro-CT images, we define a new concept named equivalent pore radius, R_e, as Equation 2.3.

$$R_e = \sqrt{\frac{A_1 + A_2 + A_3 \ldots + A_n}{\pi \cdot n}} \tag{2.3}$$

where A_1, A_2, A_3 are the area of each pore on one 2D image slice, n is the total number of pores on one image slice.

Figure 2.10 is an illustration of this concept. For every single 2D slice image (e.g. Image slice 1 in Figure 2.8), we first calculate the total area of all pores (e.g. the number of pores for each image is n) regardless of the size of the pores. Then we assume there is n virtual pores sharing the

same pore radius R_e that can generate the same total area for each image. For every single 2D slice, one equivalent pore radius can be calculated as the representative (e.g. R_{e_1} in Figure 2.8). With the 2D image stack, the equivalent pore radius for each rock image slice is calculated as $Re_{\_1}$, $Re_{\_2}$,…, R_{e_n}. After that the equivalent pore radius distribution for each rock sample is generated.

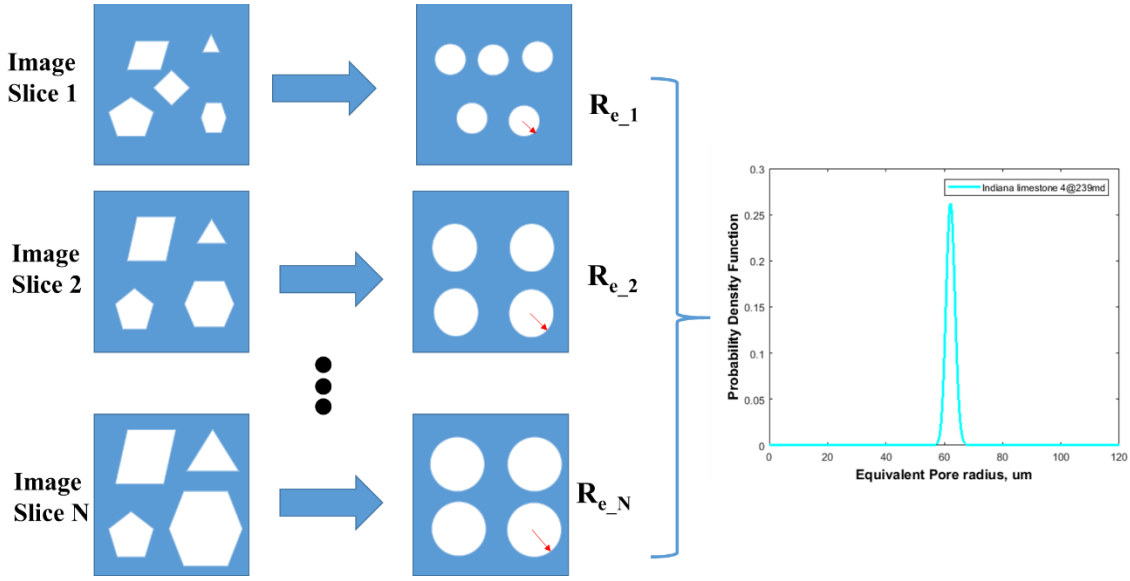

Figure 2.8 Concept of equivalent pore radius R_e

Indiana limestone sample 4, with permeability of 239 mD, was used as example, where the 98 binarized image slices are selected and there are about 2300 pores identified on each image slice (Table 2.3). For each slice, the average area of pores can be calculated by dividing total area of pores by the count of pores. Assuming the equivalent pore has circular shape, the equivalent pore radius for the first image slice Indiana_limestone_4_1 is calculated with Equation 2.4.

$$R_{e\_1} = \sqrt{\frac{Average\ Area_1}{Pore\ Count_1}} \times Resolution = \sqrt{\frac{444126\left(pixel^2\right)}{2254}} \times 8\left(\mu m / pixel\right) = 63.36\mu m \quad (2.4)$$

The equivalent pore radius for the remainder of the image slices can be calculated with the same method. Then the probability density function for Indiana limestone sample 4 is calculated

as Figure 2.9. The mean value for the calculated equivalent pore radius for Indiana limestone sample 4 is 62.2 μm.

Table 2.3 Identified pore area of Indiana limestone sample 4 image slices

Slice #	Pore Count	Total Area, pixel^2	Average Area, pixel^2	Resolution, μm/pixel	R_e, μm
Indiana_limestone_4_1	2254	444126	197.04	8	63.36
Indiana_limestone_4_2	2282	442573	193.94	8	62.86
Indiana_limestone_4_3	2226	444265	199.58	8	63.76
Indiana_limestone_4_4	2231	444445	199.21	8	63.71
Indiana_limestone_4_5	2240	443644	198.06	8	63.52
Indiana_limestone_4_6	2324	442014	190.20	8	62.25
Indiana_limestone_4_7	2311	441769	191.16	8	62.40
Indiana_limestone_4_8	2294	442468	192.88	8	62.68
Indiana_limestone_4_9	2345	441147	188.12	8	61.91
…	…	…	…	…	…
…	…	…	…	…	…
…	…	…	…	…	…
Indiana_limestone_4_97	2334	438232	187.76	8	61.85
Indiana_limestone_4_98	2356	438600	186.16	8	61.58

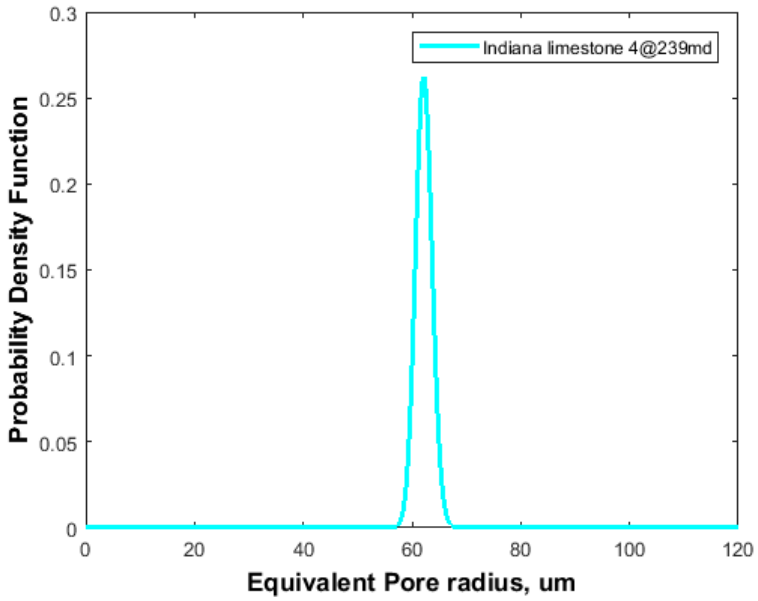

Figure 2.9 Probability function of the calculated equivalent pore radius for Indiana limestone sample 4

Following the same method for Indiana limestone sample 4, probability density function of the equivalent pore radiuses for the other rock samples is generated as Figure 2.10. The distribution of equivalent pore radius can separate different rock sample.

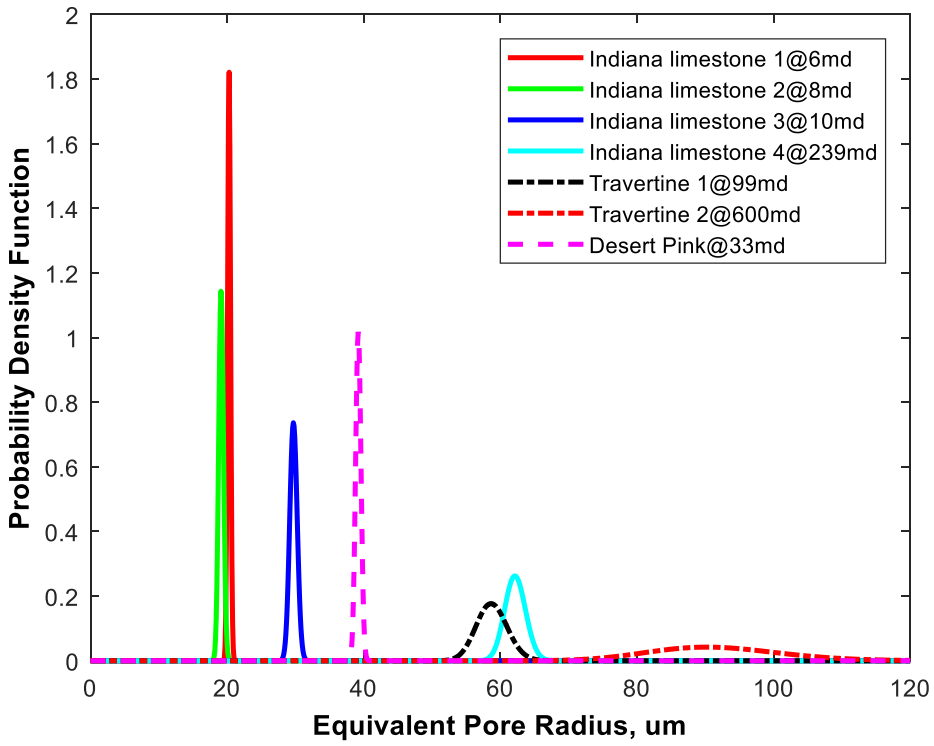

Figure 2.10 Probability function of the calculated equivalent pore radius for all rock samples

Next, we take the mean value of the equivalent pore radius for each rock sample as the representative to correlate with permeability. Figure 2.11 gives the relationship between the mean values of equivalent pore radius against laboratory-measured permeability for all rock samples tested in this study. The equivalent pore radiuses are highly related to the permeability measured in the laboratory, indicating many small pores are not contributing to the fluid flow in the tested rocks comparing with Figure 2.7 since a great proportion of small pores are filtered out through the calculation of equivalent pore radius.

Table 2.4 explains the "filtering" effect of the equivalent pore radius. Assuming there are 3 binarized image slices and each of them has 11 pores on them, the total area for each image slice are the same, so is the average area of each pore. One of the rocks is ideally homogeneous, the other two image slices have an increasing degree of heterogeneity, which is indicated by the standard deviation. These three image slices share the same equivalent pore radius of 7.98 μm, but as the degree of heterogeneity increases, the mean pore radius decreases. The mean pore radius for heterogeneous rock sample 2 is 7.31 μm, indicating that many of the small pores are having the same weight as big pores. This causes the increased scatter on Figure 2.7.

Table 2.4 Explanation of equivalent pore radius concept

	Area of Homogeneous Rock,um^2	Area of Heterogeneous Rock 1,um^2	Area of Heterogeneous Rock 2,um^2
Pore #1	200	100	10
Pore #2	200	120	30
Pore #3	200	140	50
Pore #4	200	160	100
Pore #5	200	180	150
Pore #6	200	200	200
Pore #7	200	220	250
Pore #8	200	240	280
Pore #9	200	260	300
Pore #10	200	280	350
Pore #11	200	300	480
Total Area, um^2	2200	2200	2200
Average Area, um^2	200	200	200
Area STD, um^2	0.00	66.33	148.26
Mean Pore Radius, um	7.98	7.87	7.31
Equivalent Pore Radius, um	7.98	7.98	7.98

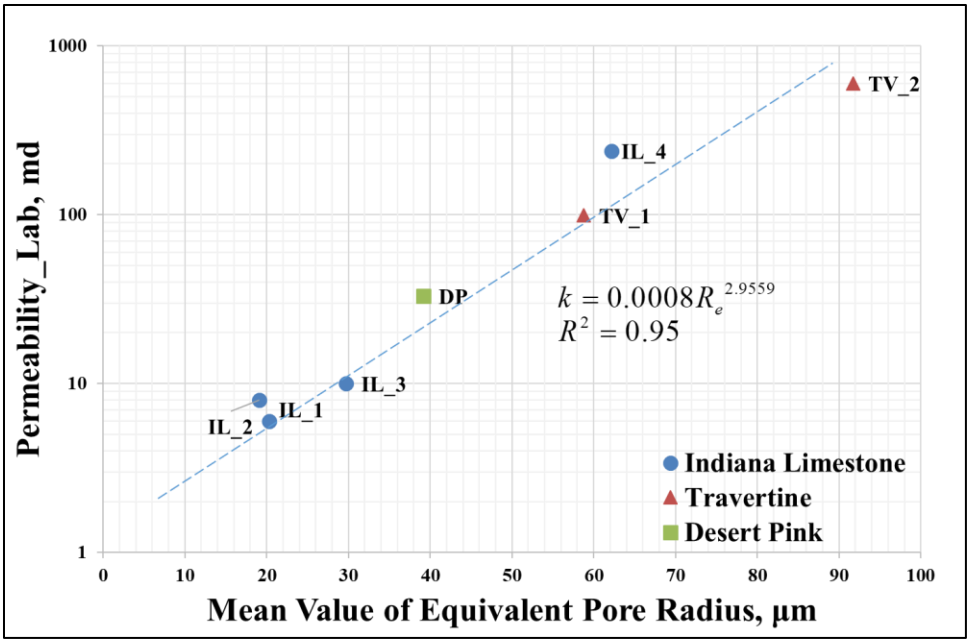

Figure 2.11 Relationship between the calculated mean values of equivalent pore radius against the measured permeability

The correlation between the mean value of equivalent pore radius and permeability is given by Equation 2.5, which can be used for permeability estimation for the tested rock samples for a range of more than two orders of magnitude.

$$k = 0.0008R_e^{2.9559} \tag{2.5}$$

where k is permeability in md, and R_e is the equivalent pore radius in μm.

The equivalent pore radius also reflects the heterogeneity of the pore sizes for each rock. For relative homogeneous rock, the equivalent pore radius is closer to the arithmetic average pore radius. Equivalent pore radius is much higher than the arithmetic average pore radius for heterogeneous rock. We also calculate the arithmetic average pore radius of the top 5% percent large pores. We observe that they also are highly correlated to the laboratory-measured permeability (Figure 2.12).

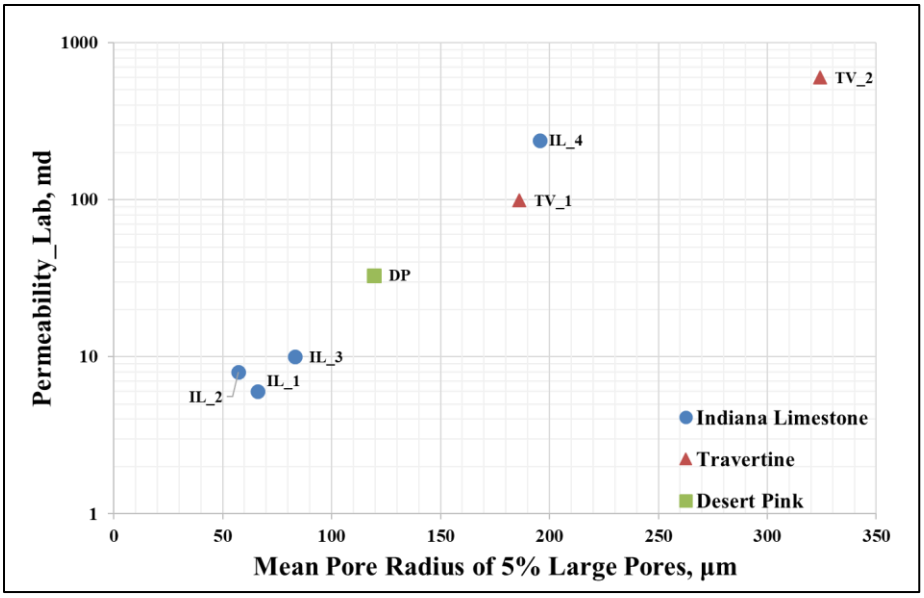

Figure 2.12 The relationship between the mean value of top 5% percent large pores against the measured permeability in the laboratory

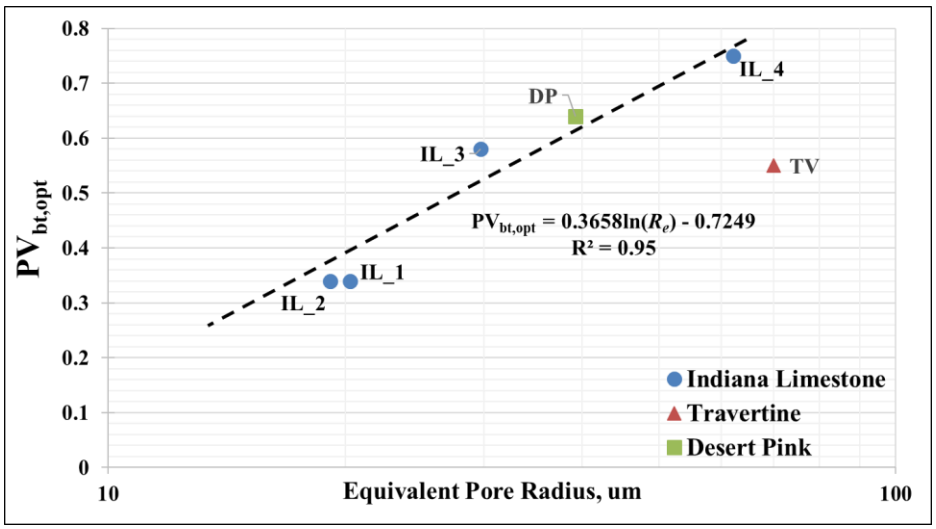

Figure 2.13 Equivalent pore radius against the optimal pore volume to breakthrough

The semi-log plot of the calculated equivalent pore radius against the optimal pore volume to breakthrough is shown in Figure 2.13. The pore volume to breakthrough is obtained from laboratory experiment, then curve-fitted with Buijse-Glasbergen model. The relationship between

equivalent pore radius and optimal pore volume to breakthrough is generated with Indiana limestone samples and Desert Pink sample as Equation 2.6. This equation may be used for estimating the optimal pore volume to breakthrough and more experimental data are needed for improvement.

$$PV_{bt,opt} = 0.3658\ln(R_e) - 0.7249 \tag{2.6}$$

We can see that the equivalent pore radius for each rock type is positively related to optimal pore volume to breakthrough with a nice correlation. Travertine also is positively related but deviated from the correlation. This result is further discussed in detail in Chapter 3.

2.4 Characterization of Pore Connectivity

Researchers have used many methods to quantify pore connectivity in porous media. The mean coordination number Z, which is a parameter transformed from rock porosity, was used to characterize the connectivity of the rock based on the three-dimensional rock image data (Bernabé et al. 2010). Water imbibition tests and molten alloy injection was used on various type of rocks to study their pore connectivity and pore network (Hu et al. 2012).

We select the topological concept of Euler-Poincare Characteristic (EPC) number to quantify the 3D pore connectivity since it is simple and can be fast applied (Vogel 1997; Chi et al. 2015). Following Vogel's method (Vogel 1997), we calculated the Euler-Poincare Characteristic number in 3D porous media based on the Euler-Poincare Characteristic number in 2D, which is defined as:

$$EPC_{2d} = N_1 - C_1 \tag{2.7}$$

where N_1 is the total number of isolated pore clusters and C_1 is the number of "holes" or "tunnels" in the isolated pore clusters. Figure 2.14 is an illustration of a 2D processed micro-CT scanned

images, the N_1 value for this image is 4 and the C_1 value is 3 for this image, thus giving a 2D Euler-Poincare Characteristic number of 1.

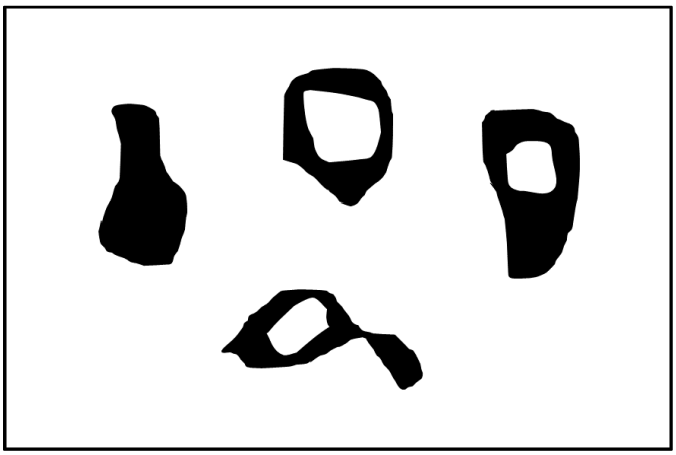

Figure 2.14 Illustration of a processed 2D micro-CT scanned images (pores are colored black)

Then we generate the 3D Euler-Poincare Characteristic number for stacks of micro-CT scanned images by applying:

$$EPC_{3D} = \sum_{i=2}^{n} EPC_{3,i} \tag{2.8}$$

The 3D Euler-Poincare Characteristic number for connectivity is directional, but we only consider the connectivity number perpendicular to the image stack as micro-CT is scanned in the same direction. An illustration of the image stack and the direction of connectivity for a Travertine sample is given in Figure 2.15. According to topological explanation, smaller 3D Euler-Poincare Characteristic number or a negative number indicate better connectivity of the pore system (Vogel 1997).

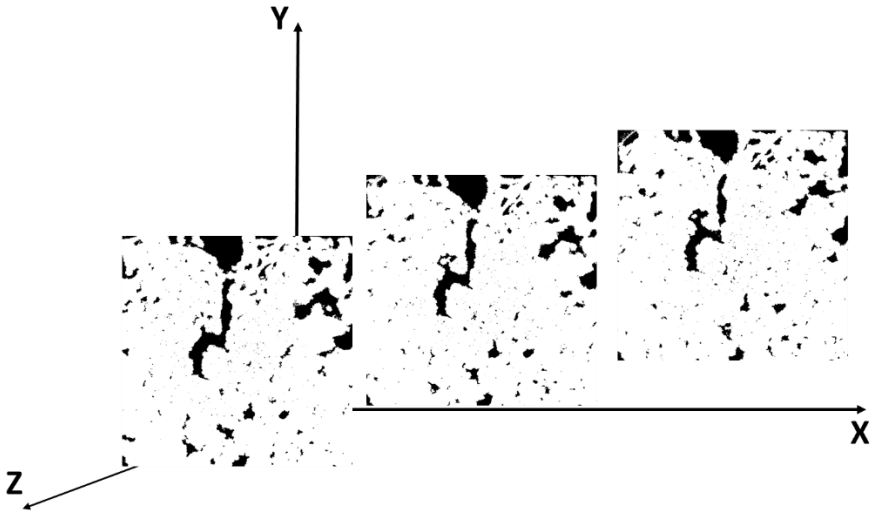

Figure 2.15 Binarized image stacks along the Z direction (pores care colored black)

The calculated connectivity against laboratory-measured permeability is plotted in Figure 2.16. Indiana limestone with a smaller connectivity number, which means it is better connected, has higher permeability. However, this relationship is scattered when more rock types are included and may not be used for correlation.

The plot of pore volume to breakthrough versus the connectivity number in unit volume is given in Figure 2.17. Optimal pore volume to breakthrough increases as connectivity number becomes smaller (indicating better connectivity). The plot of the optimal interstitial velocity versus connectivity number in unit volume is also generated in Figure 2.18. No clear trend is observed.

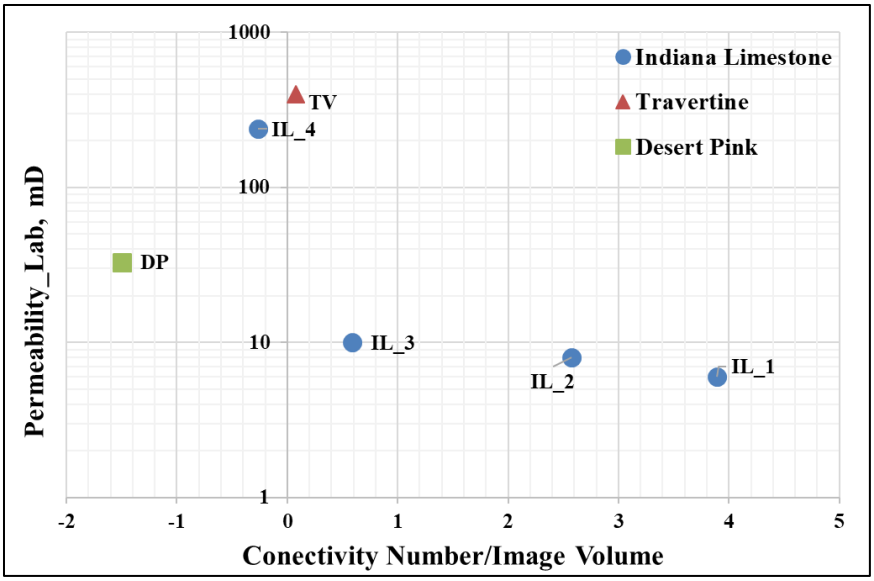

Figure 2.16 The plot of the connectivity numbers in unit volume against the laboratory-measured permeability

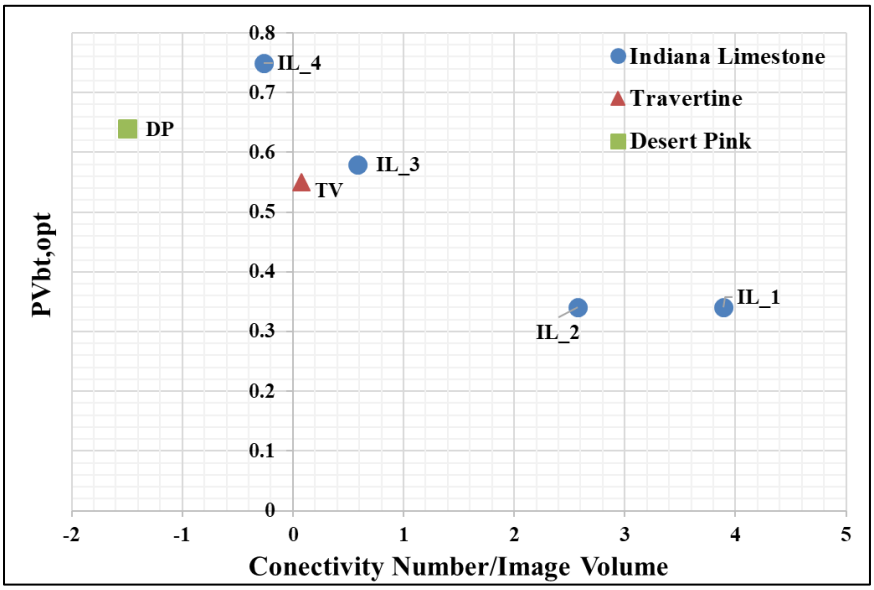

Figure 2.17 The plot of the connectivity numbers in unit volume against optimal pore volume to breakthrough

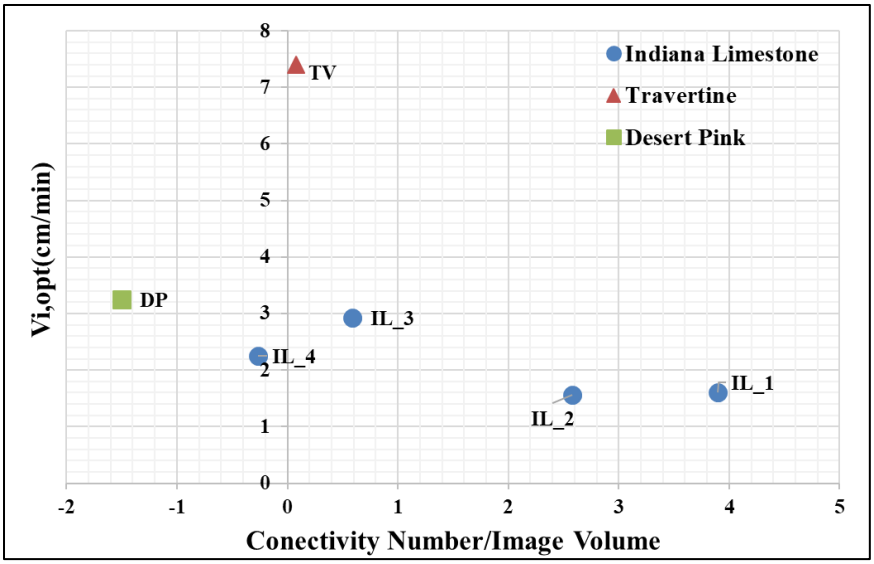

Figure 2.18 The plot of the connectivity numbers in unit volume against optimal interstitial velocity

Besides connectivity quantification by Euler-Poincare Characteristic number, we also identified the connected objects, which are the connected pore clusters for every rock sample. The pore cluster labeling technique is Hoshen-Kopelman's algorithm (Hoshen and Kopelman 1976). The binarized image stacks from scanned rock samples can generate 3D digital volume. The volume consists of voxels with value 0 or 1. Each voxel can be treated as cubic square (Figure 2.19).

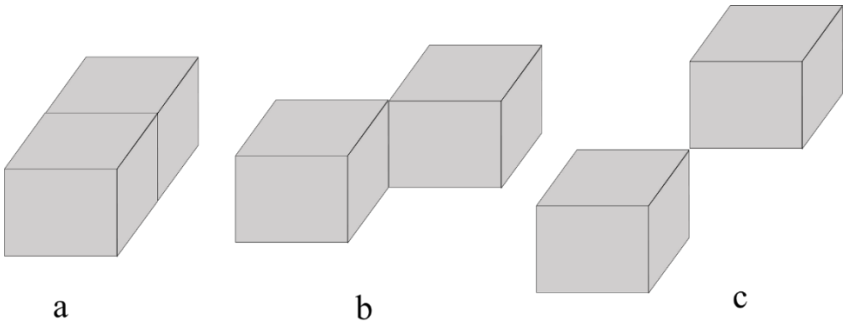

Figure 2.19 Voxel connection types

Voxels connect to each other as face-connected (Figure 2.19a), edge-connected (Figure 2.19b), and corner-connected (Figure 2.19c). Hoshen-Kopelman's algorithm scans the digital image matrix and labels the occupied voxels cell by cell. If a voxel is face-connected to neighbor voxel, it is assigned a cluster label and no label would be assigned to a cell that is edge-connected, corner-connected or not connected with neighbor voxel. Figure 2.20 gives a simple illustration of how the algorithm works. The connected voxels are labeled with the same cluster index.

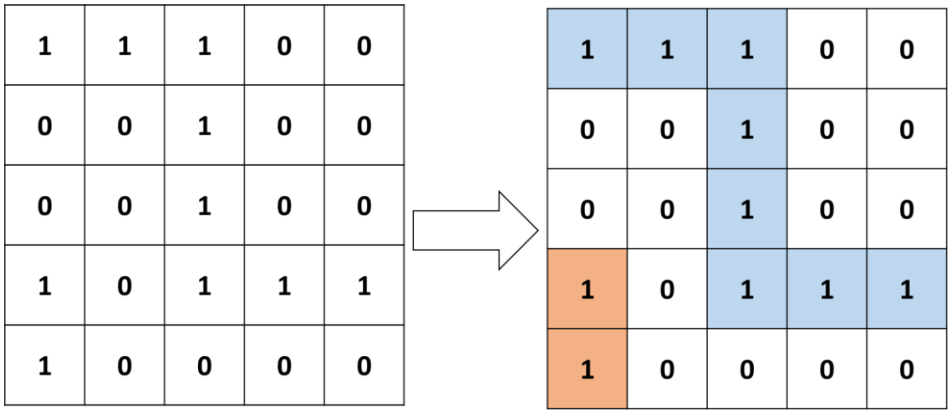

Figure 2.20 Illustration of pore cluster labeling by Hoshen-Kopelman's algorithm

This algorithm is easy to demonstrate with 2D binary images (Figure 2.21). The original input image is the word "PETE" colored white on a black background, the letters "ETE" are connected objects. By performing connected component labeling, the connected objects are identified and highlighted in different colors. The letter "P" is identified as one cluster (green), and letters "ETE" are identified as another cluster (blue).

Figure 2.21 The identified connected pixels from binary image: Original image on the top and identified connected objects colored on the bottom

The identified connected pore cluster number is plotted against permeability (Figure 2.22). The rock samples with smaller permeability have more pore clusters in unit volume, this is can be explained by the pore size distribution in Figure 2.10. Rock samples having more connected pore clusters have much smaller equivalent pore radius. Rock samples with higher equivalent pore radius have higher permeability although the number of the pore cluster is not as much as others, which can be observed by comparing Figure 2.23 and Figure 2.26.

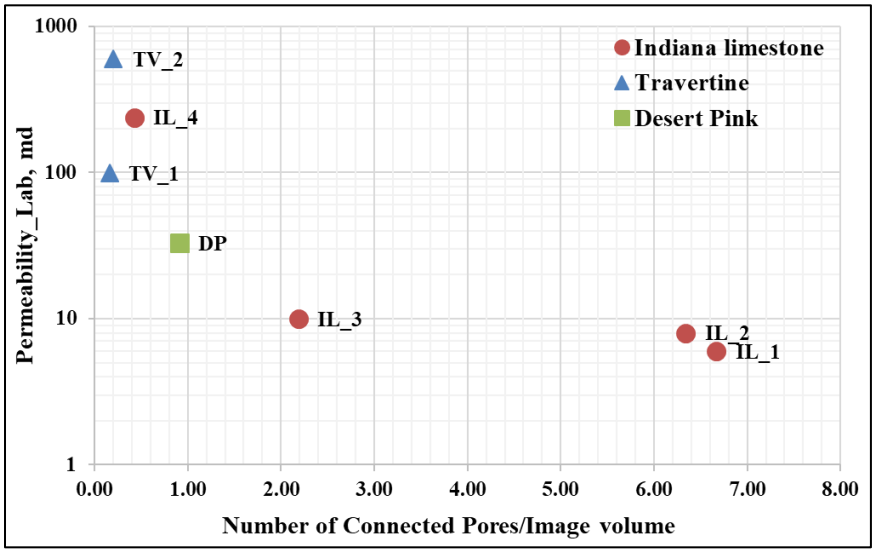

Figure 2.22 Plot of permeability against connected pore clusters in unit volume

Figures 2.23 to 2.26 are the extracted pore clusters using the Dristi software (Limaye 2012) for 600 mD Travertine, 239 mD Indiana limestone, 33 mD Desert Pink and 10 mD Indiana limestone, respectively.

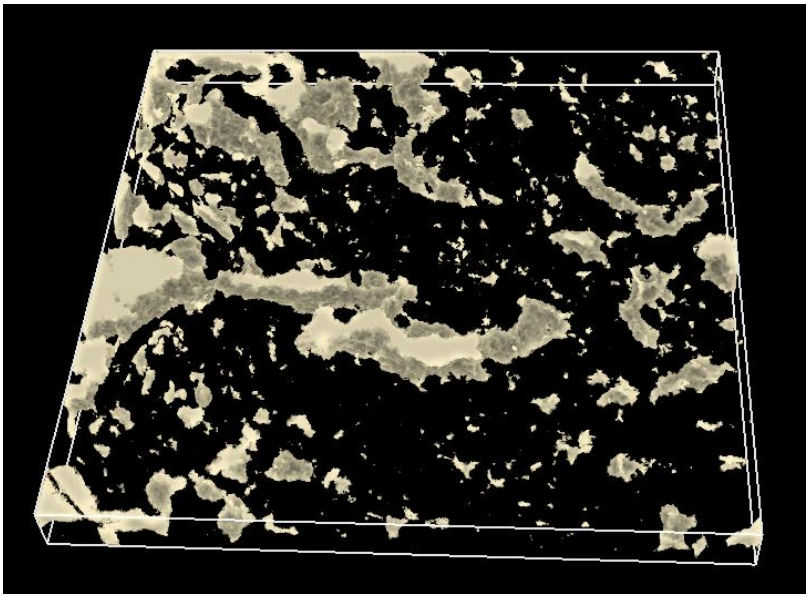

Figure 2. 23 Extracted pore structure for 600 mD Travertine (pore space in yellow white)

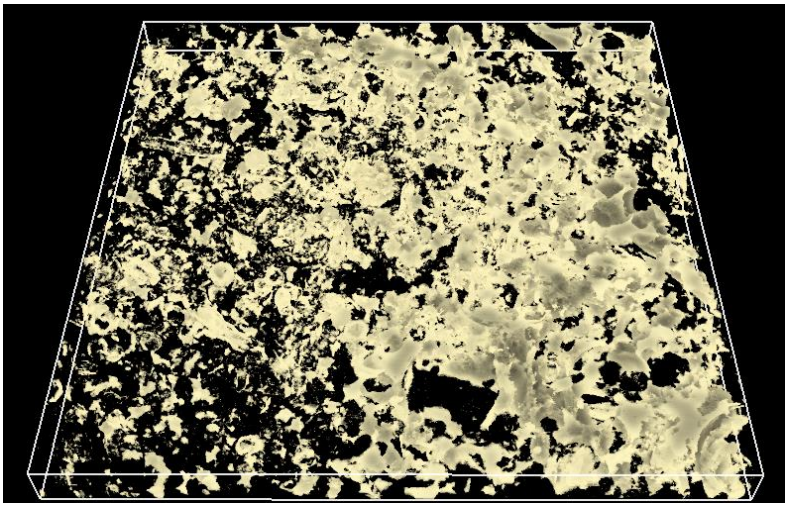

Figure 2. 24 Extracted pore structure for 239 mD Indiana limestone (pore space in yellow white)

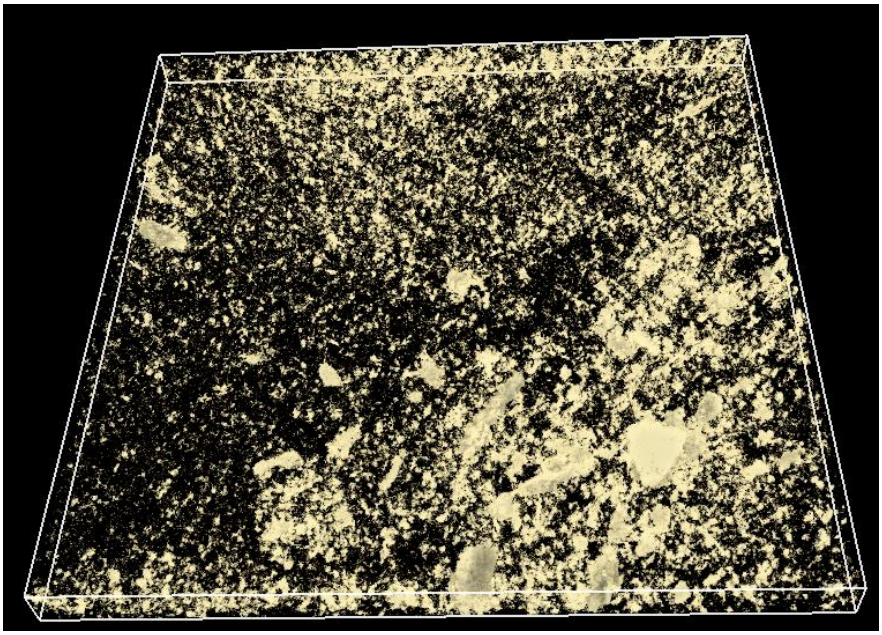

Figure 2. 25 Extracted pore structure for 33 mD Desert Pink rock (pore space in yellow white)

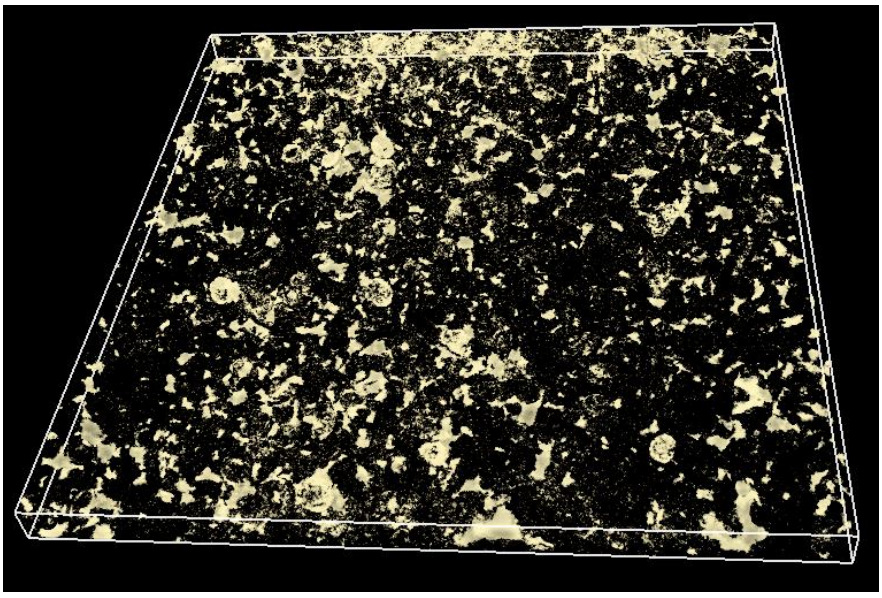

Figure 2. 26 Extracted pore structure for 10 mD Indiana limestone (pore space in yellow white)

2.5 Characterization of Surface-Area-to-Volume Ratio

The surface-area-to-volume ratio is defined as the total surface area in a unit volume of a material. We firstly identify the connected pore clusters by labeling, then we measure the surface areas for each pore clusters from surface mesh in pixels to obtain the total surface area inside the rock sample. Figure 2.27a gives the 3D structure of Indiana Limestone samples generated with processed 2D micro-CT scanned images, with the white color being the pore system and the black part being the rock matrix. We observe the intragranular and intergranular pores in this skeletal limestone sample. Figure 2.27b is the thin section image of the Indiana Limestone sample (Dong 2015) where the pore space is colored blue.

The image processing preserves the characteristics of the rock sample and reveals more details with higher resolution. Finally, we calculate the surface-area-to-volume ratio by dividing the total surface area by the bulk volume of the image stack. We performed the measurements by using a plugin called BoneJ (Doube M et al. 2010) developed for Fiji software.

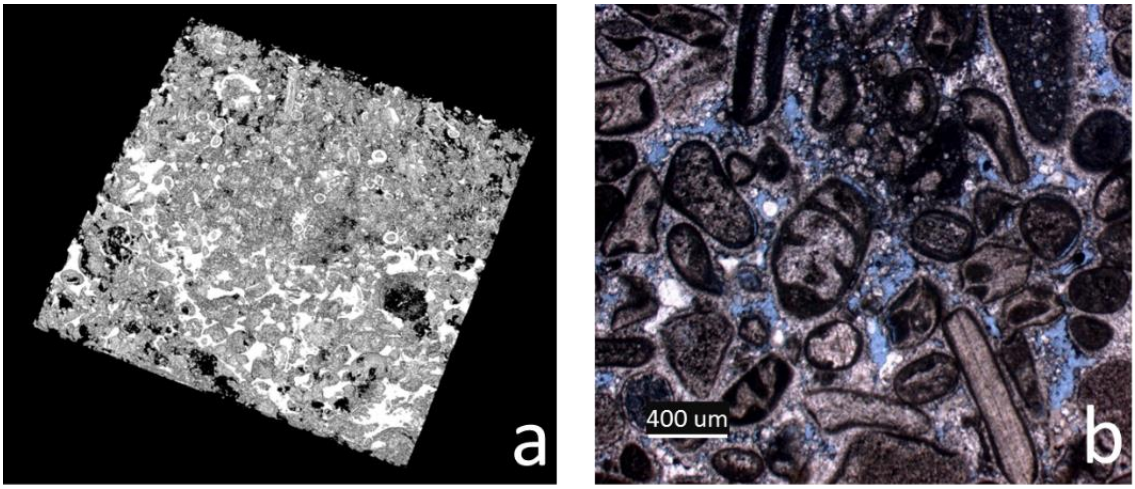

Figure 2.27 The extracted pore system of Indiana limestone with pores colored white on the left; thin section of Indiana limestone sample with 239 md permeability on the right

Figure 2.28 plots specific surface-area-to-volume ratio against laboratory-measured permeability. Smaller surface-area-to-volume ratios lead to higher permeability. This is a qualitative description of the relationship between surface-area-to-volume ratio with permeability.

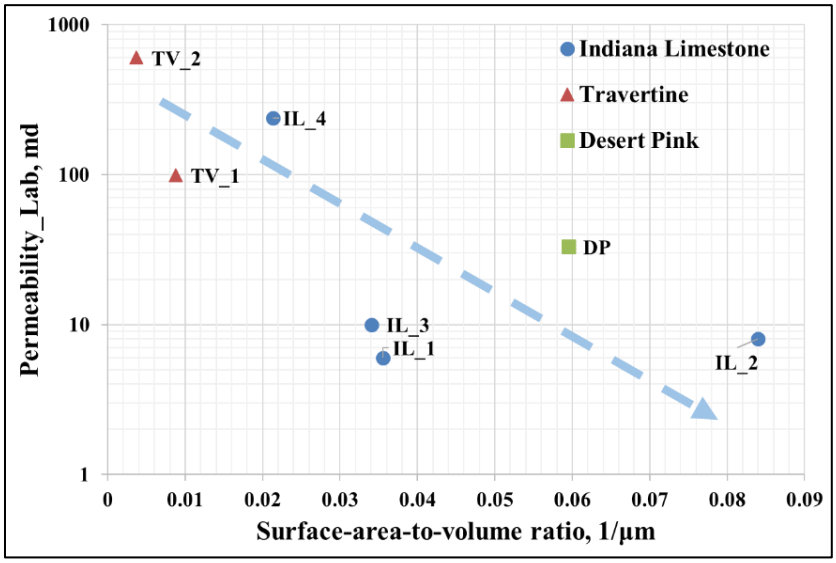

Figure 2.28 The plot of the surface-area-to-volume ratio against measured permeability

The plotted relationship between the specific surface-area-to-volume ratio and equivalent pore radius (Figure 2.29) indicates that as equivalent pore radius increases, the specific surface-area-to-volume ratio decreases. The negative relationship between the specific surface-area-to-volume ratio and equivalent pore radius can be explained by the simplified capillary tube model (Figure 2.30).

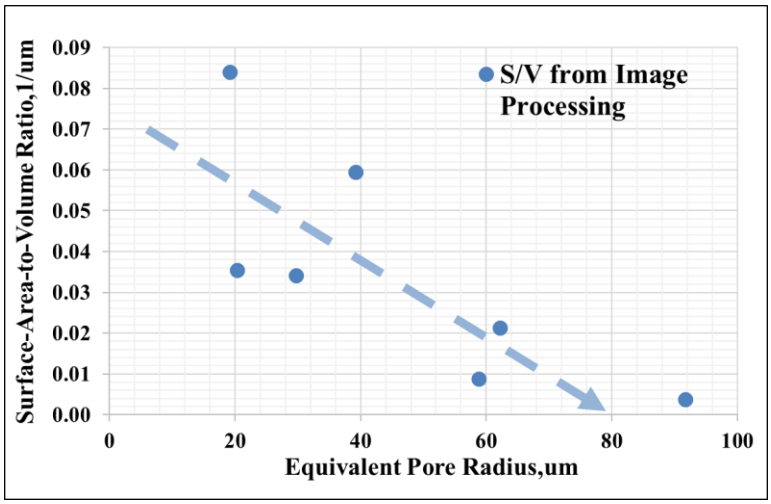

Figure 2.29 The plot of the specific surface-area-to-volume ratio against equivalent pore radius

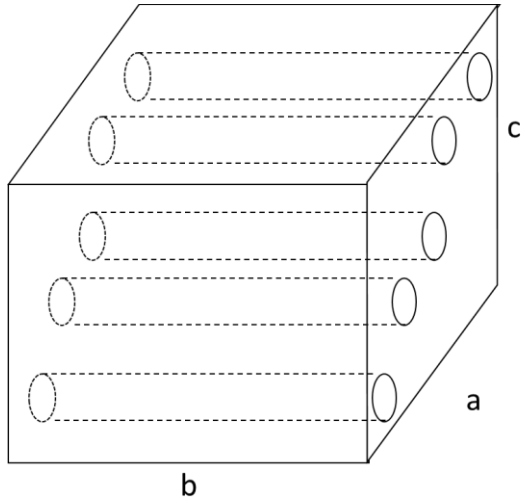

Figure 2. 30 An illustration of capillary tube model

The width, length, and height of the box-shaped volume are *a*, *b*, and *c*, respectively. Each of the capillary tube has the same radius *R* and same length b, the tortuosity is assumed as 1. The length of each capillary tube is the same as the length of the bulk volume. The number of the capillary tubes is *N*.

The bulk volume is given by:

$$V_c = a \cdot b \cdot c \tag{2.9}$$

The total surface area of the capillary tubes is:

$$S_c = N \times 2\pi Rb \tag{2.10}$$

The porosity ϕ is calculated as:

$$\phi = \frac{N\pi R^2 b}{abc} \tag{2.11}$$

The specific surface-area-to-volume ratio is given by:

$$\frac{S_c}{V_c} = \frac{2\pi RbN}{abc} = \frac{2\pi RN}{ac} \tag{2.12}$$

The number of capillary tubes N is calculated from Equation 2.11:

$$N = \frac{\phi ac}{\pi R^2} \tag{2.13}$$

Combine Equation 2.12 and Equation 2.13, we have:

$$\frac{S_c}{V_c} = \frac{2\pi R}{ac} \times N = \frac{2\pi R}{ac} \times \frac{\phi ac}{\pi R^2} = \frac{2\phi}{R} \tag{2.14}$$

Based on Equation 2.14, we can see that the surface-area-to-volume ratio is negatively related to the equivalent pore radius. Using the calculated equivalent pore radius and the measured porosity, the surface-area-to-volume ratio can be calculated by the simplified capillary tube model. Surface-area-to-volume ratio calculated from image processing is negatively related to the equivalent pore radius (Figure 2.29), which is the same for that calculated from capillary tube model. By plotting the reciprocal of equivalent pore radius R_e against the surface-area-to-volume ratio S/V in Figure 2.31, it is observed that the slope of the trend calculated from image processing is steeper than that calculated from the capillary tube model, which is 2ϕ.

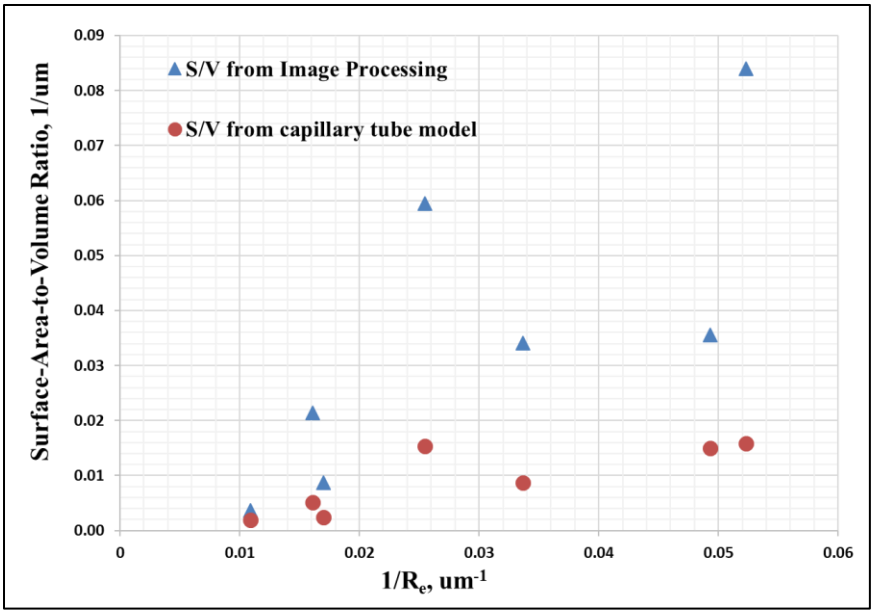

Figure 2. 31 The reciprocal of equivalent pore radius against the surface-area-to-volume ratio calculated by image process and simplified capillary tube model (red dots)

Taking the tortuosity parameter τ into the capillary tube model:

$$\tau = L_c / b \tag{2.15}$$

where L_c is the actual pore length, b is the length of the bulk volume. The illustration for this model is given by Figure 2.32.

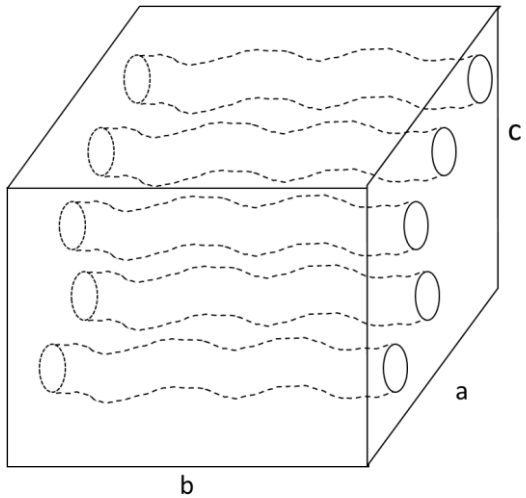

Figure 2.32 The capillary tube model with tortuosity

The surface area of the pore space in this capillary tube model becomes:

$$S_c = N \times 2\pi Rb\tau \tag{2.16}$$

The surface-area-to-volume ratio with tortuosity is given by:

$$\frac{S_c}{V_c} = \frac{2\pi R\tau}{ac} \times N = \frac{2\pi R\tau}{ac} \times \frac{\phi ac}{\pi R^2 \tau} = \frac{2\phi}{R} \tag{2.17}$$

Comparing Equation 2.14 and Equation 2.17, the surface-area-to-volume ratio does not change with tortuosity for the capillary tube model. Quantification of tortuosity for digital rock can be cost expensive using simulation techniques, such as Random Walk (Nakashima 2002). The relationship between porosity and tortuosity reported by previous researchers share the general forms of Equation 2.18 or Equation 2.19:

$$\tau = m_1 \phi^{n_1} \tag{2.18}$$

$$\tau = m_1 + n_1 \phi \tag{2.19}$$

where m_1 and n_1 are adjustable parameters that can be quantified with experiments. In this study the correlation derived by Berryman (1981) is applied for tortuosity calculation as Equation 2.20. The application and modification for Equation 2.20 for permeability estimation are discussed in detail in section 2.6.

$$\tau = (1 + \phi^{-1})/2 \tag{2.20}$$

The plot of the surface-area-to-volume ratio against the optimal pore volume to breakthrough is given in Figure 2.33, and the plot of the surface-area-to-volume ratios against the optimal interstitial velocity is given in Figure 2.34. It is observed that both the optimal pore volume to breakthrough and the optimal interstitial velocity are negatively related to the surface-area-to-volume ratio. However, the plot is scattered and should not be used for quantification.

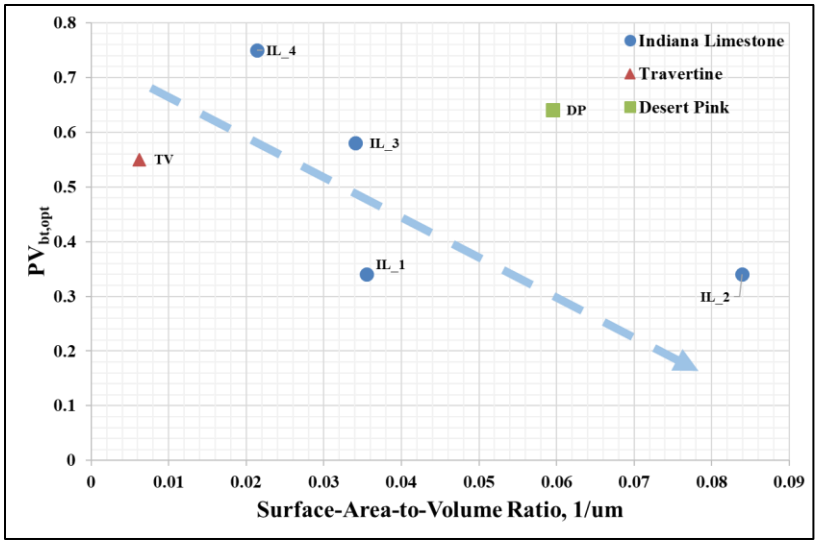

Figure 2.33 The surface-area-to-volume ratio against the optimal pore volume to breakthrough

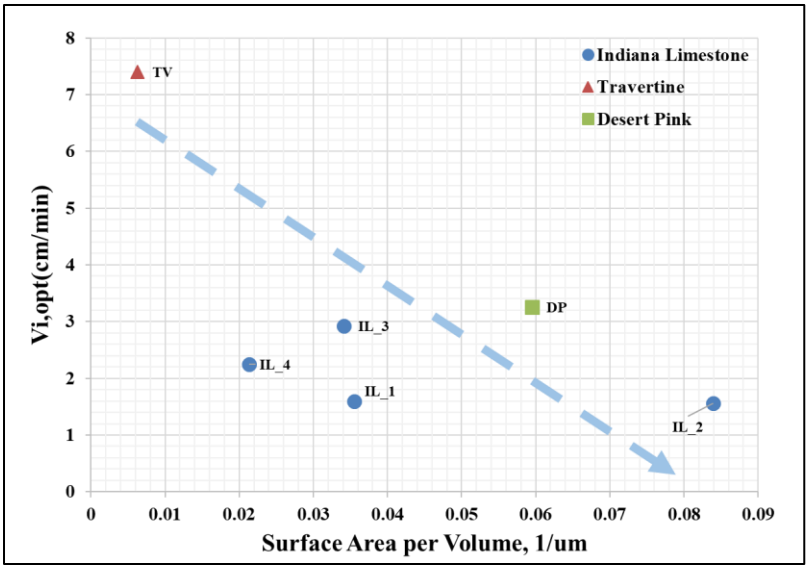

Figure 2.34 The plot of the surface-area-to-volume ratio against the optimal interstitial velocity

Following Equation 2.17, the relationship between the ratio of porosity and specific surface area $\phi/(S/V)$ against optimal pore volume to breakthrough is generated (Figure 2.35). Figure 2.35 is similar to Figure 2.13, which is the relationship between equivalent pore radius and optimal pore volume to breakthrough.

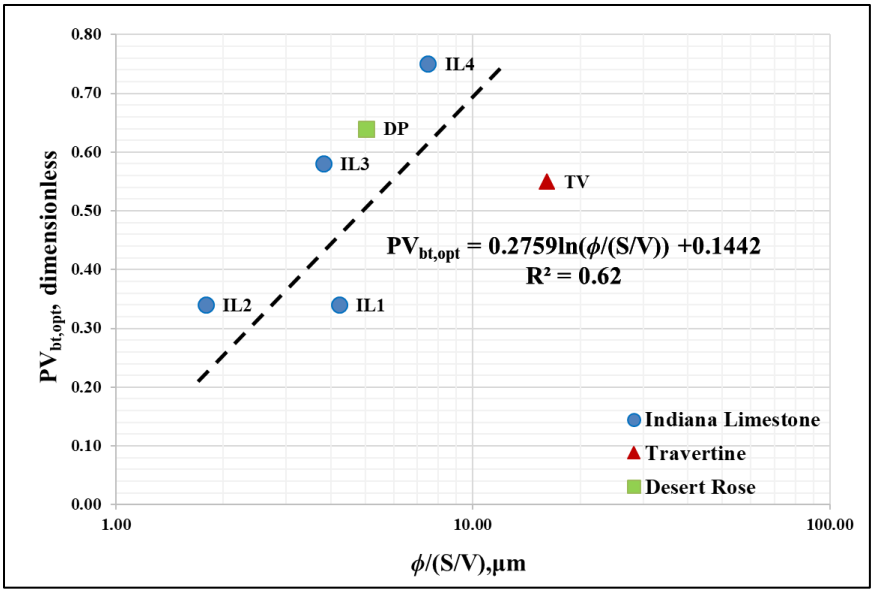

Figure 2.35 Relationship between ϕ/(S/V) against optimal pore volume to breakthrough

$\phi/(S/V)$ is a parameter similar to the equivalent pore radius (units of μm). The correlation between optimal pore volume to breakthrough and $\phi/(S/V)$ is given by Equation 2.21:

$$PV_{bt,opt} = 0.2759 \ln(\phi / (S/V)) + 0.1442 \tag{2.21}$$

The calculated properties based on binary image and laboratory measurements are listed in Table 2.5. Column 3 to column 6 are the calculated equivalent pore radius, mode pore radius, arithmetic average radius and standard deviation for all pores, respectively; Column 7 is the connectivity number in unit volume; Column 8 is the surface-area-to-volume ratio; Column 9 is the arithmetic average pore radius of top 5% large pores; Column 10 is the optimal pore volume to breakthrough; Column 11 is the optimal interstitial velocity.

Table 2.5 Properties calculated based on binary image and laboratory measurements

Sample Name	Por_Lab, v/v	Perm_ Lab, md	Equivalent Pore Radius,um	Mean Pore Radius, um	STD Pore Radius,um	Connectivity Number/Unit Volume	Surface-Area-to-Volume Ratio, 1/um	PVbt,opt	Vi,opt (cm/min)
Indiana Limestone_1	0.15	6	20	13.52	15.16	3.89	0.036	0.34	1.60
Indiana Limestone_2	0.15	8	19	13.44	13.60	2.58	0.084	0.34	1.56
Indiana Limestone_3	0.13	10	30	23.51	18.21	0.58	0.034	0.58	2.92
Indiana Limestone_4	0.16	239	62	35.72	50.86	-0.27	0.021	0.75	2.25
Travertine_1	0.07	99	59	40.35	42.70	-0.02	0.009	0.55	7.40
Travertine_2	0.09	600	92	37.97	83.55	0.18	0.004		
Desert Pink	0.30	33	39	25.77	29.55	-1.53	0.060	0.64	3.25

2.6 Characterization of Permeability

In this section the relationship between permeability and pore structure-related parameters are investigated with capillary tube model and empirical correlations based on Kozeny–Carman equation.

Darcy's law is given by:

$$Q = -k\frac{A}{\mu}\cdot\frac{dp}{dx} \tag{2.22}$$

where Q is the flow rate through the porous media (cm^3/s); A is the cross-section area fluid flowing through (cm^2); μ is the viscosity of the fluid (cP); dP/dx is the hydraulic pressure gradient between the inlet and outlet of the sample (atm/cm).

Assuming the flow in capillary tube is laminar, the capillary tube model is as shown in Figure 2.36. The length of tube is L, the radius of pore is R. The pressure at the inlet and outlet of the tube is p_1 and p_2, respectively.

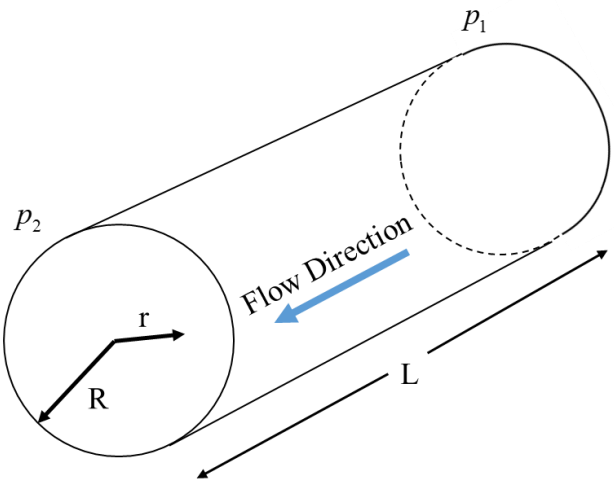

Figure 2.36 The illustration of fluid flow in one capillary tube

Assuming the fluid flow is balanced by the viscous force and the pressure between inlet and outlet, we have

$$\left(p_1 - p_2\right)\pi r^2 - \tau_s 2\pi rL = 0 \tag{2.23}$$

where r is the radius in radial direction, τ_s is the shear stress of the fluid.

Equation 2.23 can be rewritten as:

$$\tau_s = \frac{\Delta p \cdot r}{2L} \tag{2.24}$$

where Δp is the pressure difference:

$$\Delta p = p_1 - p_2 \tag{2.25}$$

For laminar flow of a Newtonian fluid, the shear stress is proportional to fluid velocity gradient:

$$\tau_s = -\mu \frac{du}{dr} \tag{2.26}$$

where u is the fluid velocity.

Combining Equations 2.24 and 2.26, we have:

$$-\frac{du}{dr}=\frac{\Delta p\cdot r}{2\mu L} \tag{2.27}$$

Integrating Equation 2.27 gives the following equations,

$$-\int du=\int\frac{\Delta p\cdot r}{2\mu L}dr=\frac{\Delta p}{2\mu L}\int rdr \tag{2.28}$$

$$-u(r)=\frac{\Delta p}{2\mu L}\frac{r^2}{2}+C \tag{2.29}$$

where C is a constant from integration.

Equation 2.29 is the general expression for fluid velocity. For laminar Newtonian fluid, the fluid velocity profile is illustrated in Figure 2.37.

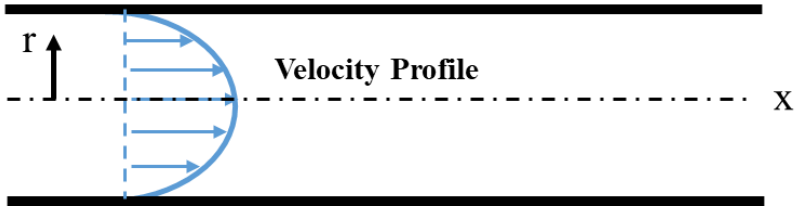

Figure 2.37 Fluid velocity profile in a capillary tube

The velocity at the wall of the capillary tube is 0:

$$-u(r=R)=\frac{\Delta p}{2\mu L}\frac{R^2}{2}+C=0 \tag{2.30}$$

$$C=-\frac{\Delta p}{2\mu L}\frac{R^2}{2} \tag{2.31}$$

The fluid velocity equation 2.29 becomes:

$$u(r)=-\frac{\Delta p}{2\mu L}\frac{r^2}{2}+\frac{\Delta p}{2\mu L}\frac{R^2}{2}=\frac{\Delta p}{4\mu L}(R^2-r^2) \tag{2.32}$$

The fluid flow in each circular lamina is given by:

$$q(r)dr = \frac{\Delta p}{4\mu L}(R^2 - r^2)2\pi r dr = \frac{\pi}{2\mu}\frac{\Delta p}{L}(rR^2 - r^3)dr \tag{2.33}$$

Integrating the total flux in the capillary tube from $r = 0$ to $r = R$:

$$q = \frac{\pi}{2\mu}\frac{\Delta p}{L}\int_0^R (rR^2 - r^3)dr = \frac{\pi R^4}{8\mu}\frac{\Delta p}{L} \tag{2.34}$$

where q is the flow rate in single capillary tube, R is the radius of the capillary tube, μ is the viscosity, Δp is the pressure along the tube and L is the actual length of the tube in Figure 2.33.

The derived Equation 2.34 is the famous Hagen–Poiseuille's equation for laminar flow in a circular capillary tube. Taking the tortuosity τ into consideration as Equation 2.15, the total flux in N capillary tube is:

$$Q = Nq = N\frac{\pi R^4}{8\mu}\frac{\Delta p}{b\tau} \tag{2.35}$$

Equation 2.11 can be written as:

$$\phi = \frac{N\pi R^2 b\tau}{abc} = N \cdot \frac{\pi R^2 \tau}{ac} \tag{2.36}$$

$$N = \frac{\phi ac}{\pi R^2 \tau} \tag{2.37}$$

Integrating Equation 2.37 and Equation 2.35, we have

$$Q = \frac{\phi R^2 ac\Delta p}{8\mu\tau^2 b} = \frac{\phi R^2 A\Delta p}{8\mu\tau^2 b} \tag{2.38}$$

where A is the cross section of the block in Figure 2.32 and $A = ac$;

Comparing Equation 2.38 against Darcy's law Equation 2.22, we have:

$$k = \phi\frac{R^2}{8\tau^2} \tag{2.39}$$

Integrating the specific surface ratio Equation 2.17 into Equation 2.39, we have the Kozeny-Carman equation (Kozeny, 1927, Carman 1937, 1956) as:

$$k = \phi \frac{R^2}{8\tau^2} = \frac{\phi^3}{2(S/V)^2 \tau^2} \tag{2.40}$$

where ϕ is porosity, *S/V* is the quantified specific surface area through image processing, and τ is the tortuosity estimated by using empirical correlation such as Equation 2.17.

The estimated permeability by using Kozeny-Carman equation is given in Figure 2.38 and Table 2.6. The Kozeny-Carman equation highly overestimates the permeability for high porosity, low permeability rocks (e.g. 6 mD Indiana limestone with 15% porosity, and 33 mD Desert Pink rock with 30% porosity). Kozeny-Carman equation may also underestimate the permeability for low porosity, high permeability rock (e.g. 99 mD Travertine sample with 7% porosity). In summary, the laboratory-measured permeability is tightly correlated to equivalent pore radius (as discussed in Section 2.3) but the Kozeny-Carman equation is not suitable for permeability estimation in this case. It should be modified and used with care for permeability estimation with digital data.

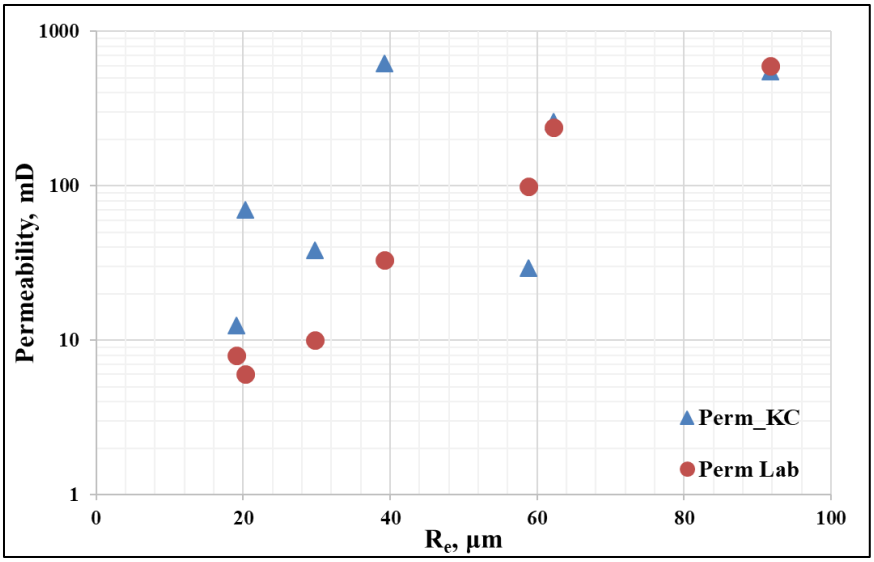

Figure 2.38 Estimated permeability by using Kozeny-Carman equation

Table 2.6 Parameters for permeability estimation with Kozeny-Carman's equation

Sample #	Sample Name	Por_Lab, v/v	Permeability_Lab, md	Equivalent Pore Radius,um	Surface-Area-to-Volume Ratio, 1/um	Tortuosity	Perm KC,md
1	Indiana Limestone_1	0.15	6	20	0.04	5.75	70
2	Indiana Limestone_2	0.15	8	19	0.08	5.75	12
3	Indiana Limestone_3	0.13	10	30	0.03	6.83	38
4	Indiana Limestone_4	0.16	239	62	0.02	5.32	261
5	Travertine_1	0.07	99	59	0.01	14.35	29
6	Travertine_2	0.09	600	92	0.00	10.61	552
7	Desert Pink	0.30	33	39	0.06	2.50	620

Researchers also discovered models for permeability estimation with general form of Equation 2.41 work well with a variety of rock types, including Fontainebleau sandstone, Berea sandstone or Indiana limestone (Nishiyama et al., 2017).

$$k = c_2 \phi^{a_2} R^{b_2} \tag{2.41}$$

where a_2 , b_2 and c_2 are adjustable parameters.

Based on the measured permeability, porosity, and calculated equivalent pore radius in section 2.3, the adjustable parameters a_2 ,b_2 , and c_2 are obtained by fitting Equation 2.41 with the laboratory-measured permeability. The fitted form of permeability estimation model is:

$$k = 0.00023\phi^{0.76} R_e^{3.67} \tag{2.42}$$

where k is permeability in mD, R_e is the equivalent pore radius in μm.

The estimated permeability with Equation 2.42 is plotted against the laboratory-measured permeabilities for our samples (Figure 2.39) and they indicate a strong relationship between estimated permeability and measured permeability.

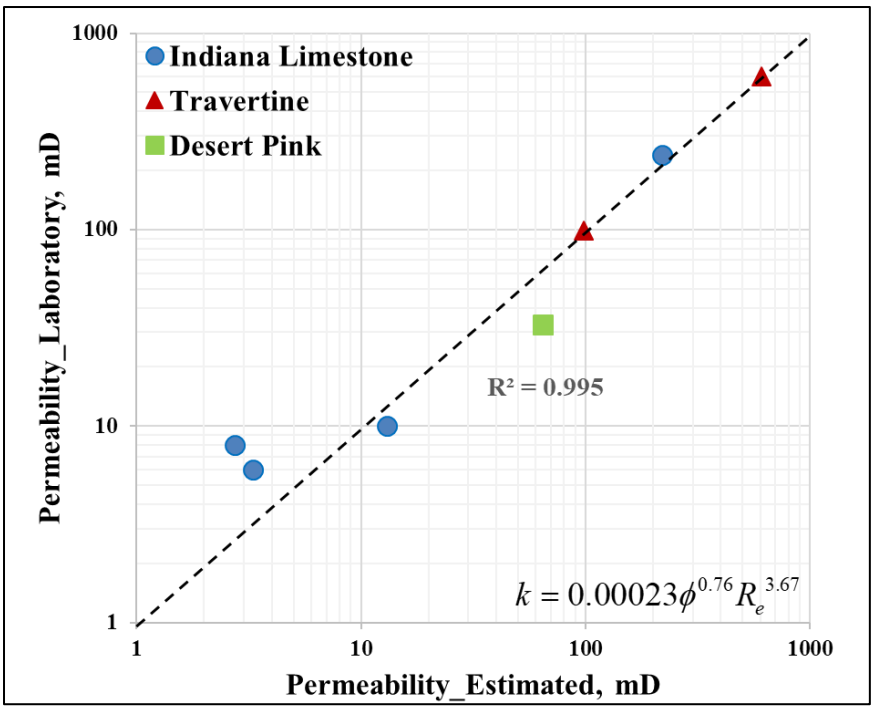

Figure 2.39 Estimated permeability against laboratory-measured permeability

The proposed permeability estimation model as Equation 2.5 and Equation 2.42 are both recommended for permeability estimation from digital rock for the tested rock samples. More

carbonate rock types need to be investigated for possible general correlation for carbonate permeability estimation. Permeability estimation using these empirical models should always be cross-validated by laboratory measurements.

2.7 Section Summary

In summary, we studied the micro-structures and important petrophysical parameters for Indiana Limestone, Desert Pink, and Travertine with micro-CT imaging technique. We defined the concept of equivalent pore radius with processed binary images, and we determined that laboratory-measured permeability from core plugs was strongly correlated to the equivalent pore radius calculated from micro-CT scanned images among the investigated carbonate rock samples. The semi-logarithmic correlation between permeability and effective pore radius fit the measured permeability data very well over a permeability range of more than two orders of magnitude. The findings of pore-scale pore structure and pore size distribution in this study are helpful for carbonate rock analysis, and a second permeability model is proposed based on measured porosity and equivalent pore radius. Two permeability models are both recommended for permeability estimation with digital rock data. The equivalent pore radius for Indiana limestone and Desert Pink samples is positively correlated with optimal pore volume to breakthrough whereas Travertine does not follow the same trend.

Additionally, we quantified the connectivity of the pore systems for tested rock samples with the concept of Euler-Poincare Characteristic number and calculated the surface-area-to-volume ratio. We observed that better connectivity, which has a smaller connectivity number, leads to higher permeability. Optimal pore volume to breakthrough increases as the connectivity increases. The relationship between connectivity number in unit volume and the optimal interstitial

velocity are not clear. The surface-area-to-volume ratio is negatively related to the permeability, optimal pore volume to breakthrough, and optimal interstitial velocity.

3. FORMATION CHARACTERIZATION AT CORE SCALE

3.1 Introduction

Core flooding with acid is a practical and reliable method to obtain optimal conditions, which is optimal pore volume to breakthrough and optimal interstitial flow rate. Normally Hydrochloric acid (HCl) is used for matrix acidizing since it is effective and economical, both for core flooding experiments in the laboratory or well stimulation in the field. When HCl acid is injected into limestone, a quick chemical reaction happens as:

$$CaCO_3 + 2HCl \rightarrow CaCl_2 + H_2O + CO_2 \tag{3.1}$$

where $CaCl_2$ is soluble in water and should not damage the formation.

In this study 15 wt% HCl is used for injection and the optimal conditions for Travertine are determined. Finally, all the optimal conditions for many rock types are collected and analyzed.

3.2 Travertine

3.2.1 Petrophysical Characteristics of Travertine

Travertine is formed rapidly during deposition of carbonate minerals, normally in springs or rivers. The mineralogy of our sample is mostly calcite and the color of the sample for this study is light yellow or cream-colored in Figure 3.1. Petrophysical properties of similar Travertine samples with different facies were previously determined (Paola 2013). The studied facies include crystalline crusts, shrubs, paper-thin rafts, and no porosity-permeability trend was observed for any facies in the selected samples (Paola 2013).

The Travertine sample studied here is highly anisotropic and heterogeneous with laminations and vugs observed on the rock surface. The Travertine block where the core plugs were cut is shown in Figure 3.1. The red colored laminations in Figure 3.1 were determined to be

impermeable layers during the core flooding experiment discussed in the next section. Plugs cut from vertical direction (Figure 3.2) has permeability value much lower than 1 mD so all core plugs for matrix acidizing were cut from the horizontal direction. The gravimetrically measured porosity of all Travertine samples is about 7.5% to 10%, the permeability measured ranges from lower than 1 mD to as high as 948 mD, depending on the orientation of core plug.

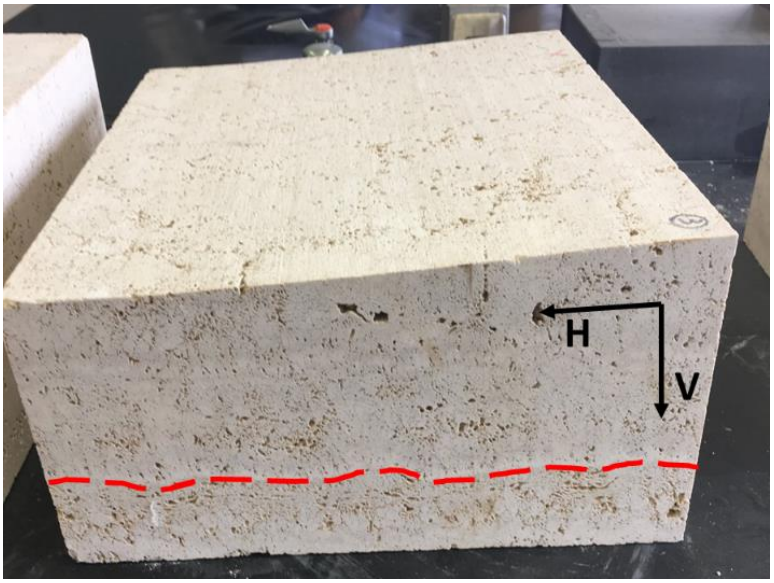

Figure 3.1 The Travertine block for this study (H indicates horizontal direction, V indicates vertical direction)

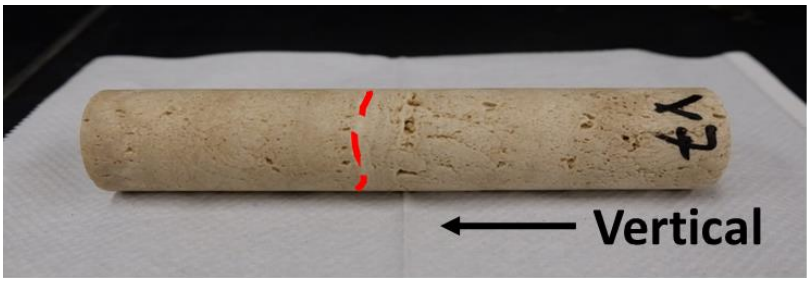

Figure 3.2 Travertine core plugs cut from vertical direction

Travertine is selected to measure the optimal conditions for matrix acidizing since it is analogous to Brazilian sub-salt units, where large hydrocarbon reserves were discovered and being producing in recent decades.

3.2.2 CT-Scan for Travertine

All core plugs were X-ray scanned with Computerized-Tomography scanner (CT scan) before the acidizing experiment to capture the inner pore structure. The CT scanner was made by Toshiba (Figure 3.3).

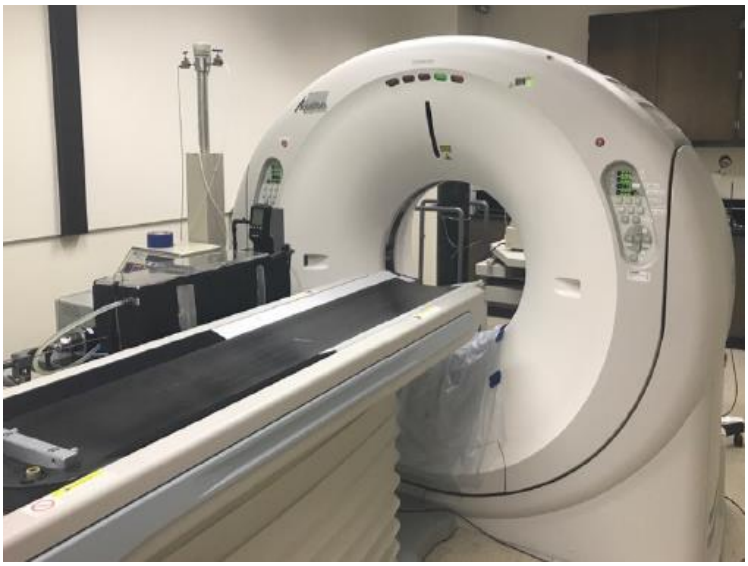

Figure 3.3 CT scanner used for Travertine scan

A CT scan is a tool to visualize the interior pore structure of a rock and investigate the heterogeneity of rock samples non-destructively. CT scanner has an X-ray source to generate and transmit X-rays through the scanned core plugs, and during the passing-through process, where X-ray are attenuated and detected by the electronic detector. The illustration of how CT works is given in Figure 3.4. Since X-ray attenuation is proportional to the object's density, we can obtain a two-dimensional image of density for the scanned core plugs. Since the cores are either dry with

air in the pores or are filled with water in the pores, the pore space has density difference between the matrix, which is 2.71 g/cc for calcite. Thus we can separate the rock matrix from the pore space through image processing. An open-source image viewer Horos (source: horosproject.org) is used to process the scanned CT image.

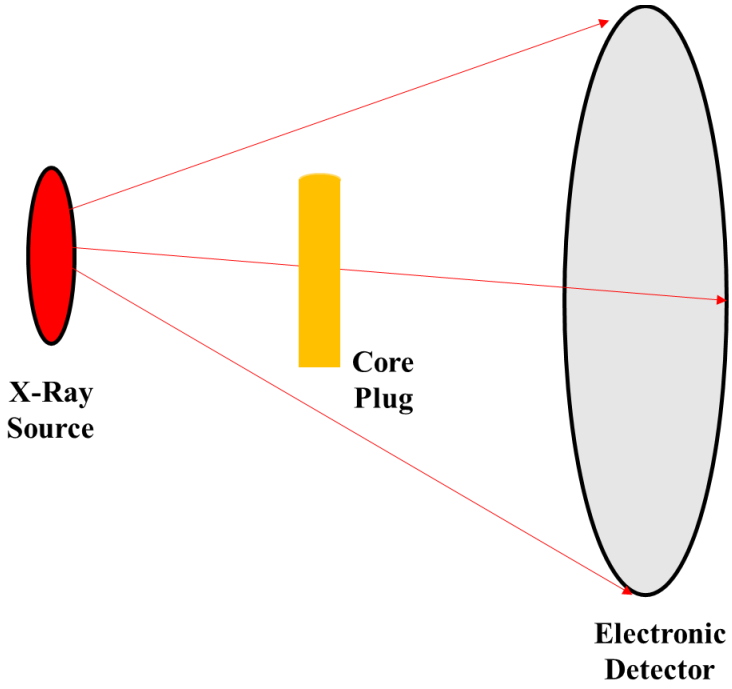

Figure 3.4 CT scan working principle illustration

The image processing procedure for CT images using Horos is similar to the procedure of processing micro-CT image with FIJI software, the steps include import of images, choosing the region of interest, segmentation by adjusting the cutoff in data histogram and generating the 3D image. The scanned and processed images for 3 Travertine plugs are shown in Figure 3.5. The darker areas circled in red are identified as impermeable zones where few pores are distributed, leading to low permeability and measurements that are below the limitation of laboratory equipment.

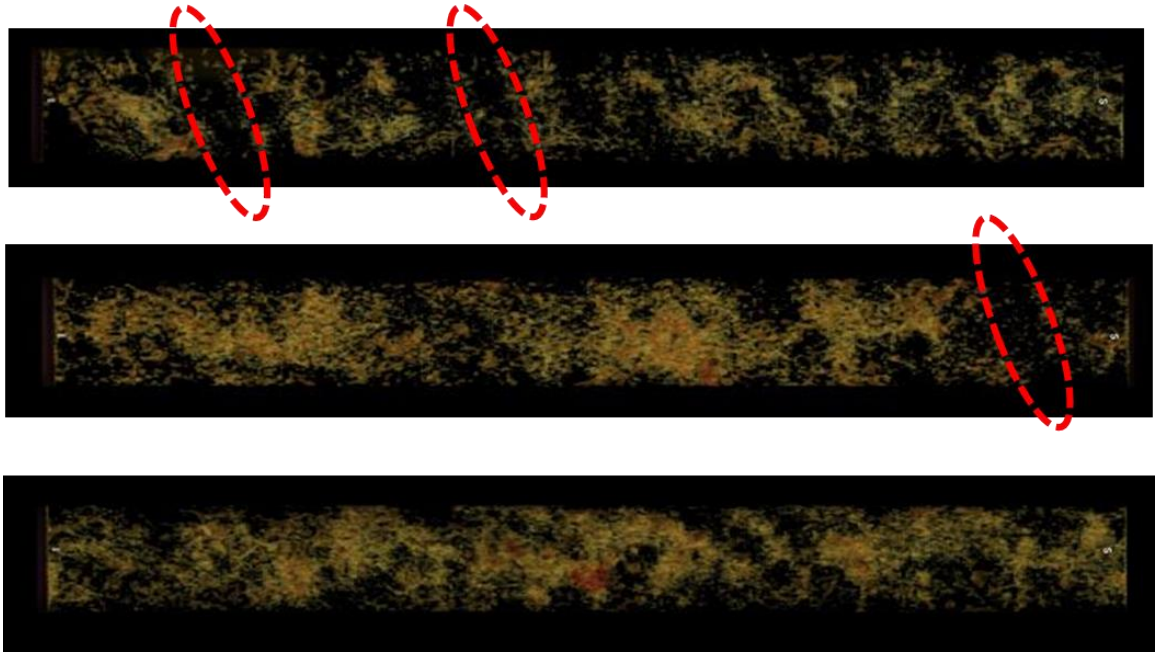

Figure 3.5 The CT scanned image for Travertine samples

3.3 Experiments for Matrix Acidizing

In this section the experimental setup and experiment procedures for matrix acidizing are introduced.

3.3.1 Experiment Apparatus

The experiment apparatus for matrix acidizing consists of syringe pumps, accumulators for brine and acid, pressure control system, core holder, heating tapes and data recording computer (Figure 3.6). The detailed setup procedure and experiment procedure is in Dong (2012).

The high-precision pumps use mineral oil to push piston to provide a fluid injection rate as low as 0.001 mL/min and it can be easily adjusted for a higher rate. The stainless steel accumulators can hold either brine or acid up to 1000 mL and the pressure limit is 5000 psi. The core holder (Figure 3. 7) can hold 1.5 inch diameter cores with lengths up to 20 inch, and it has

rubber sleeve between the core and core holder to take confining pressure, which is provided by a hand pump.

A back pressure regulator is used to ensure fluid flow occurs only when the pressure on the core outlet is equal or higher than the back pressure, which is normally set as 1000 psi supported by a nitrogen tank. The heating tape is electrically powered and can be wrapped around the core holder and fluid pipe to heat the injected fluid. A temperature sensor wire connects the core holder and data recording computer to control experiment temperature. During the experiment the pressure is recorded by pressure transducers and LabVIEW software.

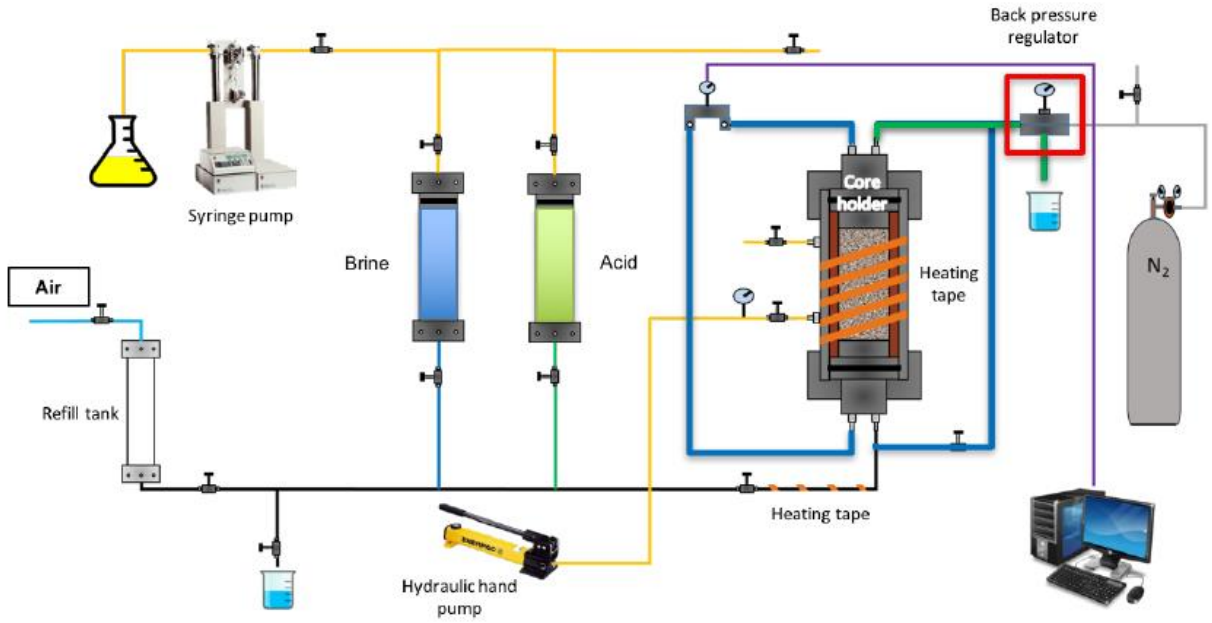

Figure 3.6 The experiment setup for matrix acidizing (Reprinted from Cheng 2017)

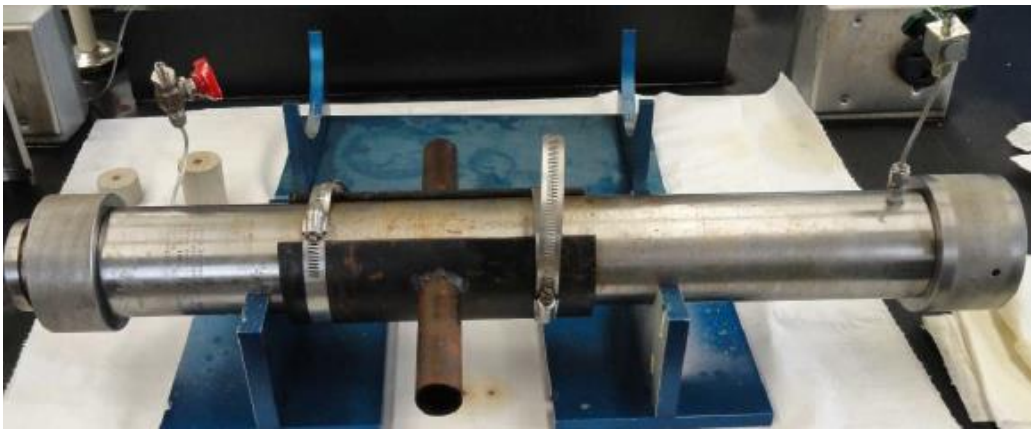

Figure 3.7 Core holder

3.3.2 Experimental Procedure

Core plugs with 1.5-in diameter by 8-in length are cut from a Travertine block shown in Figure 3.8. All cores are cut along the horizontal direction to avoid crossing the impermeable layer (white streak on the block). Core plugs were dried in a heated oven over 6 hours and weighted (Figure 3.9). After that, the core plugs are placed in a sealed container with a vacuum pump over 8 hours to guarantee the cores were fully saturated. The weight of the saturated cores is measured with a high-precision scale.

Figure 3.8 Travertine block where the cores are cut from

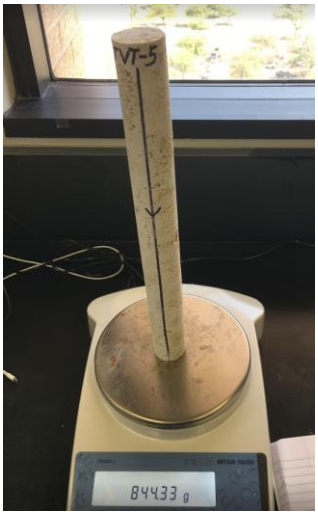

Figure 3.9 Measurement of the weight of dry Travertine core plug

The weight difference between the saturated core plug and dry plug is the weight of water occupying the pore space during the saturating procedure.

$$\Delta W = W_{core\_sat} - W_{core\_dry} \tag{3.1}$$

$$\Delta V = \frac{\Delta W}{\rho_w} \tag{3.2}$$

where W_{core_sat} is the weight of saturated core and W_{core_dry} is the weight of the dry core, ΔW is the weight difference; ρ_w is density of water, ΔV is the pore volume in the core plug.

The volume of the core plug was calculated by the diameter and length.

$$V_{core} = \frac{\pi d_{core}^2 L_{core}}{4} \tag{3.3}$$

where d_{core} is the diameter of the core plug and L_{core} is the length of the core plug, V_{core} is bulk volume of the core plug.

The total porosity ϕ of the core plug is finally given by:

$$\phi = \frac{\Delta V}{V_{core}} \tag{3.4}$$

The experiment initiated by assembling the saturated core into the core holder, and applying confining pressure to the core holder by using the manual hydraulic pump to avoid any fluid flow bypassing the core. The confining pressure was always set as 400 psi higher than the core inlet injection pressure. Then water was injected into the core until steady state was reached. The pressure difference between the core inlet and outlet were recorded during the water injection. The permeability was calculated by applying Darcy's law with the measured pressure drop. The heating tape was wrapped around the core holder and lines to heat the system until the desired temperature was reached (150 °F in this experiment). After that, the prepared 15 wt% of HCl mixed with a corrosion inhibitor was injected into the core until the pressure drop between the inlet of the core holder and outlet of the core holder became zero, indicating the wormhole penetrated through the core. The injection time and pressure were recorded during the acid injection for calculating pore volume to breakthrough. The experiment conditions are listed in Table 3.1, including experiment temperature, acid concentration, back pressure, and acid injection rate. The experiments were repeated for different core plugs cut from the same rock block with various injection rates to calculate optimal conditions.

Table 3.1 Acidizing experiment conditions for Travertine

Core#	Experiment Temperature, °F	HCl wt%	Back Pressure, psi	Injection rate(ml/min)
TVT4	150	15	1500	15.0
TVT8	150	15	1500	10.0
TVT9	150	15	1500	18.0
TVT11	150	15	1500	8.0
TVT5	150	15	1500	35.0
TVT10	150	15	1500	30.0
TVT2	150	15	1500	50.0
TVT_11	150	15	1500	6.5
TVT1C	150	15	1500	1.8

3.3.3 Experiment Results

Based on the recorded pressure data, acid injection time and acid injection rate, the experiment results are listed in Table 3.2, including the rock permeability, interstitial velocity, and pore volume to breakthrough. Core plugs with permeability lower than 1 mD were not used for matrix acidizing due to the impermeable layer or regions with few distributed pores. The Buijse-Glasbergen model (Buijse, Glasbergen 2005) was applied to the measured data to generate the wormhole-efficiency curve. This model is semi-empirical and the experimental data are fitted with least-square method.

Table 3.2 Matrix acidizing results for Travertine

Core#	Perm(mD)	Porosity, v/v	Injection rate(ml/min)	Vi(cm/min)	PVbt
TVT4	672	0.07	15.0	19.4	0.5
TVT8	174	0.06	10.0	13.6	0.7
TVT9	473	0.11	18.0	14.7	0.6
TVT11	62	0.06	8.0	11.9	1.1
TVT5	302	0.10	35.0	29.6	0.9
TVT10	63	0.11	30.0	24.3	0.6
TVT2	1194	0.12	50.0	44.3	1.1
TVT_11	542	0.09	6.5	7.0	1.0
TVT1C	100	0.06	1.8	3.0	1.7

The fitted wormhole-efficiency curve (Figure 3.10) indicates that the fitted optimal interstitial velocity was 7.4 cm/min, which is much higher than the other relative homogeneous rock types, such as Indiana limestone. This is related to the large pore radius (studies discussed in Chapter 2) and unique pore structure of Travertine.

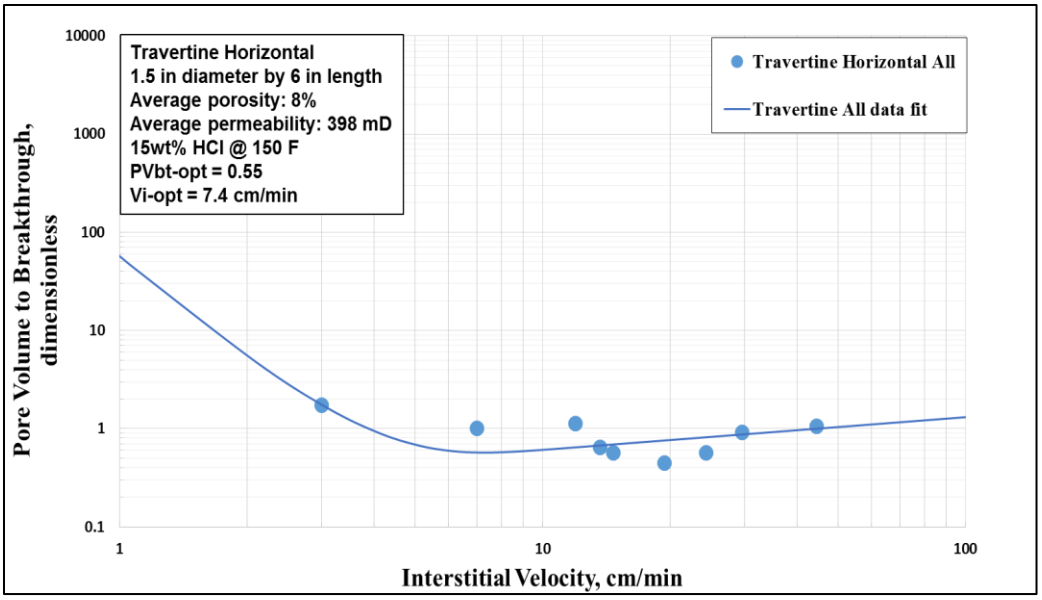

Figure 3.10 Wormhole efficiency curve for Travertine

3.4 Statistical Results for Optimal Conditions

3.4.1 General Wormhole-Efficiency Curve

Previous researchers conducted many core measurements for determining optimal conditions. In this study, we collected several acidizing experiment results and generated the wormhole-efficiency curve for each set of experiments. As listed in Table 3.2, the tested rocks are different rock types (Indiana limestone, Desert Pink, Kansas Chalk, Travertine, vuggy calcite, and Glen Rose rock), with differing porosity (8% to 35%), and differing permeability (1.86 mD to 398 mD); the core plug size for matrix acidizing ranges from 1 inch diameter, 1.5 inch diameter, and 4 inch diameter; the acid concentration for matrix acidizing are either 15 wt% or 28 wt%; the temperature for experiment ranges from room temperature to 200 °F. The influence of acid concentration, experiment temperature on optimal conditions is covered in section 1.2.

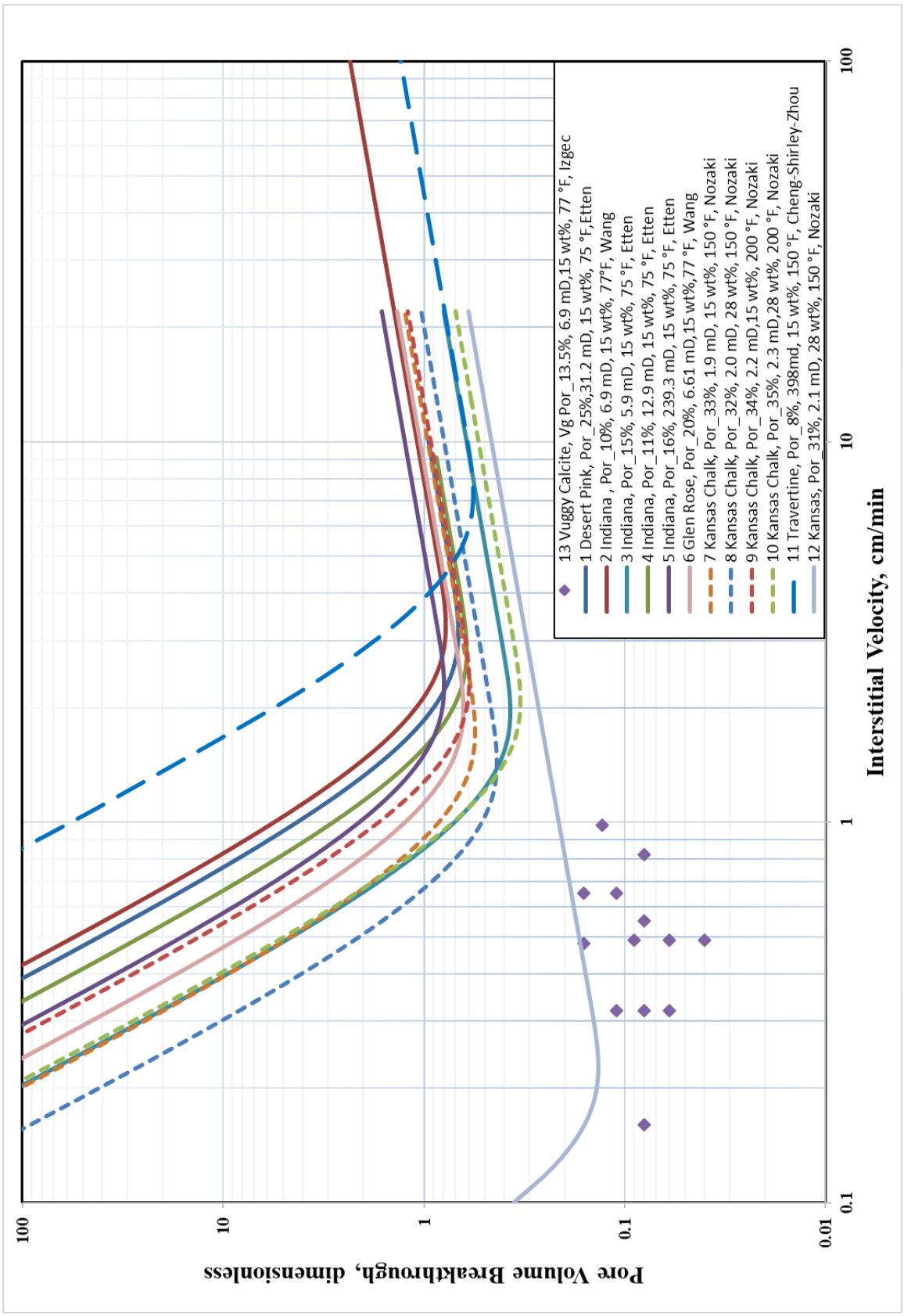

Figure 3.11 Statistics for wormhole-efficiency curves

Table 3.3 Statistics for matrix acidizing experiments

Curve #	Rock Type	Core Size(diameter by length), in × in	Porosity, v/v	Permeability, mD	Acid Type	Acid Concentration	Temperature, °F	Vi,opt, cm/min	PVbt,opt	Conducted by
1	Desert Pink	1.5×8	0.25	33.0	HCl	15 wt%	75	3.25	0.64	Etten
2	Indiana Limestone	1×6	0.1	6.9	HCl	15 wt%	77	3.34	0.75	Wang
3	Indiana Limestone	1.5×8	0.15	5.9	HCl	15 wt%	75	1.98	0.37	Etten
4	Indiana Limestone	1.5×8	0.11	12.9	HCl	15 wt%	75	2.91	0.58	Etten
5	Indiana Limestone	1.5×8	0.16	239.3	HCl	15 wt%	75	2.25	0.75	Etten
6	Glen Rose	1×6	0.20	6.6	HCl	15 wt%	77	2.02	0.61	Wang
7	Kansas Chalks	1×6	0.33	1.9	HCl	15 wt%	150	1.76	0.54	Nozaki
8	Kansas Chalks	1×6	0.32	2.0	HCl	28 wt%	150	1.46	0.42	Nozaki
9	Kansas Chalks	1×6	0.34	2.2	HCl	15 wt%	200	2.38	0.58	Nozaki
10	Kansas Chalks	1×6	0.35	2.3	HCl	28 wt%	200	2.12	0.32	Nozaki
11	Travertine	1.5×6	0.08	398.0	HCl	15 wt%	150	7.40	0.55	Cheng-Shirley-Zhou
12	Kansas Chalks	4×16.5	0.31	2.1	HCl	28 wt%	150	0.23	0.13	Nozaki
13	Vuggy Calcite	4×20	0.14	6.9	HCl	15 wt%	77	NA	NA	Izgec

The wormhole-efficiency curves (Figure 3.11) for each set of experiments was generated. It is observed that the optimal interstitial velocity for most rock types with 1 inch diameter or 1.5 inch diameter core plugs, except Travertine, lie in a narrow range of 1.46 cm/min to 3.34 cm/min, even though the acid concentration, experiment temperature and rock petrophysical properties are different for each set of experiment. The optimal pore volume to breakthrough for 1 inch or 1.5 inch diameter core plug ranges from 0.32 to 0.75.

The wormhole efficiency curve for Travertine (blue dash lines numbered 7 in Figure 3.11) is unique and the optimal interstitial velocity is 7.4 cm/min, which is much higher than other rock types. The optimal pore volume to breakthrough is 0.55, which is in the same range of other rocks.

Core dimension plays an important role for optimal conditions. The light purple curve #12 (Figure 3.11) is the wormhole-efficiency curve for 4 inch diameter Kansas Chalk, whose optimal interstitial velocity is 0.23 cm/min and the optimal pore volume to breakthrough is 0.13. This is in the same range for the 4-inch diameter vuggy calcite optimal conditions (purple points on the left corner of Figure 3.11). The optimal conditions for 4-inch diameter cores are much lower than the 1-inch or 1.5-inch cores, as both optimal interstitial velocity and optimal pore volume to breakthrough are affected by the core scale.

Figure 3.11 gives general guidance of the optimal interstitial velocity for matrix acidizing design and the heterogeneity of the pore structure for different rock type is playing an important role in determining optimal conditions. More tests on larger scale limestone blocks may indicate optimal conditions that are closer to the field application.

3.4.2 The Effect of Porosity and Permeability on Optimal Conditions

Based on the experimental data in Table 3.3, analysis of the effects of petrophysical properties on wormhole efficiency are conducted. The relationship between permeability and optimal pore volume to breakthrough is shown in Figure 3.12. The relationship between rock permeability and optimal pore volume to breakthrough is not obvious across various rock types. Kansas chalk (points colored purple) samples sharing similar permeability (around 2 mD) have distinct optimal pore volume to breakthrough ranging from 0.32 to 0.58. This also is observed in Indiana limestone: the 1.5-inch diameter core sample with 5.9 mD permeability has $PV_{bt,opt}$ of 0.37 but the 1-inch diameter sample with 6.9 mD permeability has much higher $PV_{bt,opt}$ of 0.75. Travertine has the largest permeability among all rock samples but the optimal pore volume to breakthrough is close to the average value of all rocks.

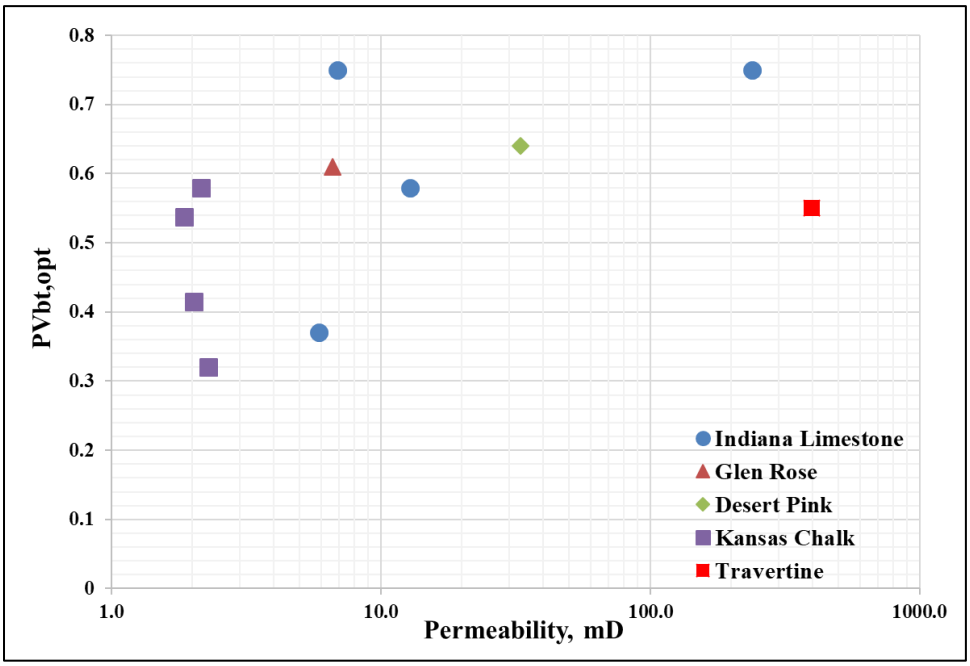

Figure 3.12 The plot of permeability against optimal pore volume to breakthrough

The relationship between core permeability and optimal interstitial velocity for various rock types is plotted in Figure 3.13. Optimal interstitial velocity is generally increasing as permeability increases. The correlation between permeability and optimal interstitial velocity is given as Equation 3.5, where the outlier data of high permeability Indiana limestone (239 mD) is excluded. This equation can be improved by incorporating more experiment data and may be used for acidizing treatment design.

$$V_{i,opt} = 0.95\ln(k) + 0.9 \tag{3.5}$$

where $V_{i,opt}$ is in cm/min, and k is in mD.

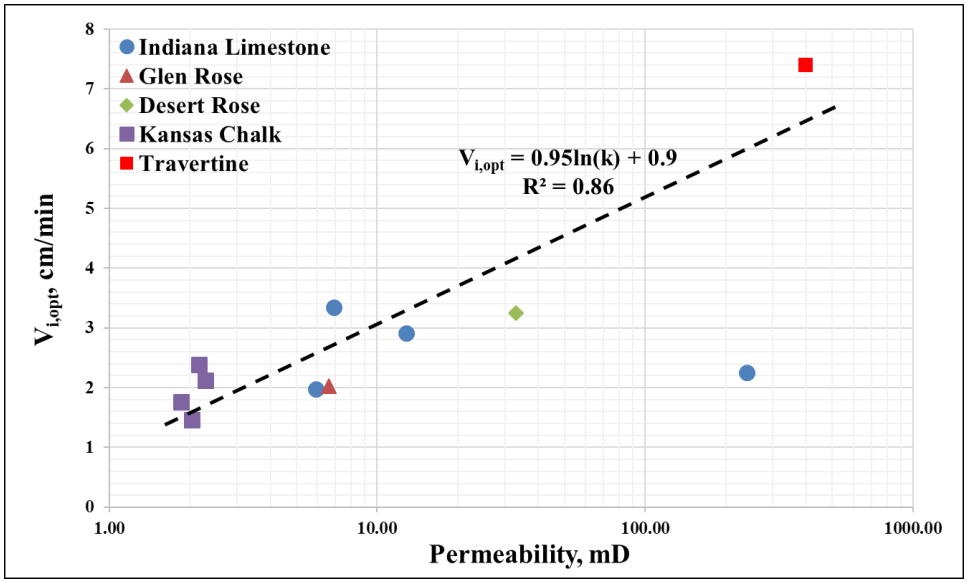

Figure 3.13 Relationship between core permeability and optimal interstitial velocity

The plot of porosity against optimal pore volume to breakthrough is shown in Figure 3.14, and the plot of porosity against optimal interstitial velocity is given by Figure 3.15.

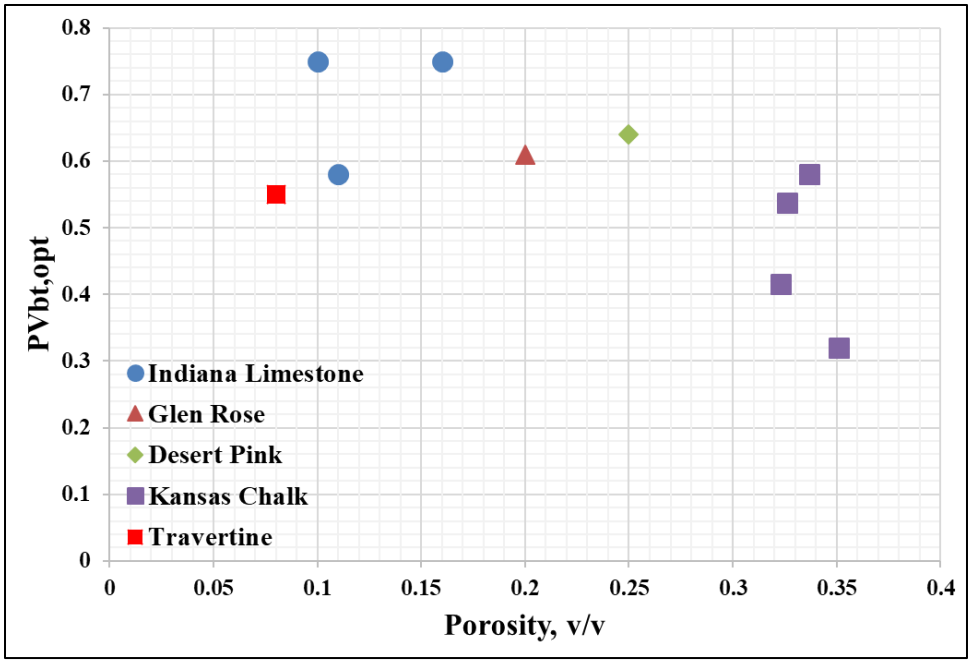

Figure 3.14 The plot of porosity against optimal pore volume to breakthrough

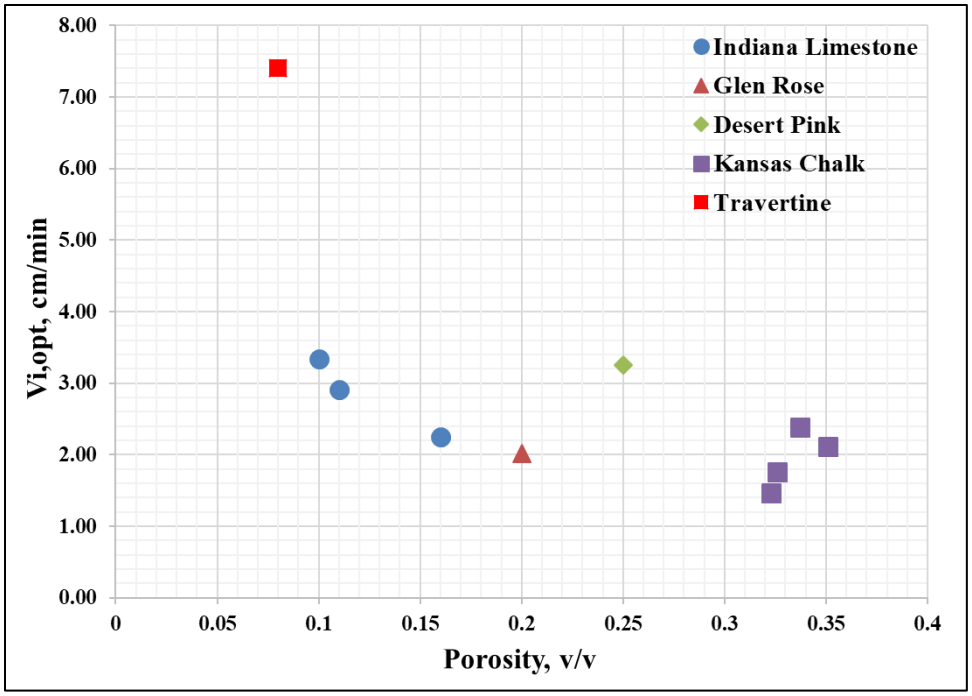

Figure 3.15 The plot of porosity against optimal interstitial velocity

The plot of porosity against optimal pore volume to breakthrough is scattered across all tested rock types and a negative trend is observed. The negative trend is caused by Kansas chalk, which is a high porosity (around 0.33 v/v) and low permeability (around 2 mD) limestone. The pores in Kansas chalk are poorly connected thus the permeability is lower than most other limestone units. The optimal pore volume to breakthrough of 1 inch or 1.5-inch diameter core plug for all rock types ranges from 0.32 to 0.75, and it is not sensitive to the change of porosity.

The plot of porosity against optimal interstitial velocity across all rock types has a more obvious negative trend but this curve should not come to a generalized conclusion. The Travertine (red point on the upper left of Figure 3.15) has high permeability for several hundred millidarcy but the porosity is only 0.08 v/v, which is opposite to that of Kansa chalk (purple points on the lower right of Figure 3.15). The optimal interstitial velocity for relative homogeneous rocks (Indiana limestone, Glen Rose, and Desert Pink) lie in a narrow range of 1.98 cm/min to 3.34 cm/min.

3.5 Section Summary

In this section, the methodology to determine optimal conditions for matrix acidizing by experiment was introduced and the optimal conditions for Travertine were obtained. Travertine is highly heterogeneous and anisotropic with vuggy pore structures, the optimal interstitial velocity is 7.4 cm/min, which is much higher than that of other tested rock types.

Additionally, the history experiment data for 13 sets of matrix acidizing experiments was collected and the wormhole-efficiency curve for each study was generated. The test rock types include Indiana limestone, Glen Rose, Desert Pink, Kansas chalk, vuggy calcite, and Travertine. The optimal interstitial velocity for most limestone tested except Travertine ranges from 1.46

cm/min to 3.34 cm/min even though the experiment temperature and acid concentration vary. The optimal pore volume to breakthrough ranges from 0.32 to 0.75 for all tested rock types. Core scale for matrix acidizing has great impact on optimal conditions: both pore volume to breakthrough and optimal interstitial velocity decrease as core diameter increases.

Finally, the effect of petrophysical properties on optimal conditions were analyzed by cross plotting their relationships. Based on the generated curves, we observe that permeability is positively related to optimal interstitial velocity. The impact of permeability on optimal pore volume to breakthrough for general rock types is not definitely clear. The impact of porosity on optimal conditions for general rock types is not clearly observed.

4. FORMATION CHARACTERIZATION AT LOG SCALE

4.1 Introduction

In a matrix acidizing treatment, acid is injected into carbonate units, where the acid reacts with carbonate rock and dissolves a portion of the rock. The dissolution creates some branch-shaped structures (Figure 4.1) that are highly conductive for flow, and are referred to as wormholes. Figure 4.1 is a CT scanned image of wormholes generated with 15 wt% HCl injection at optimal injection rate (McDuff et al. 2010). As mentioned before, there is an optimal injection rate, where wormholes can penetrate into the formation furthest at a given total injection volume. The optimal injection rate is important for the success of matrix acidizing treatment.

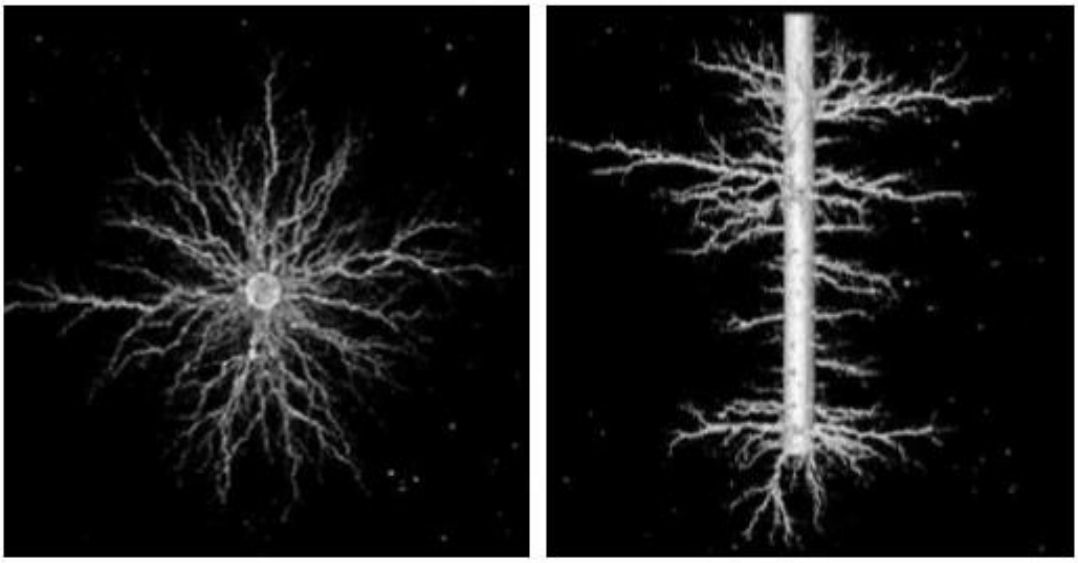

Figure 4.1 CT scanned image of wormholes generated with 15 wt% HCl injection at optimal injection rate (Reprinted from McDuff et al. 2010)

In field application, acid is injected into a carbonate formation with various well completion schematics, including bullheading, coiled tubing, acid jetting, limited entry, etc. The injection method should be selected according to the completion type and reservoir properties.

Figure 4.2 is an illustration of wormholes being created after acid was injected into formation through horizontal well. As the wormhole grows deeper into the formation, the damaged zone is bypassed and the wellbore is better connected to the undamaged formation with higher permeability.

Because permeability plays an important role in wormhole development and acid treatment design in this chapter, we first review and discuss the wormhole models, the well performance model, and the matrix acidizing design model for horizontal wells. We then discuss how to estimate permeability at the field scale by using well logs to conduct treatment design.

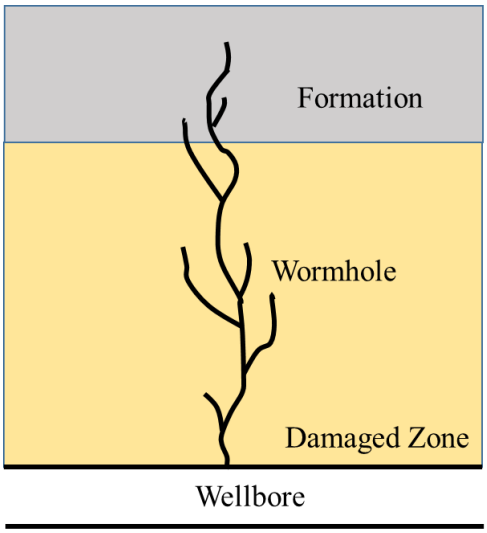

Figure 4.2 Illustration of wormhole generation in horizontal wells

4.2 Wormhole Models Review

In Chapter 3 the methodology of how to determine the optimal conditions in the laboratory with linear core flooding was introduced. Previous researchers did extensive studies on how to apply the measured optimal interstitial velocity and optimal pore volume to breakthrough into field

application. Buijse-Glasbergen developed a semi-empirical model to predict the wormhole propagation for radial flow geometry that only requires the measurement of $V_{i,opt}$ and $PV_{bt,opt}$ (Buijse and Glasbergen 2005). In this model the wormhole growth rate decreases as the wormhole front penetration r_{wh} increases as Equation 4.1 gives, this is because as the wormholes grow longer in radial direction, the acid loss becomes greater as more acid-formation contact area is created so that the wormhole tip receives less acid for deeper penetration.

$$v_{wh} = \left(\frac{v_i}{PV_{bt,opt}} \right) \times \left(\frac{v_i}{v_{i,opt}} \right)^{-\lambda} \times \left\{ 1 - \exp\left[-4 \left(\frac{v_i}{v_{i,opt}} \right)^2 \right] \right\}^2 \tag{4.1}$$

where v_{wh} is the wormhole front velocity, v_i is the interstitial velocity, γ is 1/3 when wormhole growth is loss-limited , $V_{i,opt}$ and $PV_{bt,opt}$ are the optimal interstitial velocity and optimal pore volume to breakthrough measured in the laboratory, respectively.

The wormhole front penetration r_{wh} can be calculated step by step. Firstly the acid pumping time can be sub-divided into small time steps Δt, and the initial wormhole front penetration is the same as the wellbore radius r_w, the acid interstitial velocity is assumed as constant in that time step Δt , then the wormhole front penetration for time $t+1$ can be calculated by:

$$r_{wh}(t+1) = r_{wh}(t) + v_{wh} \cdot \Delta t \tag{4.2}$$

Furui also developed a wormhole growth rate model (Furui 2010) based on Buijse-Glasbergen's model as:

$$v_{wh} = v_{i,tip} N_{ac} \times \left(\frac{v_{i,tip} PV_{bt,opt} N_{ac}}{v_{i,opt}} \right)^{-\lambda} \times \left\{ 1 - \exp\left[-4 \left(\frac{v_{i,tip} PV_{bt,opt} N_{ac} L_{core}}{v_{i,opt} r_{wh}} \right)^2 \right] \right\}^2 \tag{4.3}$$

$$v_{i,tip} = \frac{q}{\phi h \sqrt{\pi m_{wh}}} \left[\frac{1-\alpha_z}{\sqrt{d_{e,wh} r_{wh}}} + \frac{\alpha_z}{d_{e,wh}} \right] \tag{4.4}$$

where N_{ac} is the acid capacity number, L_{core} is the length of the core plug used to determine the optimal conditions in the laboratory, $v_{i,tip}$ is the acid velocity at the wormhole front, m_{wh} is the dominant wormhole number in 2D plane across the wellbore, α_z is the coefficient for wormhole spacing in axial direction, $d_{e,wh}$ is the diameter of the generated wormhole cluster and it can be approximated as :

$$d_{e,wh} = d_{core} N_{ac} PV_{bt,opt} \tag{4.5}$$

The wormhole front penetration r_{wh} for Furui's model is calculated the same method as Equation 4.2. Both Buijse-Glasbergen's model and Furui's model are recommended for matrix acidizing design in field, especially Furui's model since the effect of core size on optimal conditions is taken into calculation to reduce uncertainty. As shown in Figure 3.12, the optimal conditions measured from large diameter cores is much lower than that measured in small diameter cores.

Based on the calculated wormhole front penetration r_{wh}, the skin factor s can be calculated. Positive skin factor indicates that formation is damaged with additional pressure drop in the near-wellbore region, negative skin factor is favorable for production and it is most likely caused by well stimulation (matrix acidizing, acid fracturing, etc.).

4.3 Well Performance with Wormhole

An illustration of the regions near the wellbore in cross-section view (Figure 4.3). The wellbore radius is r_w, the wormhole front penetration r_{wh} has not reached beyond the damage zone

r_s, which has the damaged permeability k_s. The permeability for the undamaged reservoir is k, the reservoir radius is r_e and the flow is assumed to be in steady-state.

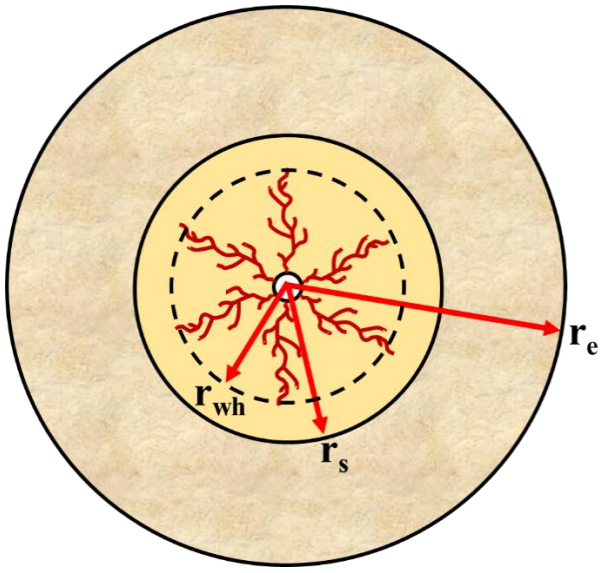

Figure 4.3 The cross-section view of various regions near a wellbore under acidizing

In ideal condition, the formation is not damaged and the skin factor is zero. The pressure drop between the reservoir boundary and wellbore is:

$$p_e - p_{wf,ideal} = \frac{q\mu}{2\pi kh} \ln \frac{r_e}{r_w} \tag{4.6}$$

In real condition, formation damage exists and the pressure drop is increased by adding a positive skin factor:

$$p_e - p_{wf,real} = \frac{q\mu}{2\pi kh} \ln(\frac{r_e}{r_w} + s) \tag{4.7}$$

The pressure drop from the reservoir boundary to the wellbore radius also can be expressed by adding up the pressure drop in each zone:

$$p_e - p_{wf,real} = \frac{q\mu}{2\pi kh}\ln(\frac{r_e}{r_s}) + \frac{q\mu}{2\pi k_s h}\ln(\frac{r_e}{r_{wh}}) + \frac{q\mu}{2\pi k_{wh} h}\ln(\frac{r_{wh}}{r_w}) \tag{4.8}$$

Integrating Equation 4.7 and Equation 4.8, provides:

$$\frac{q\mu}{2\pi kh}\ln(\frac{r_e}{r_w} + s) = \frac{q\mu}{2\pi kh}\ln(\frac{r_e}{r_s}) + \frac{q\mu}{2\pi k_s h}\ln(\frac{r_e}{r_{wh}}) + \frac{q\mu}{2\pi k_{wh} h}\ln(\frac{r_{wh}}{r_w}) \tag{4.9}$$

Reorganizing Equation 4.9, we have the skin factor expressed as:

$$s = \frac{k}{k_s}\ln\left(\frac{r_s}{r_{wh}}\right) + \frac{k}{k_{wh}}\ln\left(\frac{r_{wh}}{r_w}\right) - \ln\left(\frac{r_s}{r_w}\right) \tag{4.10}$$

The permeability in wormhole k_{wh} is larger than the original formation permeability by orders of magnitude, so the term with k/k_{wh} can be treated as 0. Then Equation 4.10 becomes:

$$s = \frac{k}{k_s}\ln\left(\frac{r_s}{r_{wh}}\right) - \ln\left(\frac{r_s}{r_w}\right) \tag{4.11}$$

Equation 4.11 is the skin factor for the reservoir before the wormhole grow beyond the damaged zone. After a wormhole propagates deeper into the formation and bypasses the damaged zone, k_s is replaced by k_{wh} and the term k/k_{wh} becomes very small, then this term can be neglected.

The final skin factor for acidized formation with wormhole front penetration of r_{wh} is:

$$s = -\ln\left(\frac{r_{wh}}{r_w}\right) \tag{4.12}$$

Based on Equation 4.12, it is observed that deep wormhole penetration into a formation is preferred rather than short wormholes. The average skin factor is -4 for matrix acidizing for

approximately 400 wells (Furui et al. 2010). This means that the wormhole penetration is about 18 ft beyond the wellbore if the wellbore radius r_w is taken as 0.328 ft, indicating matrix acidizing is a successful well stimulation technique to enhance well productivity.

4.4 Horizontal Well Acid Simulator

Horizontal well acid stimulator (HWAS) is an in-house simulator for matrix acidizing treatment design, real-time acidizing performance monitoring and well stimulation optimization in oil reservoir or gas reservoirs. This simulator was firstly developed by Furui (2004) and Mishra (2007), and further modified and improved by several researchers (Nozaki 2009, Pandya 2012, Tran 2013, Ueda 2015). HWAS has integrated several models, including a reservoir flow model, a fluid interface tracking model, a wormhole propagation model, a skin calculation model and a wellbore flow model. The model for acidizing treatment design is introduced (Figure 4.4).

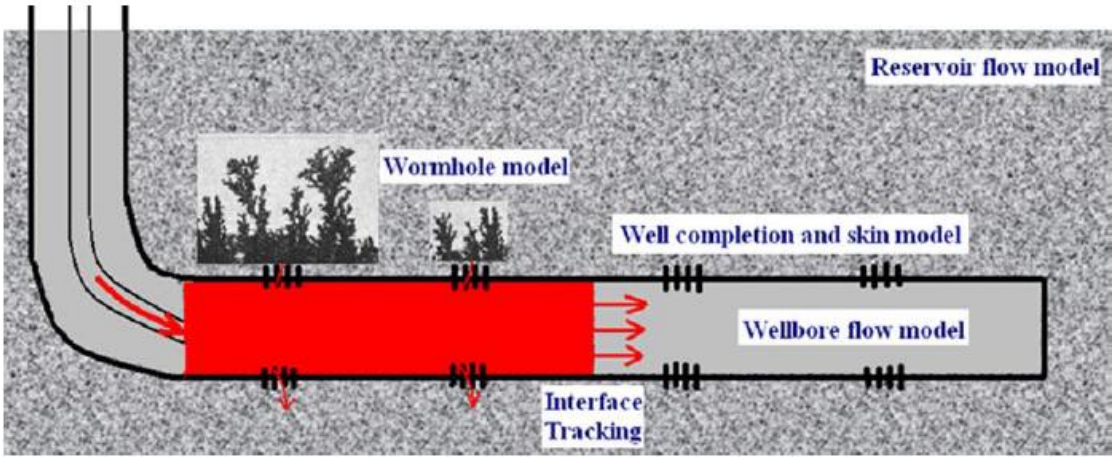

Figure 4.4 The models of horizontal well acid simulator (Reprinted from Ueda 2015)

A matrix acidizing treatment design can be efficiently implemented with HWAS. The workflow for matrix acidizing is given in Figure 4.5. At first, basic information about acid

treatment type, reservoir fluid type (gas or oil), and well completion schematic are needed. Next, the essential reservoir properties (e.g. formation pressure, formation thickness, fluid viscosity, etc.), well parameters (e.g. wellbore radius, casing diameter, etc.) and specific parameters for the designed completion type are provided. The completion type includes openhole completion, cased perforated completion, slotted liner completion, and perforated liner completion. The acid treatment type includes bullheading, coiltubing, acid jetting, and limited entry techniques (Ueda. 2015).

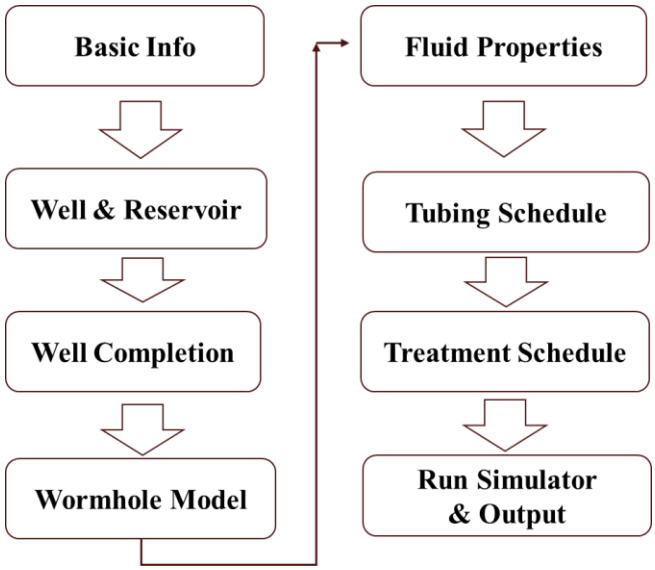

Figure 4.5 Workflow chart for matrix acidizing design with HWAS

Next the wormhole models can be selected from the volumetric model, the Buiji-Glasbergen model, and Furui's model. The measured optimal pore volume to breakthrough and optimal interstitial velocity from the laboratory are required for wormhole modeling. Then for each discretized segment of the horizontal well, the horizontal permeability, permeability impairment ratio, and damage penetration are provided. The original design of the wellbore segmentation only uses one set of porosity and permeability for the whole stimulated wellbore section, where the

heterogeneity of porosity and permeability are neglected. It is difficult to determine the effect of variation of petrophysical properties on acidizing performance along the wellbore. In this study, this workflow is upgraded with the petrophysical module to better design acid treatments (Figure 4.6), the details are discussed in next two sections.

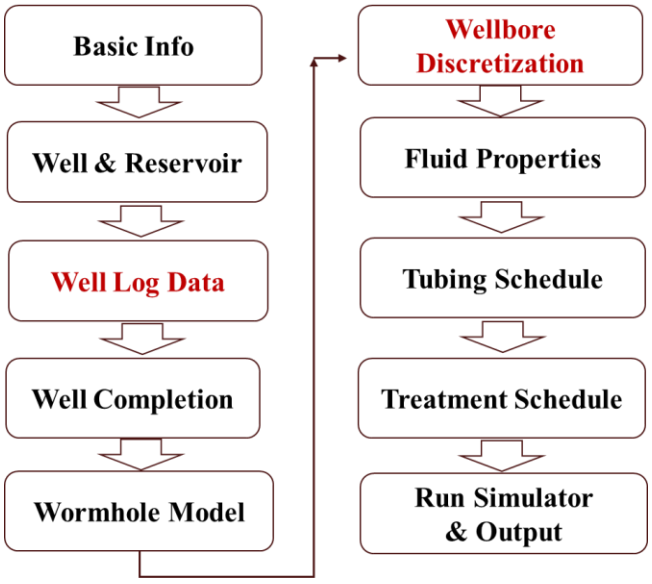

Figure 4.6 The updated workflow for HWAS

Next, the properties of injected fluid and pumping schedules are provided. Theoretically the optimal injection rate can be calculated using Furui's model. Recall wormhole growth rate equation:

$$v_{wh} = v_{i,tip} N_{ac} \times \left(\frac{v_{i,tip} PV_{bt,opt} N_{ac}}{v_{i,opt}} \right)^{-\lambda} \times \left\{ 1 - \exp\left[-4 \left(\frac{v_{i,tip} PV_{bt,opt} N_{ac} L_{core}}{v_{i,opt} r_{wh}} \right)^2 \right] \right\}^2 \qquad (4.13)$$

where N_{ac} is acid capacity number.

For Furui's model, assuming the wormhole growth rate at the tip is always maintained at optimal growth rate, we have:

$$v_{i,tip} = v_{i,tip,opt} \tag{4.14}$$

The optimal wormhole growth rate at the tip increases as wormhole front penetration increases, it is given by:

$$v_{i,tip,opt} = \frac{v_{i,opt}}{PV_{bt,opt}N_{ac}}\frac{r_{wh}}{L_{core}} \tag{4.15}$$

Integrating Equation 4.14 and Equation 4.15 into Equation 4.13, the wormhole growth rate is simplified as:

$$v_{wh} = \left(\frac{v_{i,opt}}{PV_{bt,opt}}\right)\cdot\left(\frac{r_{wh}}{L_{core}}\right)^{\frac{2}{3}}\cdot\left[1-\exp(-4)\right]^2 \tag{4.16}$$

$$\text{or} \quad v_{wh} = 0.964\cdot\left(\frac{v_{i,opt}}{PV_{bt,opt}}\right)\cdot\left(\frac{r_{wh}}{L_{core}}\right)^{\frac{2}{3}} \tag{4.17}$$

So the theoretical optimal acid injection rate can be calculated by rearranging Equation 4.4 as:

$$q = \frac{v_{i,tip,opt}}{\phi L\sqrt{\pi m_{wh}}}\left[\frac{1-\alpha_z}{\sqrt{d_{e,wh}r_{wh}}} + \frac{\alpha_z}{d_{e,wh}}\right] \tag{4.18}$$

In field practice, the maximum injection rate below the fracturing pressure is commonly recommended (Glasbegen et al. 2009). The application of optimal injection rate needs to done carefully since it requires relative uniform formation without drastic permeability variations or pressure differences, and the formation zone should be relatively short. After matrix acidizing

simulation, the variation of bottomhole pressure, reservoir flow rate and total skin with time are calculated.

4.5 Petrophysical Properties Estimation

Heterogeneity in carbonate reservoir permeability, mineralogy, and porosity distribution is critical for treatment design (Abou-Sayed et al. 2007; Glasbegen et al. 2009; Ueda 2015). High permeability can help with wormhole initiation and growth but unfavorable acid distribution with more acid going into high permeability locations can be detrimental for stimulation performance. Additionally, acid has different responses to limestone, dolomite, or other mineralogy common in carbonate units. It is necessary to consider lithology variation while designing an acidizing treatment. In this section the practical methods to estimate porosity, lithology and permeability based on well logs are introduced. The estimated properties are exported as inputs for HWAS, which is introduced in detail in the next section.

4.5.1 Estimation of Porosity and Lithology

For conventional reservoirs, the simplified petrophysical model consists of shale and matrix, pore spaces are distributed in matrix and shale filled with water or hydrocarbon. For openhole well log analysis, the first step is to perform data quality control to check environmental effects on well log data. Then Gamma Ray (GR) log is normally used to calculate the volumetric concentration of shale. Cross-plots (Neutron-Density cross-plots, Neutron-Sonic cross-plots, etc.) can be applied to identify the mineralogy in the matrix if the mineral types are less than two. The total porosity of the formation can be estimated using the bulk density log, neutron porosity log, and sonic log either individually or jointly. But for formations with complex lithology containing more than two minerals or various clay types in shale, the multi-mineral joint inversion is recommended to solve

the volumetric concentration of each mineral and the total porosity. The multi-mineral joint inversion is performed by solving sets of linear or semi-linear equations. The basic principles are explained with the following example.

Assume there is a dolomitized limestone formation with limestone and dolomite matrix. The available well logs are bulk density $\rho_{\log}$, neutron porosity $n_{\log}$, compressional wave slowness $\Delta t_{\log}$, and volumetric scatter cross section $U_{\log}$ calculated from density log, and Photo Electric Factor log (PEF). The recorded log responses from the formation are a linear combination of each formation component as Equation 4.19 to Equation 4.23.

$$V_{LS} + V_{DL} + V_{fluid} = 1 \tag{4.19}$$

$$V_{LS}\rho_{LS} + V_{DL}\rho_{DL} + V_{fluid}\rho_{fluid} = \rho_{\log} \tag{4.20}$$

$$V_{LS}n_{LS} + V_{DL}n_{DL} + V_{fluid}n_{fluid} = n_{\log} \tag{4.21}$$

$$V_{LS}\Delta t_{LS} + V_{DL}\Delta t_{DL} + V_{fluid}\Delta t_{fluid} = \Delta t_{\log} \tag{4.22}$$

$$V_{LS}U_{LS} + V_{DL}U_{DL} + V_{fluid}U_{fluid} = U_{\log} \tag{4.23}$$

In matrix form, these equations can be written as:

$$\begin{bmatrix} 1 & 1 & 1 \\ \rho_{LS} & \rho_{DL} & \rho_{fluid} \\ n_{LS} & n_{DL} & n_{fluid} \\ \Delta t_{LS} & \Delta t_{DL} & \Delta t_{fluid} \\ U_{LS} & U_{DL} & U_{fluid} \end{bmatrix} \begin{bmatrix} V_{LS} \\ V_{DL} \\ V_{fluid} \end{bmatrix} = \begin{bmatrix} 1 \\ \rho_{\log} \\ n_{\log} \\ \Delta t_{\log} \\ U_{\log} \end{bmatrix} \tag{4.24}$$

Assign simple symbols to each mineral and vector, we have:

$$\mathbf{M}=\begin{bmatrix} 1 & 1 & 1 \\ \rho_{LS} & \rho_{DL} & \rho_{fluid} \\ n_{LS} & n_{DL} & n_{fluid} \\ \Delta t_{LS} & \Delta t_{DL} & \Delta t_{fluid} \\ U_{LS} & U_{DL} & U_{fluid} \end{bmatrix} \quad \mathbf{x}=\begin{bmatrix} V_{LS} \\ V_{DL} \\ V_{fluid} \end{bmatrix} \quad \mathbf{y}=\begin{bmatrix} 1 \\ \rho_{log} \\ n_{log} \\ \Delta t_{log} \\ U_{log} \end{bmatrix} \tag{4.25}$$

The linear equation can be written as:

$$\mathbf{Mx}=\mathbf{y} \tag{4.26}$$

To solve Equation 4.26, weighted least squares solution method is adopted to minimize the errors as well as making the most of the input logs to reduce uncertainty.

$$\mathbf{M}^{\mathrm{T}}\mathbf{WMx}=\mathbf{M}^{\mathrm{T}}\mathbf{Wy} \tag{4.27}$$

where the weights W are the reciprocal of variance $\frac{1}{\sigma_i^2}$ for each log tool:

$$\mathrm{W}=\begin{bmatrix} 1 & 0 & 0 & 0 & 0 \\ 0 & 1/\sigma_{\rho}^2 & 0 & 0 & 0 \\ 0 & 0 & 1/\sigma_{n}^2 & 0 & 0 \\ 0 & 0 & 0 & 1/\sigma_{\Delta t}^2 & 0 \\ 0 & 0 & 0 & 0 & 1/\sigma_{U}^2 \end{bmatrix} \tag{4.28}$$

The volumetric concentration of each component is calculated as:

$$\mathbf{x}=\left(\mathbf{M}^{\mathrm{T}}\mathbf{WM}\right)^{-1}\mathbf{M}^{\mathrm{T}}\mathbf{Wy} \tag{4.29}$$

Figure 4.7 is an example of the estimated porosity and lithology in a tight carbonate formation using multi-mineral joint inversion (Zhou et al. 2019). The available mineralogy is obtained from core XRD tests and mud logging reports, including shale, quartz, calcite, and dolomite. The input logs for joint inversion are bulk density (RHOB), neutron porosity (NPHI), compressional wave slowness (Dt), and photo electric factor log (PEF). The estimated total porosity should always be cross-validated by core measurement from the laboratory.

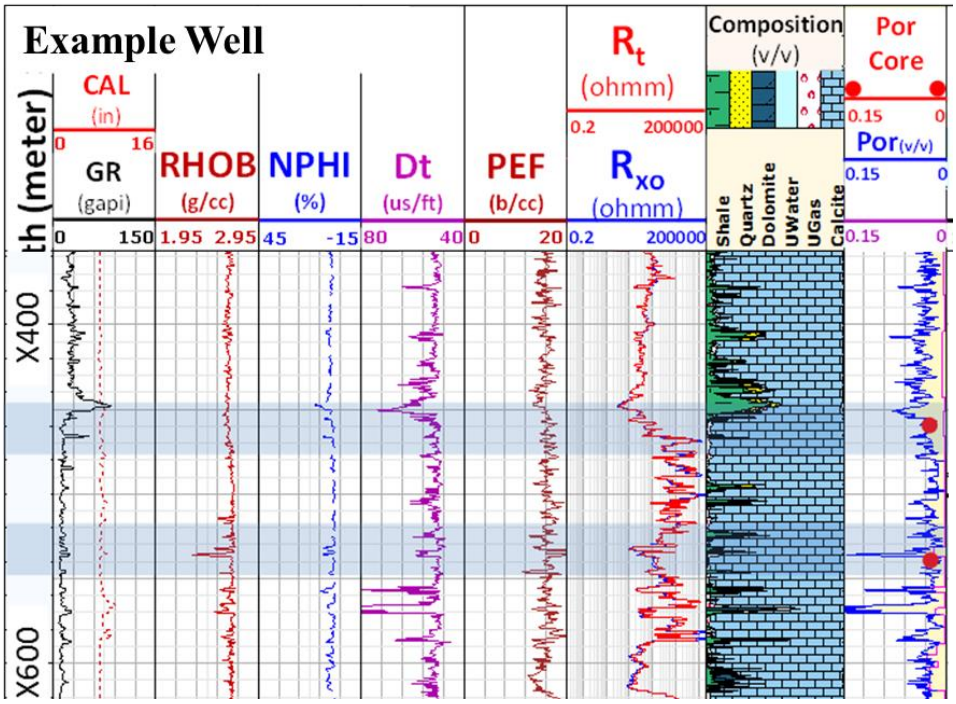

Figure 4.7 The well logs used for multi-mineral joint inversion, the estimated lithology and estimated porosity. Tracks from 1 to 9 are: measured depth (meter);caliper log and gamma ray; bulk density; neutron porosity; compressional wave slowness; photo electric factor log; shallow resistivity and deep resistivity; estimated volumetric concentration of each mineral; estimated total porosity and total porosity by core measurements (red dots) (Reprinted from Zhou et al. 2019)

4.5.2 Estimation of Permeability

In this section the practical permeability estimation methods based on well logs are introduced, most methods require core measurements as input or benchmark for calibration.

4.5.2.1 Permeability Estimation with Empirical Correlations

Researchers developed many empirical correlations to estimate formation permeability with estimated total porosity, effective porosity, and irreducible water saturation. The most famous

empirical correlation follows a general form of Wyllie-Rose methods (Equation 4.30) or Coates method (Equation 4.31, Equation 4.32).

$$k = k_w \cdot \frac{\phi^d}{S_w^e} \tag{4.30}$$

For Equation 4.30, Morris-Biggs method uses d = 6, e=2, k_w= 62500 for oil and k_w = 6500 for gas (Morris and Biggs, 1967); Timur's method uses d=4.4, e=2, k_w = 3400 for oil and k_w = 340 for gas (Timur 1968).

Coates method for permeability is as Equation 4.31 for clean zones and Equation 4.32 for else (Coates and Dumanoir, 1973):

$$k = k_c \cdot \phi_e^4 \cdot \left(\frac{1 - S_{wirr}}{S_{wirr}} \right)^2 \tag{4.31}$$

$$k = k_c \cdot \phi_e^4 \cdot \left(\frac{\phi_t - \phi_e \cdot S_{wirr}}{\phi_e \cdot S_{wirr}} \right)^2 \tag{4.32}$$

where K_c is adjusting parameter, ϕ_e is estimated effective porosity, ϕ_t is estimated total porosity, S_{wirr} is estimated irreducible water saturation, which can be estimated with Buckles method (Buckles 1965).

Both Wyllie-Rose's empirical correlations and Coates equations can be applied when core measurements are not available but core measurements are strongly recommended to calibrate the model and/or perform cross-validation. Additionally, permeability can also be estimated with NMR log if it is available (Coates 1999).

Permeability estimation based on the regressed porosity-permeability relationship also is widely used for carbonate rocks. Generally, the measured core porosity is positively related to measured permeability with the form of Equation 4.33:

$$\log(k) = C_3 + D_3 \log(\phi) \tag{4.33}$$

where C_3 and D_3 are fitting parameters for specific reservoir or rock type.

Figure 4.8 is the porosity-permeability correlation for a tight carbonate formation based on core measurements (Zhou et al. 2017). The fitted porosity-permeability correlation is given by Equation 4.34:

$$k = 0.026\phi^{0.3} \tag{4.34}$$

Equation 4.34 is applied for permeability estimation for local wells (Figure 4.9) and the estimated permeability matches well with the core measurements. Similarly, the permeability estimated by Coates equation also matches well with the core permeability, but Morris-Biggs' method and Timur's method underestimate the permeability.

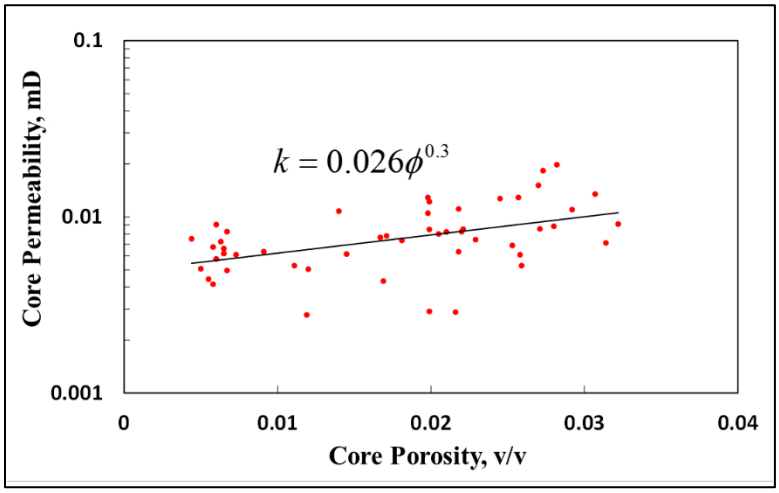

Figure 4.8 Porosity-permeability correlation from core measurement for a tight carbonate formation (Reprinted from Zhou et al. 2017)

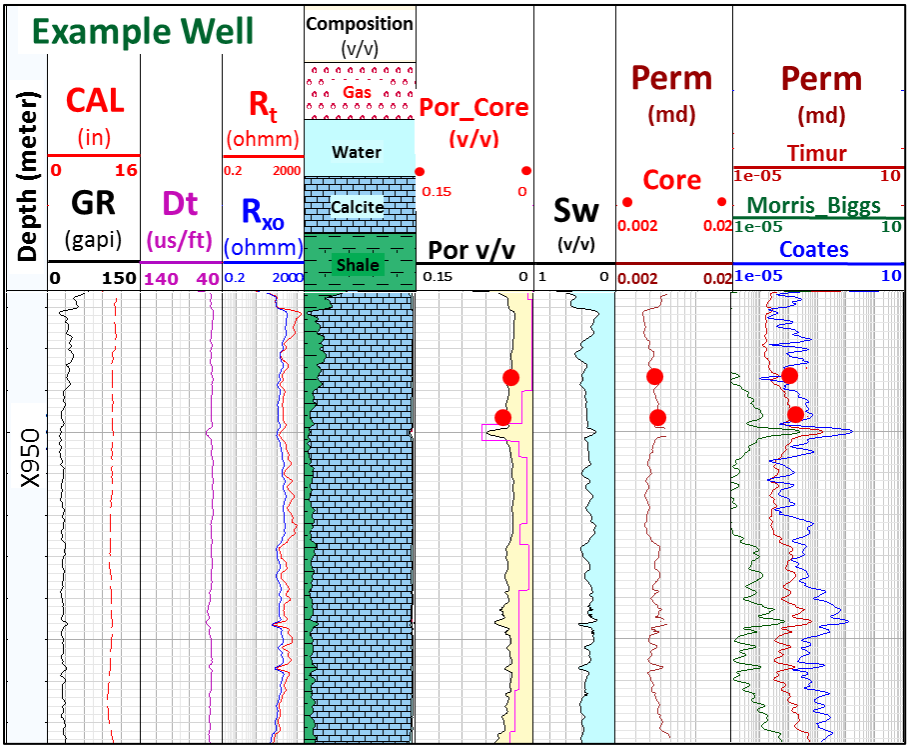

Figure 4.9 Example of estimated permeability by different method. Tracks from 1 to 9 are: measured depth in meter; caliper log and gamma ray log; compressional wave slowness log; shallow resistivity and deep resistivity log; estimated volumetric concentration of minerals; estimated porosity with core measurements (in red dots); estimated water saturation; estimated permeability with porosity-permeability correlation; estimated permeability with Timur's equation, Morris-Biggs equation, Coates equation, the core permeability (in red dots) (Reprinted from Zhou et al. 2017)

The porosity-permeability correlation in carbonate units normally has large uncertainties and should be applied with care. Permeability estimation with ϕ-k correlation based on rock classification (Zhou et al. 2017) or Rock-Fabric methods (Lucia 1999) are recommended if sufficient core measurements, thin section description, and stratigraphic framework are available.

4.5.2.2 Permeability Estimation with Multivariable Linear Regression

Researchers developed extensive multivariable linear regression models to build correlations between well logs and measured core permeability for specific formations or reservoirs. One of

the practical and reliable methods is non-parametric regression technique (Xie 2008). This method differs from conventional multivariable linear regression since it performs optimal transformation of the well logs to maximize the relationship between the well logs and the target permeability (Xie 2008). GRACE software is used to perform the data transform.

Suppose the well logs and depth-by-depth measured permeability are available for a specific formation face, then each well log can be transform from itself as linear form with polynomial equations:

$$log\_Tr(i) = p_1 log(i)^n + p_2 log(i)^{n-1} + \cdots + p_m \tag{4.35}$$

where *log_Tr* is the transformation of each well log; *log(i)* are the well logs used as inputs, normally including gamma ray, density log, neutron porosity, PEF log, sonic log and deep resistivity; p_m are the fitting parameters.

After transformation, the transformed well logs are compiled as:

$$SumTr = \sum log\_Tr(i) \tag{4.36}$$

The polynomial relationship between the measured permeability and well logs is:

$$\log(k) = q_1 SumTr^N + q_2 SumTr^{N-1} + \cdots q_m \tag{4.37}$$

where q_m are the fitting parameters.

Then the generated correlation (Equation 4.37) can be applied to other wells without core measurements to predict permeability. Figure 4.10 is an example of the estimated permeability plotted against measured permeability. The red dots are measured permeability for a new well, the blue dots are the estimated permeability using the generated correlation from other wells. The correlation coefficient is 0.62, which is satisfactory for such a heterogeneous carbonate formation.

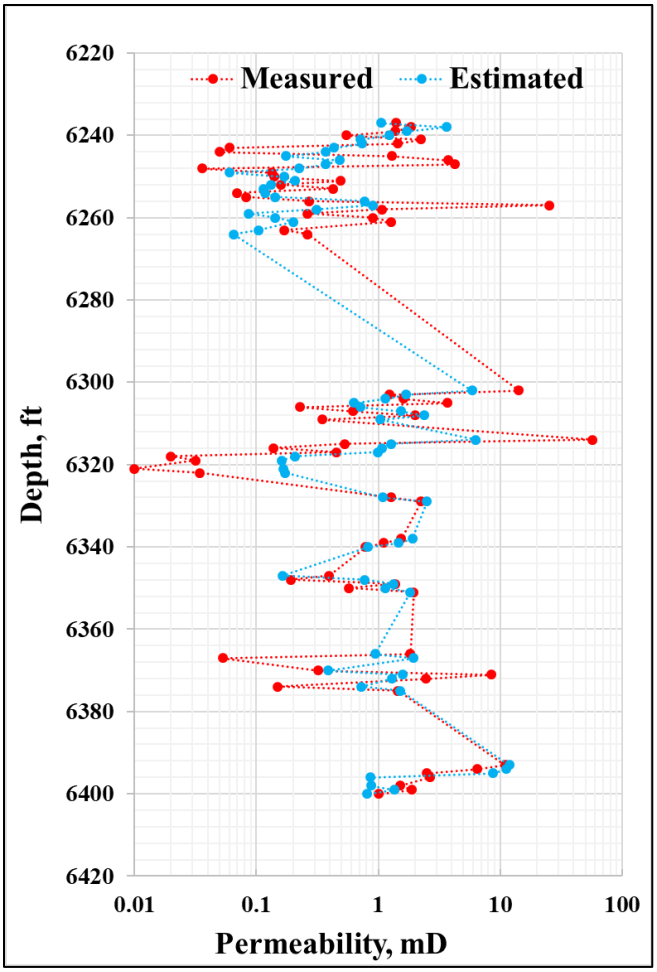

Figure 4.10 The estimated permeability with non-parametric regression against the measured core permeability

Many permeability estimation techniques based on Artificial Neural Networks (ANN) share similar procedure as this non-parametric regression method. This method requires sufficient core measurements for at least one well and well-to-well geological correlation to apply to new wells for the same formation face.

4.6 Integration of Petrophysical Models into HWAS

The petrophysical modules introduced in section 4.3 are integrated into HWAS (Figure 4.11). In this module, the depth-by-depth estimated porosity, permeability and dominant lithology can be

directed imported from well log interpretation. Before transferring the petrophysical data into HWAS, it is recommended to convert them from log scale resolution (e.g. 0.5 ft) to resolution as needed (e.g. 5ft) for matrix acidizing simulation. The interface of the developed data converter is shown in Figure 4.12.

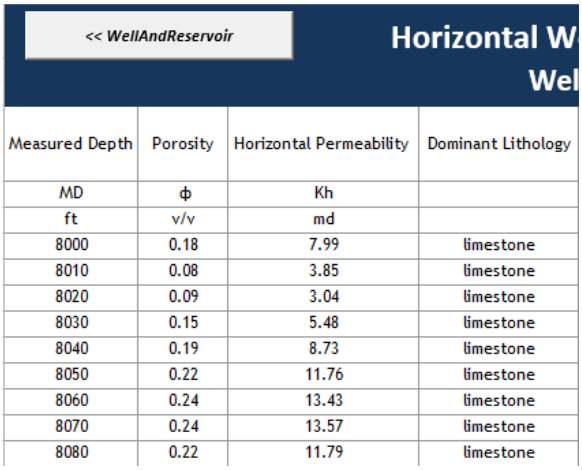

<< WellAndReservoir

Horizontal W
Wel

Measured Depth	Porosity	Horizontal Permeability	Dominant Lithology
MD	ϕ	Kh	
ft	v/v	md	
8000	0.18	7.99	limestone
8010	0.08	3.85	limestone
8020	0.09	3.04	limestone
8030	0.15	5.48	limestone
8040	0.19	8.73	limestone
8050	0.22	11.76	limestone
8060	0.24	13.43	limestone
8070	0.24	13.57	limestone
8080	0.22	11.79	limestone

Figure 4.11 The integrated petrophysical module in HWAS

Desired Resolution, ft	Maximum Original Resolution, ft		Run Data Filter			
20.00	4.21					
Input Measured Depth, ft	Porosity,v/v	Permeability, md	Input Well Log Resolution	Filtered Measured Depth, ft	Filtered Porosity, v/v	Filtered Permeability, md
1000.00	0.01	10.01	0.42	1008.28	0.01	10.11
1000.42	0.01	10.02	0.52	1030.26	0.01	10.28
1000.94	0.01	10.03	0.60	1051.30	0.02	10.40
1001.54	0.01	10.04	0.67	1072.57	0.02	10.51
1002.21	0.01	10.05	0.73	1093.82	0.02	10.60
1002.95	0.01	10.06	0.79	1114.32	0.02	10.69
1003.74	0.01	10.07	0.85	1134.82	0.02	10.77
1004.59	0.01	10.08	0.90	1156.41	0.02	10.85
1005.49	0.01	10.09	0.95	1177.60	0.02	10.92
1006.44	0.01	10.10	0.99	1198.17	0.02	10.99
1007.44	0.01	10.11	1.04	1219.48	0.02	11.06
1008.47	0.01	10.12	1.08	1241.50	0.02	11.13
1009.56	0.01	10.13	1.12	1264.22	0.02	11.20

Figure 4.12 The petrophysical data resolution converter

Now the workflow is updated in Figure 4.7. The wormhole optimal conditions for each single segment can be customized using the laboratory measurements in “Wellbore Discretization” part.

4.7 Section Summary

In this chapter, the main models and workflow for HWAS were reviewed, including the matrix acidizing design and wormhole model. The practical methods to estimate porosity, lithology and permeability based on well logs were introduced. The developed petrophysical modules were integrated into HWAS.

5. FIELD EXAMPLE OF FORMATION CHARACTERIZATION FOR ACID STIMULATION

5.1 Field Application with HWAS

In this section one synthetic matrix acidizing treatment simulation with HWAS based on field data is demonstrated. 15 wt% HCl was bullheaded into a 2860 ft long horizontal well section to perform matrix acidizing. The well completion type is openhole and the wellbore scheme is illustrated in Figure 5.1. The formation is heterogeneous limestone with high permeability peaks. The total porosity is estimated based on a neutron porosity log since a density log or sonic log is not available, and the average porosity for this formation is 17%. The permeability profile is estimated based on production logging data since core measurements were not available (Tran, 2013). The average permeability is 22 mD. The other basic reservoir data are listed in Table 5.1. Two sets of optimal conditions were used for wormhole modeling (Table 5.2), which were estimated based on history matching (Tran, 2013). The pumping schedule is listed in Table 5.3.

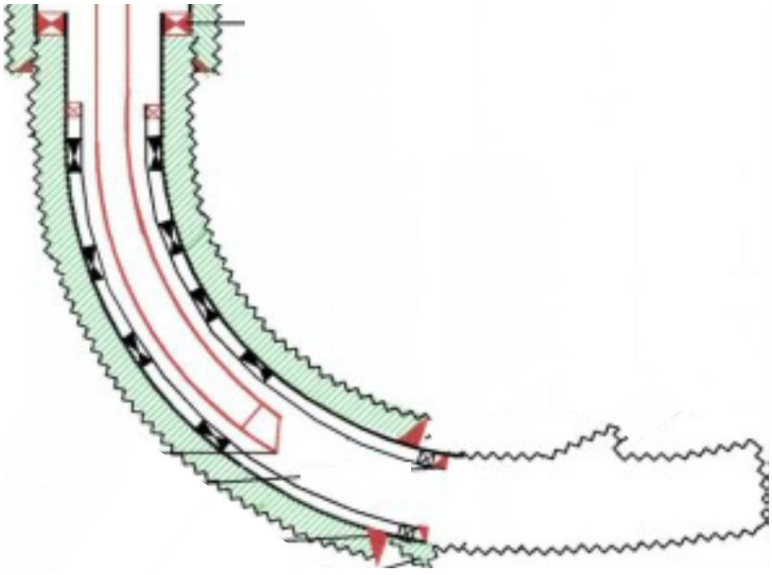

Figure 5.1 Well completion scheme

Table 5.1 Well and Stimulation Data

Parameters	Value
Completion Type	Openhole
Treatment Type	Bullheading
Reservoir Type	oil
Rock Type	Limestone
Reservoir Pressure(psi)	2750
Netpay Thickness(ft)	307
Fluid Viscosity(cP)	0.46
Wellbore Length(ft)	2860
Wellbore Radius(ft)	0.2917
Formation Top Depth(ft) MD/TVD	8000/7560
Simulation Length(ft)	2860
Acid Concentration, wt%	15
Average Porosity, v/v	0.17
Average Permebility, mD	22

Table 5.2 Optimal Points (Tran, 2013)

Optimal Points	PVbt,opt	Vi,opt, cm/min
1	0.85	1.75
2	0.53	1.75

Table 5.3 Pumping Schedule

Stage Number #	Duration min	Rate bpm	Fluid
1	0	0	Water
2	3	18	HCl
3	7	17	HCl
4	5	17	HCl
5	24	16.2	HCl
6	8	15.6	HCl
7	11	15.6	HCl
8	4	14	HCl
9	4	19	HCl
10	1	20.2	HCl
11	2	21.6	HCl
12	3	21.6	HCl
13	18	22	HCl
14	5	20	HCl

The simulated total skin variation with time is given in Figure 5.2. The simulated total skin for this well drops from 2.9 to -2.5 after the treatment, indicating the matrix acidizing is successful.

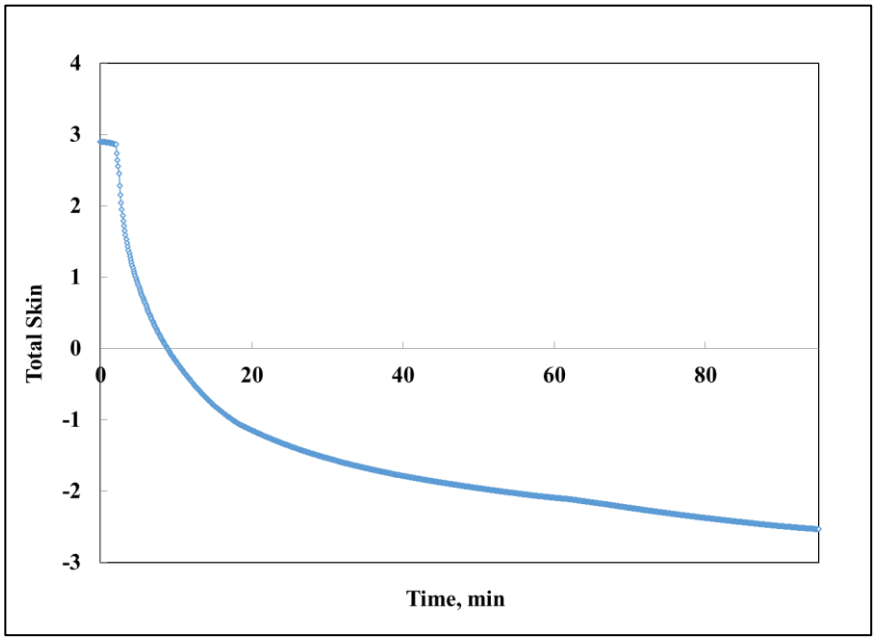

Figure 5.2 Total skin variation with time

The acid consumption and wormhole length along the wellbore are plotted in Figure 5.3. The simulated results show that the high permeability zone accepted much more acid than other sections and long wormholes near that region were created, leaving the other locations poorly treated. This indicates that for highly heterogeneous formations, especially those with permeability peaks, diversion techniques are required to create more even treatment for all locations. This synthetic case also demonstrates that the integrated petrophysical model can help completion engineer with acidizing treatment planning.

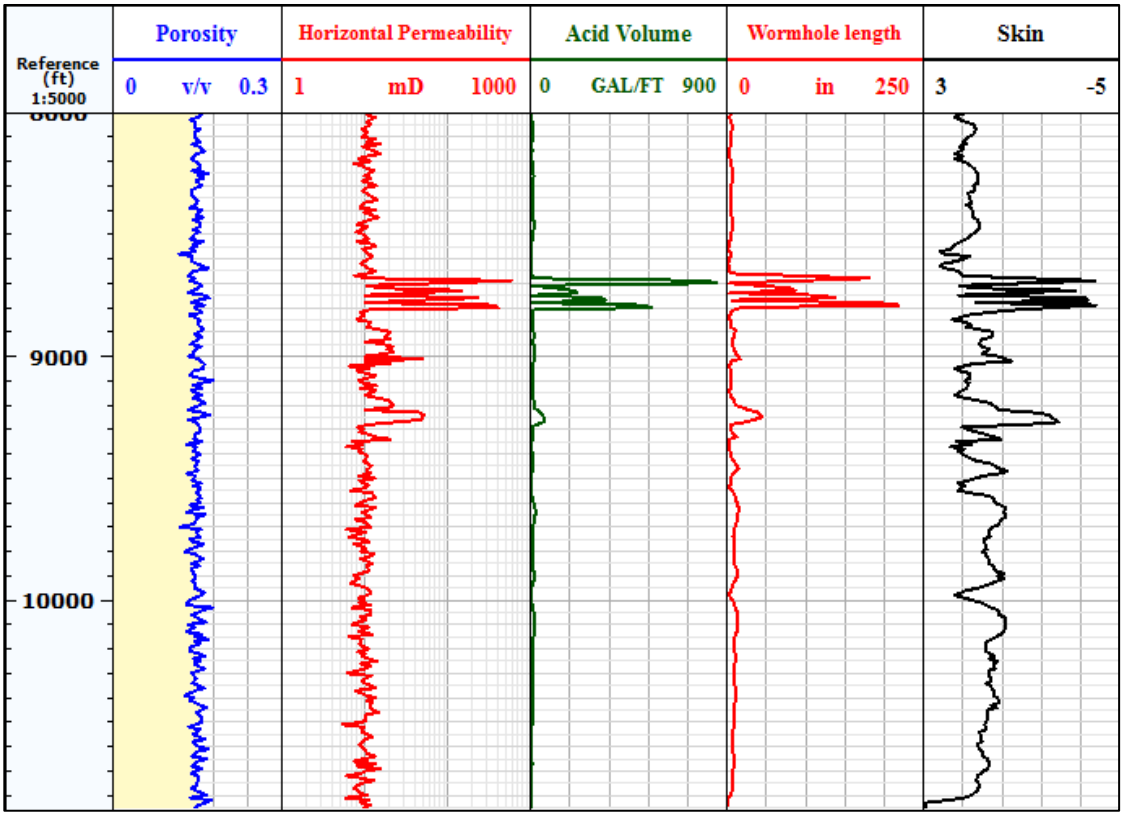

Figure 5.3 Depth-by-depth porosity, permeability, acid consumption, wormhole length, and skin factor along the horizontal well after simulated acidizing treatment

5.2 Estimation of Optimal Conditions

In this section, we introduce the method of estimating optimal conditions for matrix acidizing based on proposed correlations in Chapter 2 and Chapter 3. The optimal conditions for two rock types are measured and compared against the estimated results.

5.2.1 Estimation of Optimal Conditions for Indiana Limestone

Following the method introduced in Chapter 3, seven Indiana limestone core plugs with diameter of 1.5 inch and length of 8 inch are acidized with 15 wt% of HCl under 180 °F with varying injection rate. The average porosity is 13% and average permeability is 22.4 mD. The optimal conditions are obtained by fitting with Buijse-Glasbergen model (Figure 5.4).

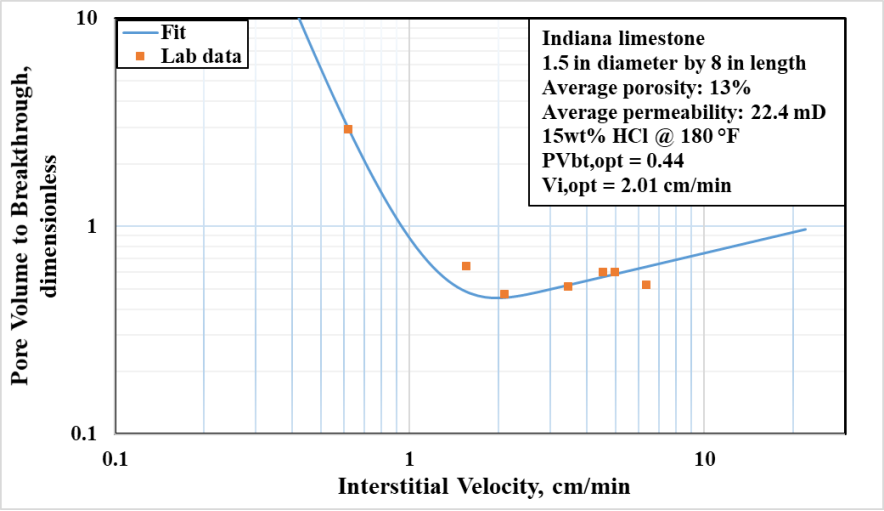

Figure 5.4 Measured optimal conditions for Indiana limestone

Next, we estimate the optimal conditions by using the proposed correlations in Chapter 2 and Chapter 3. The equivalent pore radius for Indiana limestone samples is calculated as (Equation 2.5):

$$R_e = \left(\frac{k}{0.0008}\right)^{\frac{1}{2.9559}} = \left(\frac{22.4}{0.0008}\right)^{\frac{1}{2.9559}} = 31.95\,\mu m \tag{5.1}$$

where R_e is in μm, k is in mD.

With Equation 2.6, the optimal pore volume to breakthrough is estimated as:

$$PV_{bt,opt} = 0.3658\ln(R_e) - 0.7249 = 0.3658\ln(31.95) - 0.7249 = 0.54 \tag{5.2}$$

With Equation 3.5, the optimal interstitial velocity is estimated as:

$$V_{i,opt} = 0.95\ln(k) + 0.9 = 0.95\ln(22.4) + 0.9 = 3.85\,cm/\min \tag{5.3}$$

where $V_{i,opt}$ is in cm/min, and k is in mD.

By comparing the estimated optimal conditions against measured results, the estimated pore volume to breakthrough $PV_{bt,opt}$ is consistent with laboratory measured results, but optimal interstitial velocity $V_{i,opt}$ is over-estimated by using proposed correlation (Equation 3.5).

5.2.2 Estimation of Optimal Conditions for Kansas Chalk

Following the method introduced in Chapter 3, four Indiana limestone core plugs with diameter of 1.5 inch and length of 6 inch are acidized with 15 wt% of HCl under 70 °F with varying injection rate. The average porosity is 33% and average permeability is 1.6 mD. The optimal conditions are obtained by fitting with Buijse-Glasbergen model (Figure 5.5).

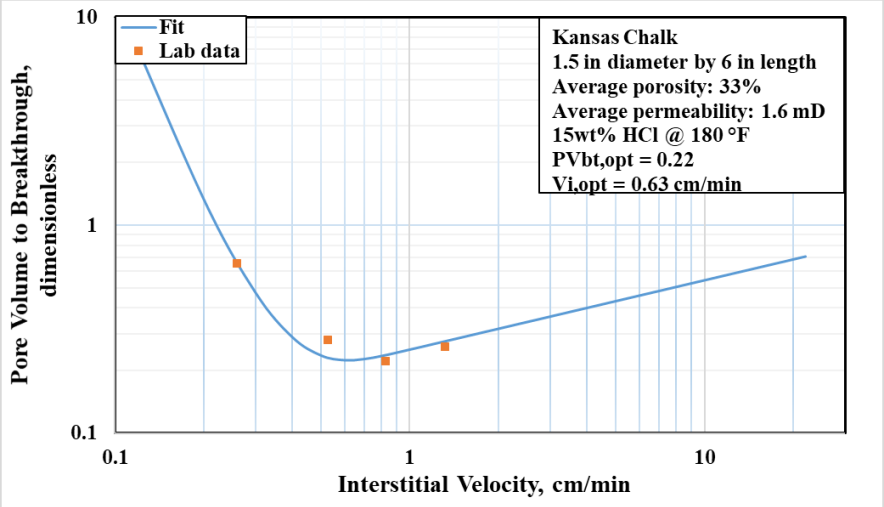

Figure 5.5 Measured optimal conditions for Kansas Chalk

Next, we estimate the optimal conditions by using the proposed correlations in Chapter 2 and Chapter 3. The equivalent pore radius for Kansas Chalk samples is calculated as (Equation 2.5):

$$R_e = \left(\frac{k}{0.0008}\right)^{\frac{1}{2.9559}} = \left(\frac{1.6}{0.0008}\right)^{\frac{1}{2.9559}} = 13.08\,\mu m \tag{5.4}$$

where R_e is in μm, k is in mD.

With Equation 2.6, the optimal pore volume to breakthrough is estimated as:

$$PV_{bt,opt} = 0.3658\ln(R_e) - 0.7249 = 0.3658\ln(13.08) - 0.7249 = 0.22 \tag{5.5}$$

With Equation 3.5, the optimal interstitial velocity is estimated as:

$$V_{i,opt} = 0.95\ln(k) + 0.9 = 0.95\ln(1.6) + 0.9 = 1.35 cm/\min \quad (5.6)$$

where $V_{i,opt}$ is in cm/min, and k is in mD.

Similar to Indiana limestone, the estimated pore volume to breakthrough $PV_{bt,opt}$ is consistent with laboratory measured results, but optimal interstitial velocity $V_{i,opt}$ is over-estimated by using proposed correlation (Equation 3.5). The experiment data for optimal condition measurements and estimation are given in Table 5.4.

Table 5.4 The experiment data for optimal condition measurements and estimation

Rock Type	Temperature, °F	HCl wt%	Porosity, v/v	Permeability, mD	Core Size, inch	Measured $PV_{bt,opt}$	Estimated $PV_{bt,opt}$	Measured $V_{i,opt}$, cm/min	Estimated $V_{i,opt}$, cm/min
Indiana Limestone	180	15%	0.13	22.4	1.5×8	0.44	0.54	2.01	3.85
Kansas Chalk	70	15%	0.33	1.6	1.5×6	0.22	0.22	0.63	1.35

5.3 Skin Factor Calculation with Optimal Conditions

In this section, examples of skin factor calculations for two formation sections with varying permeability values are given. Formation section A is 20 ft long, the average permeability is 15 mD. Formation section B is also 20 ft long, the average permeability is 180 mD. Figure 5.6 gives the workflow for skin factor calculation.

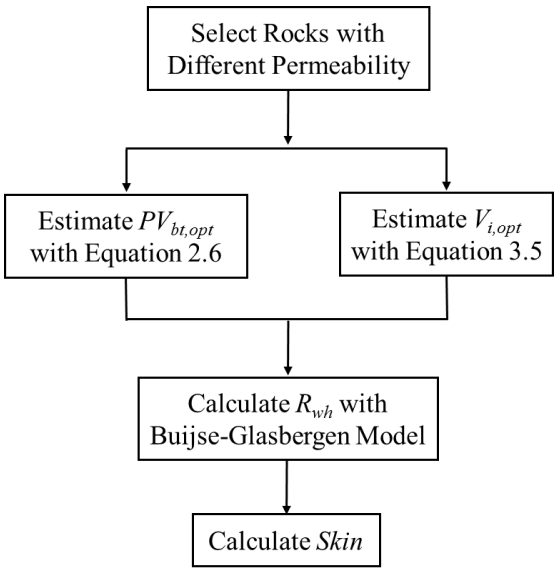

Figure 5.6 Workflow to calculate skin with estimated optimal conditions

5.3.1 Case A

For formation section A, Indiana limestone is used as analogy since its permeability is close (15 mD). Following the method introduced in section 5.2, the optimal conditions are estimated. The equivalent pore radius for formation section A is calculated as (Equation 2.5):

$$R_e = (\frac{k}{0.0008})^{\frac{1}{2.9559}} = (\frac{15}{0.0008})^{\frac{1}{2.9559}} = 27.90\,\mu m \tag{5.7}$$

where R_e is in μm, k is in mD.

With Equation 2.6, the optimal pore volume to breakthrough is estimated as:

$$PV_{bt,opt} = 0.3658\ln(R_e) - 0.7249 = 0.3658\ln(27.90) - 0.7249 = 0.49 \tag{5.8}$$

With Equation 3.5, the optimal interstitial velocity is estimated as:

$$V_{i,opt} = 0.95\ln(k) + 0.9 = 0.95\ln(15) + 0.9 = 3.47\,cm/\min \tag{5.9}$$

where $V_{i,opt}$ is in cm/min, and k is in mD.

Next, Buijse-Glasbergen model is used to calculated the wormhole radius R_{wh} (reviewed in Section 4.2). The injection rate is assumed constant at 10 bbl/min. The designed injection treatment for simulation lasts for 5 minutes. The calculation steps are:

The initial wormhole radius R_{wh} has the same value as wellbore radius R_w, the initial interstitial velocity V_i is calculated using Equation 5.4 in radial geometry:

$$V_i(R_{wh}) = \frac{Q}{2\pi R_{wh} h\phi} = \frac{5.615(ft^3/bbl)\times 10\ (bbl/\min)}{2\times 3.1416\times 0.2917(ft)\times 20(ft)\times 0.11(v/v)} = 13.93\ ft/\min \quad (5.10)$$

The constant W_{eff} in Buijse-Glasbergen model is calculated as:

$$W_{eff} = \frac{V_{i,opt}^{1/3}}{PV_{bt,opt}} = \frac{(3.47\,cm/\min\times 0.0328\ ft/cm)^{1/3}}{0.49} = 0.9891(ft/\min)^{1/3} \quad (5.11)$$

The constant W_B in Buijse-Glasbergen model is calculated as:

$$W_B = \frac{4}{V_{i,opt}^2} = \frac{4}{(0.1138\ ft/\min)^2} = 308.62(ft/\min)^{-2} \quad (5.12)$$

The B-function in Buijse-Glasbergen model is calculated as:

$$B(V_i) = (1-\exp(-W_B\cdot V_i^2))^2 = (1-\exp(-308.62(ft/\min)^{-2}\cdot(13.93\ ft/\min)^2))^2 = 1 \quad (5.13)$$

The wormhole growth rate at first time step is calculated as:

$$V_{wh} = W_{eff}\cdot V_i^{2/3}\cdot B(V_i) = (0.9891\ ft/\min)^{1/3}\times(13.93\,ft/\min)^{2/3}\times 1 = 5.77\ ft/\min \quad (5.14)$$

Then the wormhole radius for any time step is calculated by:

$$R_{wh}(t+\Delta t) = R_{wh}(t) + V_{wh}\cdot\Delta t \quad (5.15)$$

Set initial time t=0, time step $\Delta t = 0.01$ min, then the wormhole radius for the second time step is:

$$R_{wh}(\Delta t) = R_{wh}(0) + V_{wh}\cdot\Delta t \quad (5.16)$$

$$R_{wh}(\Delta t) = 0.2917 + 5.77(ft/\min)\times 0.01(\min) = 0.3494\ ft \quad (5.17)$$

These calculation steps are repeated from Equation 5.4 to Equation 5.10 until the desired injection volume is reached.

The skin factor is calculated with Equation 4.12 (assuming wormholes have reached beyond the damaged zone):

$$s = -\ln\left(\frac{r_{wh}}{r_w}\right) = -\ln\left(\frac{6.2411\ ft}{0.2917\ ft}\right) = -3.06 \tag{5.18}$$

Similar wormhole propagation and skin factor calculation for section A were performed with optimal conditions used by Tran (2013). The calculated optimal conditions, simulated wormhole radius and final skin factor are listed in Table 5.5.

Table 5.5 Optimal conditions, wormhole radius and skin factor for case A

Optimal Conditions	Perm, md	Porosity, v/v	Equivalent Pore Radius, µm	$PV_{bt,opt}$	$V_{i,opt}$, cm/min	W_{eff}	Final R_{wh}, ft	Final Skin
This Study	15	0.11	27.9	0.49	3.47	0.99	6.2	-3.1
Tran, 2013	15	0.11	NA	0.85	1.75	0.45	3.9	-2.6

The simulated wormhole radius against the acid consumption is plotted in Figure 5.7. The slopes of the two curves in Figure 5.7 are proportional to wormhole growth rate V_{wh} since the injection rate is constant. The wormhole growth rate V_{wh} in Buijse-Glasgergen model is linearly proportion to the constant W_{eff} (Equation 5.8), which is determined by optimal conditions (Equation 5.5). The calculated W_{eff} is given in Table 5.4.

The wormhole growth rate V_{wh} calculated with the estimated optimal conditions in this study is faster than that of Tran (2013), thus the final wormhole penetration is deeper and final skin factor is more favorable for production.

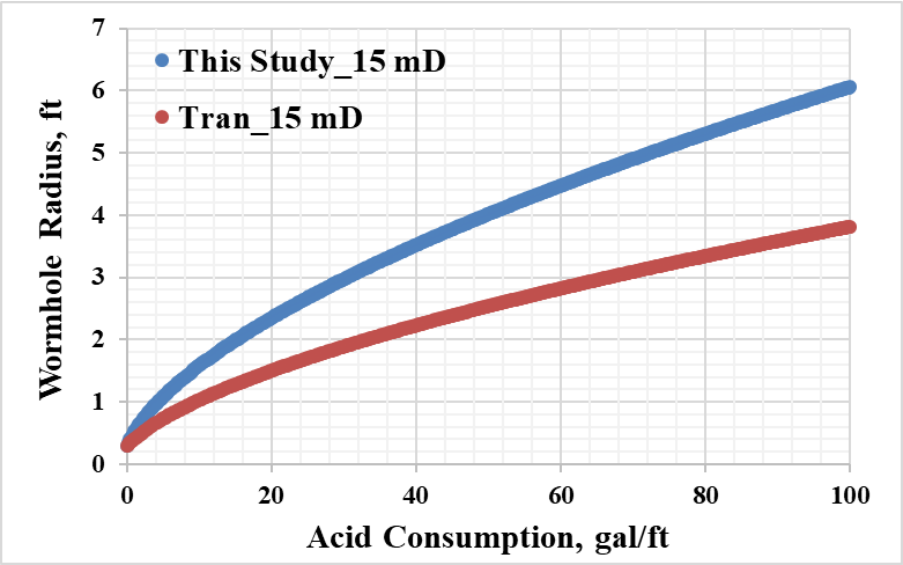

Figure 5.7 Acid consumption against wormhole radius (Case A)

5.3.2 Case B

For formation section B, Travertine is used as an analogy since permeability is close (180 mD). Using Equation 2.5, the equivalent pore radius for formation section B is calculated as:

$$R_e = \left(\frac{k}{0.0008}\right)^{\frac{1}{2.9559}} = \left(\frac{180}{0.0008}\right)^{\frac{1}{2.9559}} = 64.67\ \mu m \tag{5.19}$$

where R_e is in μm, k is in mD.

With Equation 2.6, the optimal pore volume to breakthrough is estimated as:

$$PV_{bt,opt} = 0.3658\ln(R_e) - 0.7249 = 0.3658\ln(64.67) - 0.7249 = 0.80 \tag{5.20}$$

With Equation 3.5, the optimal interstitial velocity is estimated as:

$$V_{i,opt} = 0.95\ln(k) + 0.9 = 0.95\ln(180) + 0.9 = 5.8\,cm/\min \tag{5.21}$$

where $V_{i,opt}$ is in cm/min, and k is in mD.

Wormhole radius and skin factor were calculated with same method as in case A. The calculated optimal conditions, simulated wormhole radius and final skin factor are listed in Table 5.6.

Table 5.6 Optimal conditions, wormhole radius and skin factor for case B

Optimal Conditions	Perm, md	Porosity, v/v	Equivalent Pore Radius, μm	$PV_{bt,opt}$	$V_{i,opt}$, cm/min	W_{eff}	Final R_{wh},ft	Final Skin
This Study	180	0.12	64.7	0.80	5.80	0.72	5.0	-2.8
Tran, 2013	180	0.12	NA	0.53	1.75	0.73	5.0	-2.8

The simulated wormhole radius against the acid consumption for case B is plotted in Figure 5.8. The wormhole growth rate, final wormhole penetration depth, and final skin are similar since the constant W_{eff} calculated by the two sets of optimal conditions are close (Table 5.5).

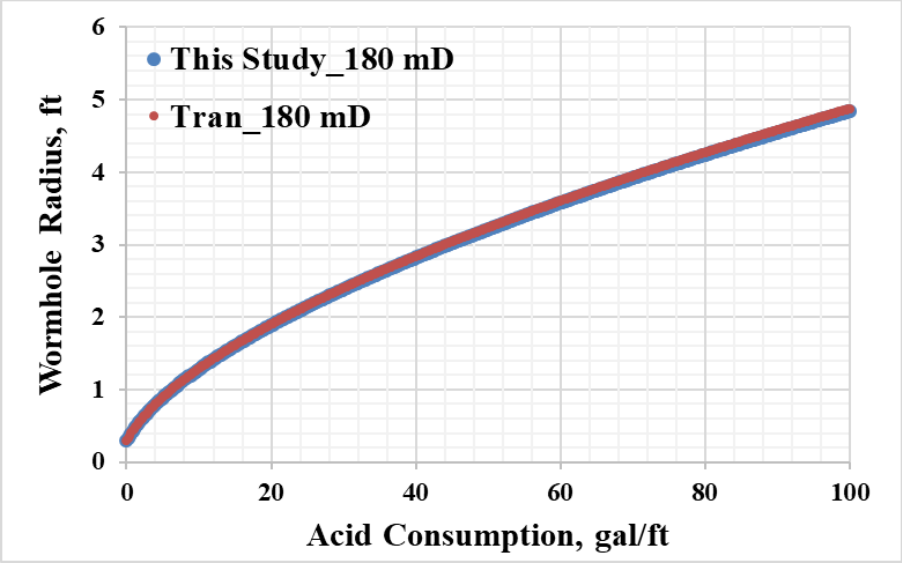

Figure 5.8 Acid consumption against wormhole radius (Case B)

5.4 Section Summary

In this chapter, a synthetic matrix acidizing treatment case based on field data was demonstrated. The simulation results indicate that the heterogeneity of petrophysical properties along the wellbore played an important role for a successful matrix acidizing treatment. A carefully designed diversion technique is required for highly heterogeneous formation to be successfully stimulated.

Examples of estimating optimal conditions with permeability and equivalent pore radius was given. The correlation between equivalent pore radius R_e and optimal pore volume breakthrough $PV_{bt,opt}$ was given in Chapter 2, and the correlation between permeability and optimal interstitial velocity $V_{i,opt}$ was given in Chapter 3. Two cases with varying permeability values are compared for wormhole propagation calculation and skin factor calculation.

6. CONCLUSIONS

In this dissertation formation characterization for matrix acidizing is performed at micro-scale, core-scale and log-scale. The main conclusions are:

At micro-scale, we studied the micro-structures and important petrophysical parameters for Indiana Limestone, Desert Pink, and Travertine with micro-CT imaging technique. We defined the concept of equivalent pore radius with processed binary images, and we determined that laboratory-measured permeability from core plugs is strongly correlated to the equivalent pore radius calculated from micro-CT scanned images among the investigated carbonate rock samples. The semi-logarithmic correlation between permeability and effective pore radius fit the measured permeability data very well over a permeability range of more than two orders of magnitude. The findings of pore-scale pore structure and pore size distribution in this study are helpful for carbonate rock analysis, and a second permeability model is proposed based on measured porosity and equivalent pore radius. Two permeability models are recommended for permeability estimation with digital rock data. The equivalent pore radius for each Indiana limestone and Desert Pink rock is positively correlated with optimal pore volume to breakthrough whereas Travertine does not follow the same trend.

Additionally, we quantified the connectivity of the pore systems for tested rock samples with the concept of Euler-Poincare Characteristic number and calculated the surface-area-to-volume ratio. We observed that better connectivity, which has smaller connectivity number, leads to a higher permeability. Optimal pore volume to breakthrough increases as the connectivity increases. The relationship between connectivity number in unit volume and the optimal interstitial velocity are not clear. The surface-area-to-volume ratio is negatively related to the permeability, optimal pore volume to breakthrough and optimal interstitial velocity.

At core-scale, the optimal conditions for Travertine were obtained. Travertine is highly heterogeneous and anisotropic with vuggy pore structures, the optimal interstitial velocity is 7.4 cm/min, which is much higher than other tested rock types. The historical data for 13 sets of matrix acidizing experiments was collected and their wormhole-efficiency curve was generated. The test rock types include Indiana limestone, Glen Rose, Desert Pink, Kansas chalk, vuggy calcite, and Travertine. The optimal interstitial velocity for most limestone tested except Travertine ranged from 1.46 cm/min to 3.34 cm/min even though the experiment temperature and acid concentration vary quite a bit. The optimal pore volume to breakthrough ranges from 0.32 to 0.75 for all tested rock types. Core scale for matrix acidizing has great impact on optimal conditions: both pore volume to breakthrough and optimal interstitial velocity decrease as core diameter increases. We also determined that permeability is positively related to optimal interstitial velocity. The impact of permeability on optimal pore volume to breakthrough is not definitely clear. The impact of porosity on optimal conditions was not observed.

At log-scale, practical methods to estimate porosity, lithology, and permeability based on well logs were introduced. The developed petrophysical module are integrated into HWAS and a synthetic case based on field data was demonstrated, indicating that heterogeneity of petrophysical properties along the wellbore plays an important role in a successful matrix acidizing job. Carefully designed diversion technique is required for highly heterogeneous formation. Besides, methods of estimating optimal conditions with permeability and equivalent pore radius was introduced and examples were given.

REFERENCES

Abou-Sayed, I., Shuchart, C. E., Choi, N. H., Clancey, B. M., & Bene, T. F. 2007. Well Stimulation Technology for Thick, Middle East Carbonate Reservoirs. International Petroleum Technology Conference. DOI:10.2523/IPTC-11660-MS

Ajay Limaye; Drishti. 2012. A volume exploration and presentation tool. Proc. SPIE 8506, Developments in X-Ray Tomography VIII, 85060X

Akanni, O. O., & Nasr-El-Din, H. A. 2015. The Accuracy of Carbonate Matrix-Acidizing Models in Predicting Optimum Injection and Wormhole Propagation Rates. Society of Petroleum Engineers. DOI:10.2118/172575-MS

Bazin, B. 2001. From Matrix Acidizing to Acid Fracturing: A Laboratory Evaluation of Acid/Rock Interactions. SPE Production & Facilities 16 (1): 22-29. SPE-66566-PA.

Bernabe, Y., Li, M., and Maineult, A. 2010. Permeability and Pore Connectivity: A New Model Based On Network Simulations. J. Geophysical Research 115 (B10): 203. http://dx.doi.org/10.1029/ 2010JB007444.

Berryman, J.G., 1981. Elastic wave propagation in fluid-saturated porous media,Journal of Acoustical Society of America, 69, 416-424.

Bolte, S. & Cordelières, F.P. 2006. A guided tour into subcellular colocalization in light microscopy. J. Microsc., 224, 213-232

Buckles, R. S. 1965. Correlating and Averaging Connate Water Saturation Data. Petroleum Society of Canada. DOI:10.2118/65-01-07

Buijse, M., de Boer, P., Breukel, B., Klos, M., & Burgos, G. 2003. Organic Acids in Carbonate Acidizing. Society of Petroleum Engineers. DOI:10.2118/82211-MS

Buijse, M.A. and Glasbergen, G. 2005. A Semiempirical Model to Calculate Wormhole Growth in Carbonate Acidizing. Paper presented at the SPE Annual Technical Conference and Exhibition, Dallas, Texas. SPE 96892. DOI: 10.2118/96892-ms.

Carman. 1937. Fluid flow through granular beds. Transactions of the Institution of Chemical Engineers, vol. 15, pp. 155–166

Carman. 1956. Flow of gases through porous media. Butterworths, London.

Chi, L., & Heidari, Z. 2016. Directional-Permeability Assessment in Formations With Complex Pore Geometry With a New Nuclear-Magnetic- Resonance-Based Permeability Model. Society of Petroleum Engineers. DOI:10.2118/179734-PA

Coates, G. R., & Dumanoir, J. L. 1973. A New Approach to Improved Log-Derived Permeability. Society of Petrophysicists and Well-Log Analysts.

Coates, G.R., Xiao, L., and Prammer, M.G. 1999. NMR Logging Principles and Applications. Publication H02308, Halliburton Energy Services, Houston, Texas, USA.

Daccord, G., Lenormand, R., and Liétard, O. 1993. Chemical Dissolution of a Porous Medium by a Reactive Fluid—I. Model for the "Wormholing" Phenomenon. Chemical Engineering Science 48 (1): 169-178. DOI: http://dx.doi.org/10.1016/0009-2509(93)80293-Y

Daccord, G., Touboul, E., and Lenormand, R. 1989. Carbonate Acidizing: Toward a Quantitative Model of the Wormholing Phenomenon. SPE Production Engineering 4 (1): 63-68. DOI: 10.2118/16887-pa

Dong, K. 2015. Theoretical And Experimental Study On Optimal Conditions In Carbonate Acidizing, Ph.D. dissertation, Texas A&M University, College Station, Texas (Dec 2015)

Dubetz, D., Cheng, H., Zhu, D., & Hill, A. D. 2016. Characterization of Rock Pore-Size Distribution and Its Effects on Wormhole Propagation. Society of Petroleum Engineers. DOI:10.2118/181725-MS

Etten, R.J. 2015. Experimental Investigation on the Effect of Permeability on the Optimum Acid Flux in Carbonate Matrix Acidizing, Master thesis, Texas A&M University, College Station, Texas

Economides, M.J., Hill, A.D., Ehlig-Economides, C, and Zhu, D. 2013. Petroleum Production Systems, Upper Saddle River, New Jersey: Prentice Hall.

Fredd, C.N. and Fogler, H.S. 1998. Alternative Stimulation Fluids and Their Impact of Carbonate Acidizing. SPE Journal 3 (1): 34-41. SPE 31074-PA. http://dx.doi.org/10.2118/31074-PA.

Fredd, C. N., & Miller, M. J. 2000. Validation of Carbonate Matrix Stimulation Models. Society of Petroleum Engineers. DOI:10.2118/58713-MS

Frick, T., Mostofizadeh, B. and Economides, M. 1994. Analysis of Radial Core Experiments of Hydrochloric Acid Interaction with Limestones. Presented at the International Symposium on Formation Damage Control, Lafayette, Louisiana, 7-10 February. SPE-27402-MS. http://dx.doi.org/10.2118/27402-MS.

Furui, Kenji. 2004. A comprehensive skin factor model for well completions based on finite element simulations, Ph.D. dissertation, The University of Texas at Austin, Austin, Texas

Furui, K., Burton, R.C., Burkhead, D.W. et al. 2010. A Comprehensive Model of High-Rate Matrix Acid Stimulation for Long Horizontal Wells in Carbonate Reservoirs. Paper presented at the SPE Annual Technical Conference and Exhibition, Florence, Italy. SPE SPE-134265-MS. DOI: 10.2118/134265-ms.

Gueguen, Y. and Dienes, J. 1989. Transport Properties of Rocks From Statistics and Percolation. Mathematical Geology 21 (1): 1–13. http://dx.doi.org/10.1007/BF00897237.

Golfier, F., Bazin, B., Zarcone, C. et al. 2001. Acidizing Carbonate Reservoirs: Numerical Modeling of Wormhole Propagation and Comparison to Experiments. Presented at the SPE European Formation Damage Conference, The Hague, Netherlands, 21-22 May. SPE-68922-MS. http://dx.doi.org/10.2118/68922-MS.

Hoefner, M.L. and Fogler, H.S. 1989. Fluid-Velocity and Reaction-Rate Effects During Carbonate Acidizing: Application of Network Model. SPE Production Engineering 4 (1): 56-62. SPE-15573-PA. http://dx.doi.org/10.2118/15573-PA.

Hoshen, J.; Kopelman, R. 1976. "Percolation and cluster distribution. I. Cluster multiple labeling technique and critical concentration algorithm". Phys. Rev. B. 14 (8): 3438–3445. DOI:10.1103/PhysRevB.14.3438

Huang, T., Hill, A. D., & Schechter, R. S. 1997. Reaction Rate and Fluid Loss: The Keys to Wormhole Initiation and Propagation in Carbonate Acidizing. Society of Petroleum Engineers. DOI:10.2118/37312-MS

Huang, T., Zhu, D., and Hill, A.D. 1999. Prediction of Wormhole Population Density in Carbonate Matrix Acidizing. Paper presented at the SPE European Formation Damage Conference, The Hague, Netherlands. SPE 54723. DOI: 10.2118/54723-ms.

Huang, L-K & Wang, M-J J .1995. Image thresholding by minimizing the measure of fuzziness. Pattern Recognition 28(1): 41-51

Iassonov, P., Gebrenegus, T., and Tuller, M. 2009. Segmentation of X‐ray computed tomography images of porous materials: A crucial step for characterization and quantitative analysis of pore structures, Water Resour. Res., 45, W09415, DOI:10.1029/2009WR008087.

Izgec, O., 2009. Reactive Flow In Vuggy Carbonates: Methods And Models Applied To Matrix Acidizing Of Carbonates, Ph.D. dissertation, Texas A&M University, College Station, Texas

Kozeny, J. 1927. Ueber kapillare Leitung des Wassers im Boden. Sitzungsber Akad. Wiss., Wien, 136(2a), pp 271-306.

Lucia, F.J., 1999. Carbonate Reservoir Characterization: Springer-Verlag, Berlin, Heidelberg, New York, 226 p.

Maheshwari, P., & Balakotaiah, V. 2013. 3D Simulation of Carbonate Acidization with HCl: Comparison with Experiments. Society of Petroleum Engineers. DOI:10.2118/164517-MS

McDuff, D., Shuchart, C. E., Jackson, S., Postl, D., & Brown, J. S. 2010. Understanding Wormholes in Carbonates: Unprecedented Experimental Scale and 3-D Visualization. Society of Petroleum Engineers. doi:10.2118/134379-MS

Mishra, Varun .2007. A model for matrix acidizing of long horizontal well in carbonate reservoirs. Master's thesis, Texas A&M University. Available electronically from http : / /hdl .handle .net /1969 .1 /ETD -TAMU -1957.

Morris, R. L., and W. P. Biggs. 1967. “Using log-derived values of water saturation and porosity” Transactions of the SPWLA 8th Annual Logging Symposium, Paper X, 26p.

Nakashima, Y., & Watanabe, Y. 2002. Estimate of transport properties of porous media by microfocus X‐ray computed tomography and random walk simulation. Water Resources Research, 38(12), 8-1.

Paccaloni, G., Tambini, M., & Galoppini, M. 1988. Key Factors for Enhanced Results of Matrix Stimulation Treatments. Society of Petroleum Engineers. DOI:10.2118/17154-MS

Panga, M.K.R., Ziauddin, M., and Balakotaiah, V. 2005. Two-Scale Continuum Model for Simulation of Wormholes in Carbonate Acidization. AIChE Journal 51 (12): 3231-3248. DOI: 10.1002/aic.10574

Ronchi, P., Cruciani, F., & Cirilli, S. 2013. Continental Carbonates as Hydrocarbon Reservoir, an Analogue Case Study from The Travertine of Saturnia, Italy. International Petroleum Technology Conference. DOI:10.2523/IPTC-17107-MS

Schechter, R.S. and Gidley, J.L. 1969. The Change in Pore Size Distribution from Surface Reactions in Porous Media. AIChE Journal 15 (3): 339-350. DOI: 10.1002/aic.690150309

Schindelin, J.; Arganda-Carreras, I. & Frise, E. et al. 2012. Fiji: an open-source platform for biological-image analysis. Nature methods 9(7): 676-682, PMID 22743772, DOI:10.1038/nmeth. 2019.

Schwalbert, M. P., Zhu, D., & Hill, A. D. 2017. Extension of an Empirical Wormhole Model for Carbonate Matrix Acidizing Through Two-Scale Continuum 3D Simulations. Society of Petroleum Engineers. DOI:10.2118/185788-MS

Timur, A. 1968. An Investigation of Permeability, Porosity, & Residual Water Saturation Relationships for Sandstone Reservoirs. Society of Petrophysicists and Well-Log Analysts.

Tran, Hau. 2013. Modeling and Optimization of Matrix Acidizing in Horizontal Wells in Carbonate Reservoirs. Master's thesis, Texas A&M University. Available electronically from http : / /hdl .handle .net /1969 .1 /149428.

Ueda, Kenji. 2015. Integrated Method to Evaluate Acid Stimulation of Horizontal Wells in Carbonate Reservoir through Treatment Pressure Analysis. Master's thesis, Texas A & M University. Available electronically from http : / /hdl .handle .net /1969 .1 /155416.

Y. Bernabé, M. Li, A. Maineult. 2010. Permeability and pore connectivity: A new model based on network simulations. Journal of Geophysical Research : Solid Earth, American Geophysical Union

Vogel, H. J. 1997. Morphological Determination of Pore Connectivity as a Function of Pore Size Using Serial Sections. European J. Soil Science 48 (3): 365–377. http://dx.doi.org/10.1111/j.1365-2389.1997. tb00203.x.

Wang, Y., Hill, A.D., and Schechter, R.S. 1993. The Optimal Injection Rate for Matrix Acidizing of Carbonate Formations. Paper presented at the SPE Annual Technical Conference and Exhibition, Houston, Texas. SPE 26578. DOI: 10.2118/26578-ms.

Wyllie, M.R.J. and Rose, W.D. 1950. Some Theoretical Considerations Related to the Quantitative Evaluation of the Physical Characteristics of Reservoir Rock From Electrical Log Data. J. Pet Tech 189: 105–108.

Xie, Jiang. 2008. Improved permeability prediction using multivariate analysis methods. Master's thesis, Texas A&M University. Available electronically from http: / /hdl .handle .net /1969 .1 /ETD -TAMU -3223.

Zakaria, A.S., Nasr-El-Din, H.A., and Ziauddin, M. 2015. Predicting the Performance of the Acid-Stimulation Treatments in Carbonate Reservoirs with Nondestructive Tracer Tests. SPE Journal. DOI: 10.2118/174084-PA

Zhang Ningning,He Dengfa,Sun Yanpeng and Li Haowu. 2014. Distribution Patterns and Controlling Factors of Giant Carbonate Rock Oil and Gas Fields Worldwide [J]. 19(6): 54-65.

Zhou, Ding Zhu, and A. D. Hill, Texas A&M University. 2019. “A New Petrophysical Correlation for the Permeability of Carbonate Rocks”. SPWLA 60th Annual Symposium, June 15-19, 2019, The Woodlands, TX

Zhou, Texas A&M University, Zoya Heidari, The University of Texas at Austin, Ding Zhu, and A. D. Hill, Texas A&M University. 2017. “Petrophysical Rock Classification, Permeability Estimation, and Elastic Moduli Assessment in Tight Carbonate Reservoirs: A Case Study in Tarim Field, China.” SPE 187516, SPE East Regional Meeting, October 4-6, 2017, Lexington, KY

Yuhai Zhou, Wenyu Zhang, and Ding Zhu, Texas A&M University. 2019. "Stimulation Evaluation in Horizontal Wells with Emphasis on Petrophysics and Rock Mechanics: A Case Study in Deep, Tight Carbonate Formation". IPTC-19118-MS, March 26-28, 2019, Beijing, China

Ziauddin, M.E. and Bize, E. 2007. The Effect of Pore-Scale Heterogeneities on Carbonate Stimulation Treatments. Paper presented at the SPE Middle East Oil and Gas Show and Conference, Kingdom of Bahrain. Society of Petroleum Engineers SPE-104627-MS. DOI: 10.2118/104627-ms